Theoretical and Experimental Investigations in Acoustofluidic Manipulation of Bioparticles

Hanlin Wang

A thesis submitted for the degree of Doctor of Philosophy

Cardiff University

March 2022

Abstract

With the maturation of micro and nano processing technologies and the development of microchip laboratories, the acoustofluidic manipulation of particles has been developed rapidly. Microfluidic chips as miniature experimental platforms are revolutionizing research tools in several disciplines. Acoustically driven microfluidic chips is a current research hotspot with the advantages of non-invasiveness, high strength, and good biocompatibility.

This thesis demonstrates acoustofluidic platforms based on static surface acoustic waves for particle manipulation, including the design of interdigital transducers (IDTs), cleaning room fabrication and integration with microfluidic technologies, electronics, and mechanical systems. I present a numerical model to predict the motion of particles under microfluidic manipulation. I employ a perturbation approach where the flow variables are divided into first- and second-order fields. Impedance boundary conditions are used to model microchannel walls and displacement boundary conditions are used to model acoustic actuation. This model is verified to be accurate by comparison with published numerical studies.

Furthermore, to extend the generalizability of the model, I present two microfluidic systems, conventional PDMS-SAW system, and the GaN system. By comparing numerical predictions with experimental results, I validate the GaN system's ability to manipulate particles with high throughput and verify the accuracy of the model for different piezoelectric materials and working frequencies. Based on this simulation model, I developed two new acoustic fluid configurations: a microchannel sandwiched between two identical surfaces acoustic wave (SAW) transducers (SAW-SAW) or between a piezoelectric transducer (PZT) and a SAW transducer (PZT-SAW). I have numerically simulated the distribution of acoustic pressure, time-averaged flow velocity, and particle trajectories in these devices and compared the simulation results for different acoustic fluid configurations. The results show that the SAW-SAW and PZT-SAW configurations produce significantly higher acoustic pressures and particle velocities in the microchannel. In addition, I have developed a novel Filled Tilt Angle (FTA) acoustic fluidic device to be applied to the mechanophenotyping of live cells. The FTA

device consists of an interdigital transducer placed at an angle along the microfluidic channel in the direction of fluid flow. Pressure nodes formed within the acoustic fluid field of the microchannel cause biological cells to deviate from their original flow pattern based on their mechanical properties, including volume, compressibility, and density. The threshold power that allows the cells to converge to the pressure node fully is used to calculate the acoustic contrast factor. To demonstrate the role of FTA in the mechanophenotyping of cells and to distinguish between different cell types, further experiments were performed by using A549 (lung cancer cells), MDB-MA-231 (breast cancer cells), and leukocytes. The obtained acoustic contrast factors for lung and breast cancer cells differed from those of leukocytes by 55.1% and 17.8%, respectively. These results show that this method can successfully distinguish between different cell types based on the acoustic contrast factors, which has tremendous clinical implications for identifying, for example, epithelial cells in the circulation.

Finally, this thesis extends the understanding of acoustofluidic units through the study of innovative microfluidic systems. It will further advance the knowledge of SSAW based cell manipulation techniques and enable further development for high precision cell manipulation and biosensor applications.

Acknowledgement

I would like to gratefully appreciate the following people:

My great supervisor, Dr. Xin Yang. This thesis was completed under the careful guidance of my supervisor, Dr. Xin Yang. Dr. Xin Yang has a broad academic vision, rich professional knowledge, a rigorous research attitude, and profound academic attainment. Since I joined the group, Dr. Yang Xin has been caring for me and has provided me with help and guidance in my research and life. Dr. Yang has been guiding me tirelessly from research directions to experimental designs, from study planning to short-term goals, from writing papers to optimizing drawings.

I would also like to thank Dr. Chao Sun for his essential inspiration and outstanding teaching in theoretical and experimental work in the field of acoustofluidics. Dr. Minghong Shen, Prof. Aled Clayton, Professor Yongqing Fu, Dr. Despina Moschou, Dr. Siva Sivaraya, Prof.Yuan Fan, Dr. You Zhou, Dr. Zhihua Xie, and Dr. Yinhua Dong for their selfless support and excellent guidance. Dr. Meng Cai, and Dr. Jun Wei provided necessary experimental support and biological samples for my research. I am grateful to my colleagues Fangda Wu, Roman Mikhaylov, and Xiaoyan Zhang for their first-class practical skills and good at solving various challenges in experiments, and I have collaborated with them on many experiments. In addition, I would like to thank the other members of MUSL for working together in the field of microfluidics and for overcoming the difficulties of the experiments together. I am very grateful to them for all their help. I want to thank my colleagues and staff at Cardiff University for providing research funding and PGR support.

I would also like to thank my friend, Qiang Cong, for his inspiration and support during my theoretical studies.

Finally, I would like to thank my wife, Yu Zhang, and my families for their continued support and understanding.

Table of contents

List of figures

List of tables

List of publications

Wang, H., Boardman, J., Zhang, X., Sun, C., Cai, M., Wei, J., Dong, Z., Feng, M., Liang, D., & Hu, S. (2023). An enhanced tilted-angle acoustic tweezer for mechanical phenotyping of cancer cells. Analytica Chimica Acta, 341120.

Wang, H., Yuan, F., Xie, Z., Sun, C., Wu, F., Mikhaylov, R., Shen, M., Yang, J., Zhou, Y., & Liang, D. (2023). Modelling hybrid acoustofluidic devices for enhancing Nano-and Micro-Particle manipulation in microfluidics. Applied Acoustics, 205, 109258.

Sun, C., Dong, Y., Wei, J., Cai, M., Liang, D., Fu, Y., Zhou, Z., Sui, Y., Wu, F. Mikhaylov, R., **Wang, H.**, Fan, F., Xie, Z., Stringer, M., Yang, Z., Wu, Z., Tian, L. & Yang, X. (2022). Acoustically accelerated neural differentiation of human embryonic stem cells. Acta Biomaterialia, 151, 333-345.

Ma, J., Liang, D., Yang, X., **Wang, H**., Wu, F., Sun, C., & Xiao, Y. (2021). Numerical study of acoustophoretic manipulation of particles in microfluidic channels. *Proceedings of the Institution of Mechanical Engineers, Part H: Journal of Engineering in Medicine*, 235(10), 1163-1174.

Wu, F., Shen, M. H., Yang, J., **Wang, H.**, Mikhaylov, R., Clayton, A., Qin, X., Sun, C., Xie, Z., & Cai, M. (2021). An enhanced tilted-angle acoustofluidic chip for cancer cell manipulation. IEEE Electron Device Letters, 42(4), 577-580.

Mikhaylov, R., Martin, M. S., Dumcius, P., **Wang, H**., Wu, F., Zhang, X., Akhimien, V., Sun, C., Clayton, A., & Fu, Y. (2021). A reconfigurable and portable acoustofluidic system based on flexible printed circuit board for the manipulation of microspheres. Journal of Micromechanics and Microengineering, 31(7), 074003.

Mikhaylov, R., Wu, F., **Wang, H**., Clayton, A., Sun, C., Xie, Z., Liang, D., Dong, Y., Yuan, F.,

& Moschou, D. (2020). Development and characterisation of acoustofluidic devices using detachable electrodes made from PCB. Lab on a Chip, 20(10), 1807-1814.

Sun, C., Mikhaylov, R., Fu, Y., Wu, F., **Wang, H**., Yuan, X., Xie, Z., Liang, D., Wu, Z., &. (2020). Flexible printed circuit board as novel electrodes for acoustofluidic devices. IEEE Transactions on Electron Devices, 68(1), 393-398.

Sun, C., Wu, F., Fu, Y., Wallis, D. J., Mikhaylov, R., Yuan, F., Liang, D., Xie, Z., **Wang, H**., & Tao, R. (2020). Thin film Gallium nitride (GaN) based acoustofluidic tweezer: modelling and microparticle manipulation. Ultrasonics, 108, 106202.

Sun, C., Wu, F., Wallis, D.J., Shen, M.H., Yuan, F., Yang, J., Wu, J., Xie, Z., Liang, D., **Wang, H**. & Yang, X, (2020). Gallium nitride: a versatile compound semiconductor as novel piezoelectric film for acoustic tweezer in manipulation of cancer cells. IEEE Transactions on Electron Devices, 67(8), 3355-3361.

Chapter 1 Introduction

1.1 Bio-particles manipulation

Bioparticles sized from 20 nm to 100 μm, including viruses, exosomes, cells, etc. are a critical part of biomedical and bioengineering research. It is of great importance for the different manipulations of biological particles such as cell separation, enrichment, and alignment. Most clinical diagnostics and basic research aim to understand the underlying causes of disease. To understand the underlying causes of disease, specific bioparticles need to be isolated from complex samples such as blood, saliva, and cell culture supernatants. [1] The isolation of cancer cells from blood has become a valuable complementary tool for cancer research, diagnosis, drug efficacy assessment and treatment.[2] The enrichment of exosomes in biological fluids holds promise for diagnostic applications of EVs (extracellular vesicles), which are lipid bilayer-delimited particles that are naturally released from almost all types of cell and, unlike a cell, cannot replicate.

Bioparticle manipulation methods can be classified as active or passive depending on the presence or absence of an external force field. Passive particle manipulation uses geometry or topology of the flow fields and channels within the manipulation system to manipulate the motion of particles. Active particle manipulation utilizes the external forces generated by external fields on the particles to manipulate the movement of the particles. This chapter will first review the development, progress, and principles of methods in bioparticles manipulation, i.e., hydrodynamic based methods, electrokinetic based methods, magnetic based methods, acoustic based methods. (Table.1) Then the applications in based on acoustofluidics will be discussed. Then the theoretical models in SAW-based acoustofluidics and a mechanophenotyping acoustic tweezer which motivates the studies in this thesis will be discussed.

Methods	Mechanism	Advantage	Disadvantage
Hydrodynamic based methods	Pressure field gradient	Short manipulation time	Low recovery
Electrokinetic based methods	Inhomogeneous electric field and homogeneous eletric field	Label free	Complicated system, biological basis underexplored
Magnetic based methods	Magnetic field strength	Highly specific	Low to medium throughput, time consuming,low recovery
Optical based methods	Optical polarizablilty	Minimal sample preparation and labeling, non-invasive	Medium throughput
Acoustic based methods	Acoustic resonacne	Label free,fast, high throughput, non-invasive	Specific type of material to be used

Table. 1 List of various methods used for bioparticles manipulations.

1.1.1 Hydrodynamic based methods

Hydrodynamic based methods are based on interacting fluids and particles with microstructures to separate particles by size, shape, and deformability. Deterministic lateral displacement (DLD),[3, 4] hydrophoresis,[5-7] and pinched flow fractionation (PFF)[8, 9] are examples of these techniques.

DLD is based on an array of micropillars, (as shown in **Fig. 1.1a**) with each row laterally offset by a finely tuned distance from the previous row. Depending on the column-to-streamline distance, this design generates different streamlines that move either in the main flow direction or along the offset sides of the previous rows of columns. Because of the steric hindrance of the column wall and the streamline following of the microparticles, particles smaller than the critical size pass through the gap of the column in the mean main flow direction repeatedly, whereas particles greater than the critical size travel along the offset direction due to the greater particle-column distance and laterally bumped along the offset direction. After multiple strut rows, lateral distances between large and small particles accumulate, eventually leading to separation. DLD has a high resolution but a low throughput. [8] Nanoparticles and exosomes with the size of 20 nm were recently sorted by using DLD at a flow rate of 10 μL/h.[4]

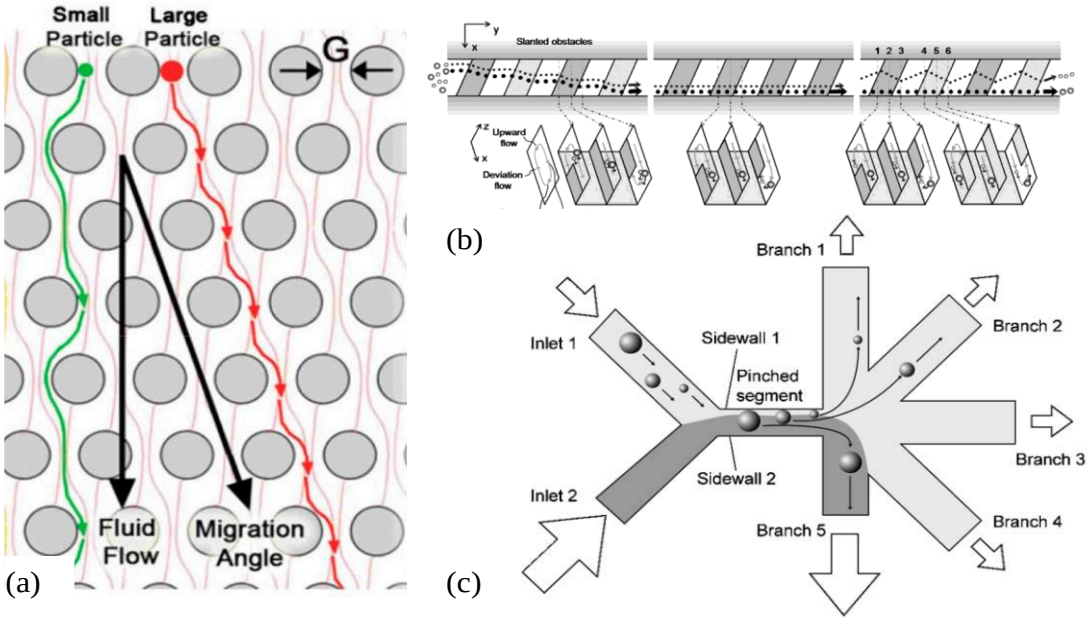

Fig. 1.1 Basic principles of hydrodynamic-based methods: (a) DLD, [3, 4] (b) hyrdophoresis, [5-7] (c) pinched flow fractionation[8, 9]

Hydrophoresis is a separation method that employs particle motion influenced by pressure fields created by microstructures. It typically employs a microfluidic device with sloped obstacles to create lateral pressure gradients that induce helical recirculation, concentrating microparticles at various lateral locations based on their size or deformability (as shown in **Fig. 1.1b**). The slanted obstacles are formed at the bottom and top of the channel. As the particles pass through the inclined obstacles placed alternately at the bottom and top of the channel, they are focused along the direction of the focusing flow to the side walls. The second region only has inclined obstacles at the channel's bottom. Only the continuous obstacle at the bottom causes the flow to rotate clockwise. The particles are at the bottom of the channel due to the downward rotating flow. The relative size differences between the particles and the inclined obstacle and the top or bottom of the channel determine the extent to which the particles deviate from the concentrated position in the third region. The obstacle aligns the large particles in the obstacle gap at the Z-center. The rotating flow has no deviated flow, which keeps the large particles in the focal position. Small particles follow the focused and deflected flow oscillations caused by exposure to the rotating flow's lateral pressure gradient along the X-axis. Hydrophoresis also has a high

separation resolution, as Sungyoung Choi et al. demonstrated by completely separating polystyrene microbeads with diameters of 9 μm and 12 μm using the Continuous hydrophoretic system.[5]

PFF introduces particle suspensions of varying sizes into the main microchannel via side microchannels. The flow rate was adjusted to sandwich the particles in a narrow stream against the wall so that the centers of all particles were on different streamlines due to size differences. The particles of different sizes are separated by a greater lateral distance relative to the expansion in the sudden downstream expansion. Hydrodynamic filtration uses a similar operating principle to introduce particle suspensions from a single inlet of a microchannel with multiple vertically branched outlets. The initially dispersed particles are gradually aligned along the side walls by repeatedly withdrawing a small portion of the liquid from the main flow through the branch outlet. Small particles enter the branch outlet before large particles because they are closer to the sidewall downstream of the microchannel. As a result, this technique allows for simultaneous particle separation. Junya Takagi et al. successfully separated red blood cells from blood using asymmetric pinched flow system (shown in **Fig. 1.1c**) and sorted a mixture of 1.0–5.0 μm particles depend on the size.[8] PFF has a limited sample yield because of the high sheath-to-sample flow ratio. As a result, these techniques are frequently used to process small volumes of samples.

Hydrodynamic based methods utilize size and deformability of the bioparticles. If bioparticles have a significant size difference, they can be moved to different locations in the microfluidic network. A characteristic of bioparticles is that they do not have a single size; instead, they have a size distribution. The operational and selection accuracy of these hydrodynamic based methods are reduced when two different populations of bioparticles have size overlap. Label-free is the most significant advantage of the hydrodynamic based methods.

1.1.2 Electrokinetic based methods

Another option for manipulating particles is the use of the electrokinetic motion of the particles and cells, which refers to the migration of electrically charged cells or particles in liquid solution or suspension in the presence of an applied electric field usually provided by immersed electrodes. There are two important phenomena applied to electrokinetic based methods, electrophoresis (EP) and dielectrophoresis (DEP). Electrophoresis (EP) is caused by the Coulombic force (electrophoretic force) acting on a particle with a surface charge to move it through an electric field. In order to utilize EP, the particles need to be charged, and the applied electric field must be constant or direct current (DC).

EP is commonly used in traditional separation techniques such as capillary electrophoresis(CE) to separate DNA and proteins.[10] As shown in **Fig. 1.2a**, a typical capillary electrophoresis system includes a high-voltage power supply, a sample introduction system, a capillary tube, a detector, and an output device. Each electrode is connected to one side of the high voltage power supply. These electrodes aid in the generation of an electric field, which initiates the migration of the sample from the anode to the cathode via the capillary tube. As shown in **Fig.1.2b**, the cells were injected by electroosmotic flow through the first capillary to a cell lysis junction. The resulting cell lysate migrated into the second capillary, where the major proteins, hemoglobin and carbonic anhydrase were separated by capillary electrophoresis and resultant analyte zone were detected by laser-induced fluorescent detection system. Xuan and Li demonstrated a microchip for selective dispensing of microparticles[11]. The particle suspension was electrokinetically focused into a slim stream. The dispensing was manually triggered by an instant electrical pulse perpendicular to the focused particulate flow in a double-cross microchannel as shown in **Fig. 1.2c**. Reichmuth et al. illustrated an electrophoretic immunoassay microfluidic chip for simultaneous virus concentration and detection using in situ nanoporous membranes [12]. Electrophoresis through the membrane separated and removed the excess antibodies from the antibody–virus complexes. This system offers a sensitive method for rapid and portable virus detection in livestock screening applications.

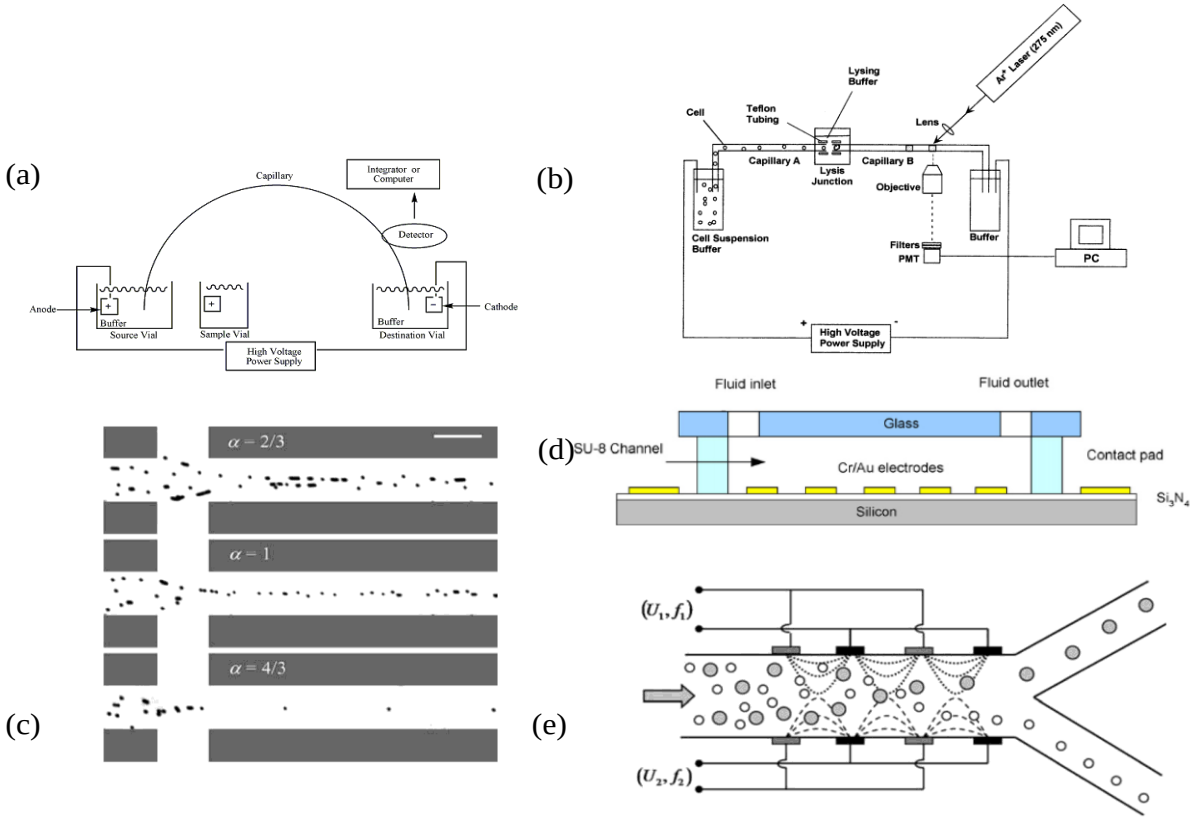

Fig. 1.2 (a) Schematic of a typical capillary electrophoresis system. [10] (b) Schematic of instrumental setup for high-throughput CE analysis of single cells.[11] (c) Electrokinetic focusing with concentrated particles at different voltages. [12] (d) Schematic diagram of the DEP device (cross section). [13] (e) Principle of the DEP switching design. Particles are flowing through the channel by the free flow in the DEP switching zone, force balance plots are shown for the particles with negative DEP properties in the switching region. [14]

DEP is the movement of particles in a non-uniform electric field due to the interaction of the dipoles of the particles and the spatial gradient of the electric field. The DEP response of the particles can switch from negative-DEP (nDEP) to positive-DEP (pDEP) depend on the working frequency. A DEP-based microsystem for the selective manipulation and separation of bioparticles using dielectrophoretic effect was demonstrated [13]. An array of microfabricated interdigitated electrodes lining on the bottom surface of a microchannel (**shown in Fig.1.2d**) is used to generate the electric field of high gradients. When working frequency is greater than 5 kHz, particles under positive DEP were attracted to the edges of the electrodes. When working frequency is smaller than 5 kHz, particles under negative DEP were repelled away

from the electrodes and levitated at certain height above the electrodes. In the same year, Wang et al. designed a novel electrophoretic switching with vertical electrodes on the sidewalls of the microchannel to dynamically manipulate the particles. [14] As shown in **Fig. 1.2.e**, A set of mutually occluding electrodes on the sidewalls of the microchannel is used to generate a non-uniform electric field to produce a negative DEP force that repels the beads/cells from the sidewalls. The opposite DEP forces are generated by another set of electrodes on the opposing sidewalls. The applied voltage and frequency can tune these lateral negative DEP forces. By manipulating the coupled DEP forces, the particles flowing through the microchannel can be positioned at different equilibrium points along the width direction and continue to flow into different exit channels.

However, there is a challenge to predict the electrophoretic motion of bioparticles in an electric field as the biological basis of the dielectric characteristics of bioparticles is not known. In electrokinetic-based applications, the presence of an electric field induces Joule heating in the fluid. Depending on the electrical conductivity of the buffer solution and the strength of the buffer solution and the electric field, Joule heating effects can be severe and result in severe thermal effects that can lead to deterioration of system performance.[15] In addition, Joule heating may also lead to undesired electrothermal effects, affecting the flow field within the microchannel.[16]

1.1.3 Magnetic based methods

The basic principle of magnetic based manipulation is based on the difference in magnetic susceptibility between the cell of interest and the surrounding environment. Movement of cells under a magnetic field is usually referred to as magnetophoresis which can be performed in two ways.[17] Cells are migrated to a region of high magnetic field strength (positive magnetophoresis) or escape from such a region (negative magnetophoresis). Since most cells are not inherently magnetic in nature, researchers generally exploit extrinsic magnetic properties for positive magnetophoresis by labeling cells with magnetic nanoparticles (MNPs) particles (as shown in **Fig. 1.3a**). The demand for effective in vitro cell detection and sorting

platforms has grown with the growing demand for cancer and infectious disease diagnostics, rare cell enrichment, environmental safety, and public health monitoring. As a result, several magnetic cell separation and detecting methods and equipment have been created. The majority of magnetic cell separation technologies rely on antibody-coupled magnetic labels to target surface antigens on cells. (as shown in **Fig.1.3b**) Majid Hejazian and Nam-Trung Nguyen demonstrated a micro magnetofluidic device that consists of a straight channel sandwiched between two arrays of permanent magnets for the size-selective concentration of non-magnetic particles in 2016.[18] Particles with diameters of 3.1 μm and 4.8 μm are discriminated and separated successfully. Brian D. Plouffe et al. constructed a microfluidic magnetophoretic cell separation platform as shown in **Fig.1.3d**.

In the channel, laminar flow is applied in the y-direction over a separation chamber and a magnetic field is applied in the x-direction. Nonmagnetic material follows the direction of the laminar flow, whereas magnetic particles/cells are deflected from the outside streams to a center collection stream (Fig. **1.3e)**. They successfully isolate 50 MCF-7 cells from whole blood with collection efficiencies greater than 85% and purity greater than 90% using this system.[19] Resident endothelial progenitor cells and hematopoietic stem cells were also isolated from whole blood with high efficiency (＞90%) rapidly (240 μL/min).[19] Another immunomagnetic microfluidic sorting was performed for the isolation of mouse lung multipotent stem cells (MLSCs).[20] First, an external magnet was used to guide magnetically-labeled cells (CD45+ and CD31+) into the isolation zone of the microfluidic platform, whereas unlabeled cells flowed through the unlabeled cell zone. Second, unlabeled cells were extracted and tagged with Sca-1 (Stem cell antigen-1) antibody that was FITC-coupled. MLSCs (CD45-, CD31-, and Sca-1+) were then collected at the isolation zone using anti-FITC magnetic beads. The FITC signal determined that the efficiency was 96–99 percent, and isolated MLSCs preserved their ability to self-renew and differentiate.[20]

Magnetic cell manipulation techniques have also been used for two- and three-dimensional cell cultures. Lin et al performed a 3D cell spheroid culture to mimic the tissue specificity of cells.[21] The cells were guided into the spheroids using magnetic force to form a three-

dimensional arrangement of cells in a non-contact pattern. Ghosh et al. used magnetophoresis to aggregate cells into spheroids by assembling cells at a location on the surface of the culture chamber above a permanent magnet for a multi-step seeding process (**Fig. 1.3f**), where the shape of the cell cluster is determined by the cell type used in 2016.[22] Positive magnetophoresis can also assemble cells at the air-media interface by magnetic levitation (**Figure. 1.3g**). Souza et al. reported in 2010 that this suspension-based 3D cell culture method using bioinorGaNic hydrogel hydrogels composed of filamentous phages, MNPs, and gold nanoparticles treated cells suspended with permanent magnets at the air-media interface and spatially varied by magnetic fields to manipulate the formation of different three-dimensional geometries and cell compositions.[23]

Magnetic based methods have several advantages over other methods. First, the technique is non-contac. Second, the generation of magnetic fields does not depend on complex or expensive instrumentation. Third, magnetic manipulation is less sensitive to internal and external factors such as ionic strength, surface charge, pH and temperature. Magnetic fields are an important component of the magnetic-based manipulation system, and both positive and negative magnetic forces affect living cells differently. Some cellular processes are affected by magnetic fields, such as membrane properties[24], cell shape and cytoskeletal orGaNization.[25]

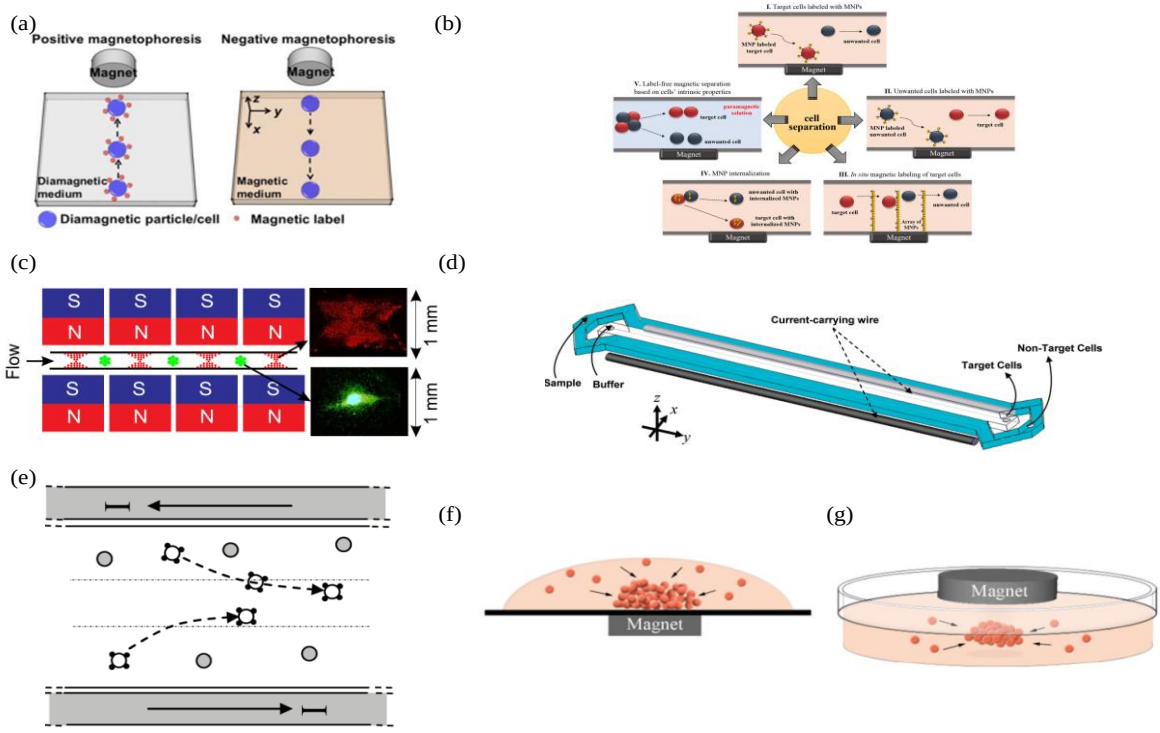

Fig. 1.3 (a) Schematic illustration of positive and negative magnetophoresis. [17] (b) Schematic illustration of microfluidic-based cell isolation methods. (I) Target cells labeled with MNPs, (II) Unwanted cells labeled with MNPs, (III) Magnetic labeling of target cells, (IV) MNP internalization, and (V) Label-free magnetic separation based on cells' intrinsic properties.[18] (c) Schematic of the size-selective traps for non-magnetic particles, green dots represent large particles, and red dots represent small particles. [19] (d) Schematic illustration of the cell separation design. [20] (e) Principle of magnetophoretic cell separation. [21] (f) Magnetic force-based manipulation of magnetically labeled cells (positive magnetophoresis) and label-free diamagnetic cells (negative magnetophoresis) 3D assembly of magnetically labeled cells into a spheroid by a magnet under the culture chamber, (g) on the top of the culture chamber. [22]

1.1.4 Optical based methods

When light is incident on a surface, a force is generated on that surface. Since the intensity of optical forces is relatively small, ranging from femto- to nano-Newtons, they are only effective on microscopic objects ranging from a few tens of nanometers to a few hundred micrometers. The invention of optical tweezers facilitated the use of optical forces to manipulate physical objects by Ashkin and his colleagues.[26, 27] Optical tweezers use the force exerted by a strongly focused Gaussian laser beam to capture small objects.[28, 29] The optical force working in optical

tweezers is usually described as the sum of two components: a "scattering force," which pushes the particle along the direction of propagation of the incident light, and a "gradient force," which pulls the particle toward the highest intensity region.[30] As shown in **Fig. 1.4a**, when a beam focused by a high numerical aperture lens is incident on a particle with a diameter smaller than the wavelength of the light wave (1), the particle is subjected to a scattering force ($\mathbf{F}_{scat}$, red arrow), which pushes the particle along the propagation direction of the light, and a gradient force ($\mathbf{F}_{grad}$, black arrow) to bring it into focus. When the particle diameter is larger than the wavelength of the light (2), the particle acts as a refractive object.[31] A change in the direction of each ray corresponds to a change in the momentum of the light and an equal opposite change in the momentum of the bead. The reflected light loses the forward momentum gained by the bead, resulting in a net force ($\mathbf{F}_{reflection}$, red arrow) that pushes the bead in the direction of the light's propagation. The refracted ray is deflected forward due to the high angle of incidence, creating a momentum change and a reaction force ($\mathbf{F}_{refraction}$, black arrow) that pulls the bead towards the focal point. The particles are stably bound near the laser focus when these two forces are balanced.

Optical tweezers methods have found application in many fields including, characterizing the mechanical force in manipulating live cells,[32] cell separation,[33] assembling and orGaNizing cells,[34] and analyzing the single cell dynamics upon environmental change.[35] An interesting work using a combination of optical tweezers and microfluidic systems to classify cells was done by Wang et al in 2011.[36] As shown in **Fig.1.1b,** samples and buffers go through two separate inlets. A charge-coupled device (CCD) camera captures photos of cells as they move through the area of interest, and image processing methods identify target cells based on their size and fluorescence. The optical trap is then positioned on the target cell and moved into the buffer flow using a control signal. The trap releases the target cell when it reaches its targeted location, and it flows to the collection port, where it will be collected and studied further. The sorting throughput was raised to five particles per second using multiple optical traps (five holographic optical tweezers). Purification of a mixture of yeast cells with beads and a solution of fluorescent and non-fluorescent human embryonic stem cells confirmed the sorter's efficacy.

Li et al. presented another innovative example of a single optical tweezer for cell sorting, in which they used the same femtosecond laser to create the microfluidic chip (through water assisted surface ablation) and then to execute the optical tweezer.[37] They demonstrated a microfluidic device consisting of two micropools in which B substilis cells were controlled and sorted.

In addition to allowing particle sorting, optical tweezers allow driving fluid control within microfluidic channels by the rotation of dedicated microscopic structures. Leach et al. exploited spin momentum transfer from a circularly polarized tweezer laser beam to birefringent trapped particles.[38] They used vaterite microspheres ranging from 5 μm to 7 μm in diameter. As shown in **Fig. 1.4c,** they placed two particles on opposite sides of the channel and close to the wall, and the inverted handedness of the trapped beam caused opposite spins of the Vaterite particles and consequently a net fluid flow. This device demonstrated flow rates up to 200 fL/s with two birefringent particles rotating at 8.7 Hz and 9.2 Hz, respectively. Terray et al. used scanning laser optical trapping to implement a microfluidic gear or peristaltic pump[39]. Multiple micro-sized silica particles are moved to drive the fluid by guiding the tweezer beam through a scanning mirror. As shown in **Fig.1.4d**, pairs of particles rotate in opposite directions for gear pumps to induce a net flow. Optical based methods are also used to mechanically characterize the fluid medium from a rheological point of view. Keen et al. connected the thermal motion of numerous trapped silica micro-spheres with the viscosity at different places using holographic optical tweezers and a fast complementary metal oxide semiconductor（CMOS） camera, and examined local changes in viscosity due to the presence of boundaries.[40] As shown in **Fig.1.4e**, The objective lens, was mounted on a piezo-controller and used to both focus the trapping beam and to image the particles. A tungsten–halogen lamp and condenser were used to illuminate the sample. Trapping was achieved using a laser system. The laser was expanded to slightly overfill the aperture of a spatial light modulator (SLM) and then coupled into the tweezers system by imaging the SLM on to the back aperture of the microscope objective lens. By appropriate hologram design, this allows multiple optical traps to be created in the sample plane. The viscosity of the fluid around each

particle can be calculated by analysis of the thermal motion of the particles. Distinct advantages of using optical tweezers for these applications include non-contact force for cell manipulation, force resolution and amiability to liquid medium environments.

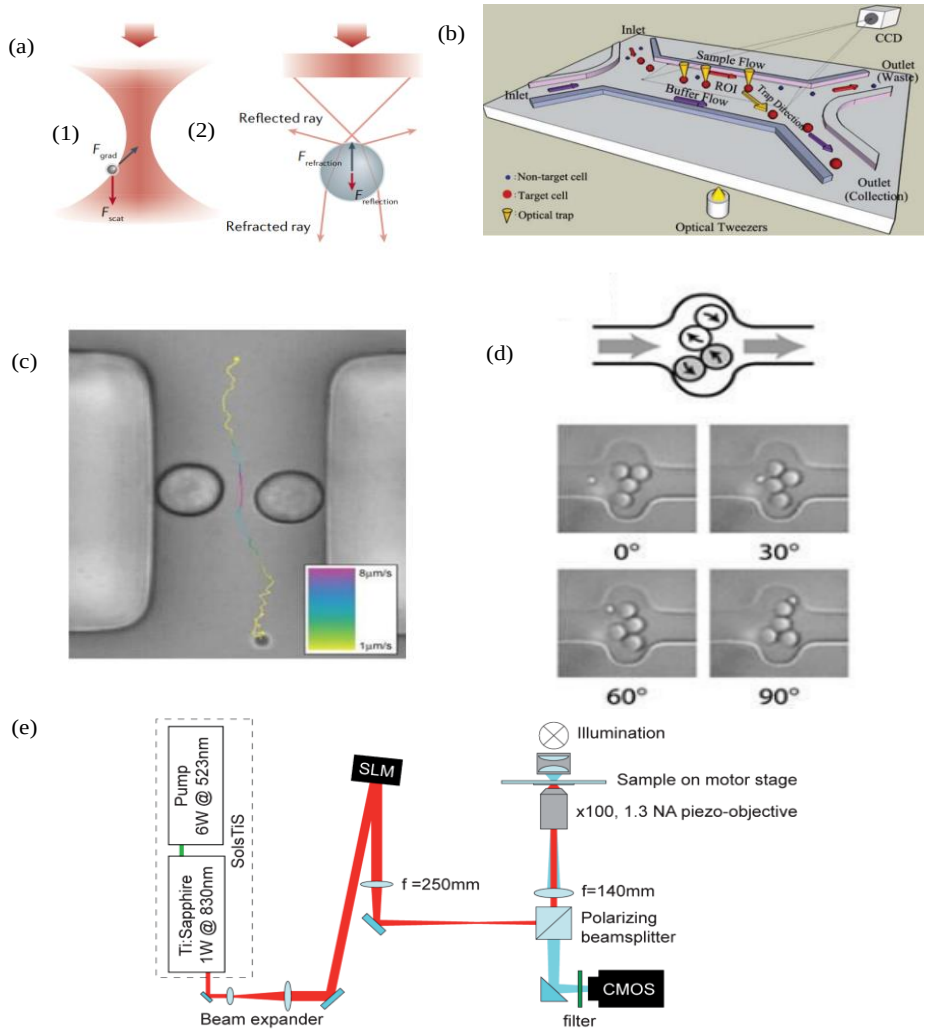

Fig. 1.4 (a) Principles of optical tweezers. [30] (b) Schematic of the cell sorting procedure. [36] (c) The traced path of a 1 μm silica particle being pumped through a 15 μm wide PDMS channel by the two trapped vaterite beads. [38] (d) Design of the gear microfluidic pump showing bead movement together with the screen shoots of 3μm silica beads 2 Hz rotation in a 6μm channel. [39] (e) set up of multipoint viscosity measurement system. [40]

1.1.5 Acoustic based methods

Acoustic based methods for manipulating particles through the use of propagating sound waves. The simple design, noninvasiveness, and non-contact, label-free nature, has made

various acoustic tweezers as an acoustic-based tool for diagnostics, therapeutics and fundamental biological research. Sound is a regular mechanical vibration that flows through many forms of materials as a waveform. When sound travels through solid materials, it usually has longitudinal or compressional waves.[41] Sound passes typically through solids, liquids, and gases, but some materials absorb a large portion of the sound waves and prevent them from propagating. Sound waves are disturbances in matter, where the individual parts of the matter may only show periodic motion while the waveform travels. All sound waves share similar characteristics since wave motion follows the same principles. The wavelength, amplitude, velocity, and frequency are used to characterize a waveform, where the wavelength is defined as the distance from one crest to the next crest or the maximum of the wave to the next maximum, the amplitude is the height of the wave given as the peak-to-peak valve, the velocity is used to describe how fast a crest is traveling from a fixed point and the frequency is the rate of a crest passing a given point. A convenient way to generate sound waves is to use piezoelectric materials and is therefore used in acoustic based methods. Piezoelectric materials can be single crystals, polycrystalline ceramics or polymers, all of which are anisotropic, where the positive and negative charges are not symmetrically arranged. The electric dipole moment allows these materials to convert electrical energy into mechanical energy, the so-called direct piezoelectric effect (**Fig.1.5a**), or the converse piezoelectric effect (**Fig.1.5b**) from mechanical to electrical energy. In acoustic fluid systems, piezoelectric materials are used to generate static and dynamic mechanical vibrations at designed frequencies. Two different wave modes are utilized to manipulate particles, including bulk acoustic waves (BAWs, **Fig. 1.5c**) and surface acoustic waves (SAWs, **Fig.1. 5d**). BAWs are commonly generated by the thickness or lateral vibrational mode of a piezoelectric ceramic element. Typically, the resonant frequency of BAWs is under 10 MHz, with a wavelength larger than 150 μm, and acoustic energy could be coupled to the fluid medium directly or through a coupling layer.[42] By designing an acoustic resonator, the particle suspended in the fluid medium can be manipulated effectively by BAWs. Acoustic manipulation based on BAWs is capable of dealing with microparticles with a high flow rate, providing a high throughput tool for particle manipulation.[43] SAWs, on the other hand, are mechanical waves travelling along the surface

of a piezoelectric substrate. The acoustic energy of SAWs is localized to the substrate surface, minimizing the input power consumption for particle manipulation (the input electronic power is typically less than 1 W). [44] SAWs are generated by interdigital transducers (IDTs), which are fabricated by standard microelectromechanical systems technology. By designing interdigital electrodes of various shapes, such as curved, straight, and slanted finger, focused, plane, and broadband acoustic fields can be achieved, respectively. As the frequency of SAWs is in the range of tens to hundreds of megahertz, the corresponding SAW wavelength is typically less than 100 μm and thus particles can be manipulated with a high spatial resolution.[45]

Compared with optical based methods and magnetic based methods described above, acoustic based methods overcome the disadvantages of a tightly focused laser beam that heats the sample by optical tweezers[26] and only manipulate magnetic particles by magnetic based methods[46]. Therefore, acoustic based manipulation is the main object of this thesis. Considering that microfluidic platforms are amazing platforms for the study of nanometer to micron-sized particles (size matched to acoustic manipulation) and most biological particles are present or suspended in liquid environment, the acoustics combined with microfluidics, acoustofluidic particles manipulations is the subject of this thesis, with its simple device design, biocompatible and non-contact operation, and label-free characteristics.

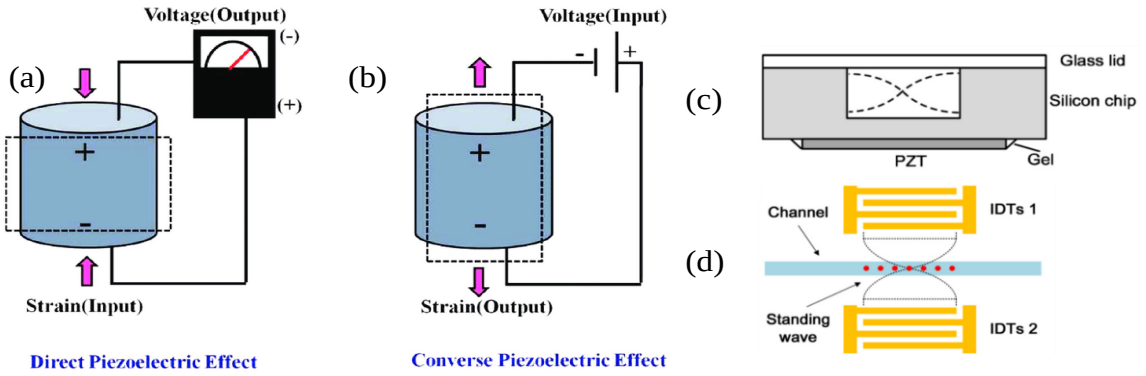

Fig. 1. 5 Schematic of (a) direct piezoelectric effect. [41] (b) converse piezoelectric effect. [41] (c) BAW mode. [42] (d) SAW mode. [44]

1.2 Acoustofluidic applications

Acoustofluidics, the integration of acoustics and microfluidics, is a rapidly growing research field that is addressing challenges in biology, medicine, chemistry, engineering and physics. In particular, the manipulation of bioparticle in fluids has proven to be a powerful tool due to the label-free, biocompatible and non-contact nature of acoustic techniques. By designing and tuning the applied acoustic field, cells and other biological particles can be manipulated in different modes for a variety of applications, including sample concentration, cell washing, cell Sorting, cell mechanophenotyping and rotation of cells. In this chapter, I discuss the application of different modes of acoustofluidic bioparticles manipulation, and outline how it has been applied to traditional applications such as cell separation, cell washing and fluorescence-activated cell sorting, as well as emerging applications, including circulating tumour cells and exosome isolation.

1.2.1 Cell Sample concentration

The enrichment of particles or live cells from diluted samples is a necessary step in bioassays. Enrichment of rare bio-particles can improve detection sensitivity and also reduce processing time. To detect bacteria in a water sample, for example, a cell culture phase is usually required, which might take from 6 to 24 hours to develop enough bacteria for analysis. The whole analysis time can be significantly decreased by using a concentration device to enrich the bacteria[47]. One of the earliest applications of acoustic waves in bioparticles manipulations was cells enrichment, as demonstrated by the Kundt tube.[48] Early experiments used a narrow vibrating driver as a resonator inside a glass tube to create a standing acoustic field. Particles in the standing acoustic field are subjected to acoustic radiation forces, and particles with positive acoustic contrast factor are pushed towards the pressure nodes of the standing wave field and trapped, resulting in local particle enrichment (**Fig.1.6a**).[49] Recently experiment

finished by Soh and his colleagues , who published a paper about an acoustofluidic cell concentrator that continuously collects cells and can handle huge sample volumes with a 1000-fold enrichment of particle/cell samples (**Fig. 1.6b**)[50]. They created an acoustic resonator with a pressure node plane perpendicular to the direction of flow. As the cell samples were placed into the flow chamber, all the cells were pushed into the center of the flow chamber (pressure node plane). The cell sample is concentrated, and the excess liquid is eliminated by creating two outlets that can collect the central and lateral liquid streams. The researchers Mao et al use a peristaltic pump to recirculate the cell samples to further increase the enrichment factor. After a complete enrichment cycle, the concentration of red blood cells and human cancer cell lines increased by a factor of 1000. They used synchrotron radiation pressure and acoustic flow to accomplish low-frequency nanoparticle enrichment within square-section glass capillaries (**Fig. 1.6c**).[51] They found a large, single vortex flow pattern at a frequency of approximately 2.6 MHz. The two forces (acoustic radiation force and drag force) did not compete, as the pressure node was equally at the center of the channel. The nanoparticles, therefore, collect in the center of the channel. Down to 80 nm, the effective concentration of polystyrene particles was demonstrated. This technique was then used to improve the detection signal of a homogeneous nanoparticle-based immunoassay. Using this acoustic flow-controlled nanoparticle concentrator, the fluorescence signal was increased by a factor of 30. Hammarstrom et al. also used low-frequency secondary acoustic radiation forces, which are generated by particle-particle interactions in close proximity, to enrich nanoparticles.[52] Then, as E. coli and nanoparticles moved between these large seed particles, they were, due to secondary acoustic radiation forces are confined and enhanced in the acoustic field. In a recent study, this method was successfully used to enrich the blood of septic patients for pathogens.[53] The bacterial enrichment procedure took less than 2 hours to complete, which is much shorter than the time required for cell culture (4.6-26.4 hours). The system's sensitivity needs to be improved to detect sepsis with low bacterial counts in the future. Extracellular vesicles from culture media, urine, and blood were enhanced similarly, demonstrating the utility of acoustic fluid methods for concentrating extracellular vesicles. Cooper and his colleagues created the SAW, which can drive droplets on a SAW substrate with a diagonal interferer. They used this

to enrich erythrocytes infected with malaria parasites in the outer ring of the droplet. Enrichment was completed in 3 seconds with an enrichment factor of 100-1000 times.[54] Extracellular vehicles (EVs) have emerged as a rich source of biomarkers providing diagnostic and prognostic information in diseases such as cancer. Ku et al. demonstrate the applicability of an automated acoustic-based technique to enrich EVs, termed acoustic trapping[55]. As shown in **Fig.1.6d**, a local λ/2 acoustic standing wave was created in a glass capillary by a piezoelectric transducer and seeding polystyrene beads were aspirated and trapped in the capillary by the primary acoustic forces (**Fig.1.6d (1&2)**). It was followed by aspiration of sample containing EVs. The EVs were attracted and trapped together with the seeding cluster by secondary acoustic forces (**Fig.1.6d (3)**). The cluster of EVs and seeding particles were washed and released into the 96-well plate when ultrasound was deactivated.[55] (**Fig.1.6d (4)**). They have successfully enriched EVs from cell culture conditioned media and urine and blood plasma from healthy volunteers using this platform.[55] The acoustically trapped samples contained EVs ranging from exosomes to microvesicles in size and contained detectable levels of intravesicular microRNAs. Gu et al. present an acoustofluidic centrifugation technique that leverages an entanglement of acoustic wave actuation and the spin of a fluidic droplet to enable nanoparticle enrichment and separation. [56] When an electrical signal was applied to the tilted IDT, the two traveling SAWs propagated along the substrate from two opposite directions and entered both sides of the droplet. Droplets can generate internal vortices when excited by small acoustic amplitudes, which intensify as the acoustic amperage increases. As the momentum accumulates, the droplet's surface tension tries to balance with the acoustic radiation pressure and centrifugal force. The droplet gradually deforms into a concave ellipsoid shape and reaches a stable spin pattern with periodic rotational boundary deformation[56]. The liquid. The particles in the droplet migrate toward the center of the droplet according to a biaxial rotational trajectory. One axis is relative to the droplet, and the other is relative to the particle. This biaxial particle trajectory follows a helical path, and the particle itself is also rotating (shown in the dashed box in **Fig1.6e** and indicated by the green arrow). By combining acoustic streaming and droplet spinning, rapid (<1 min) nanoparticle concentration and size-based separation are achieved with a resolution sufficient to identify and isolate exosome subpopulations.

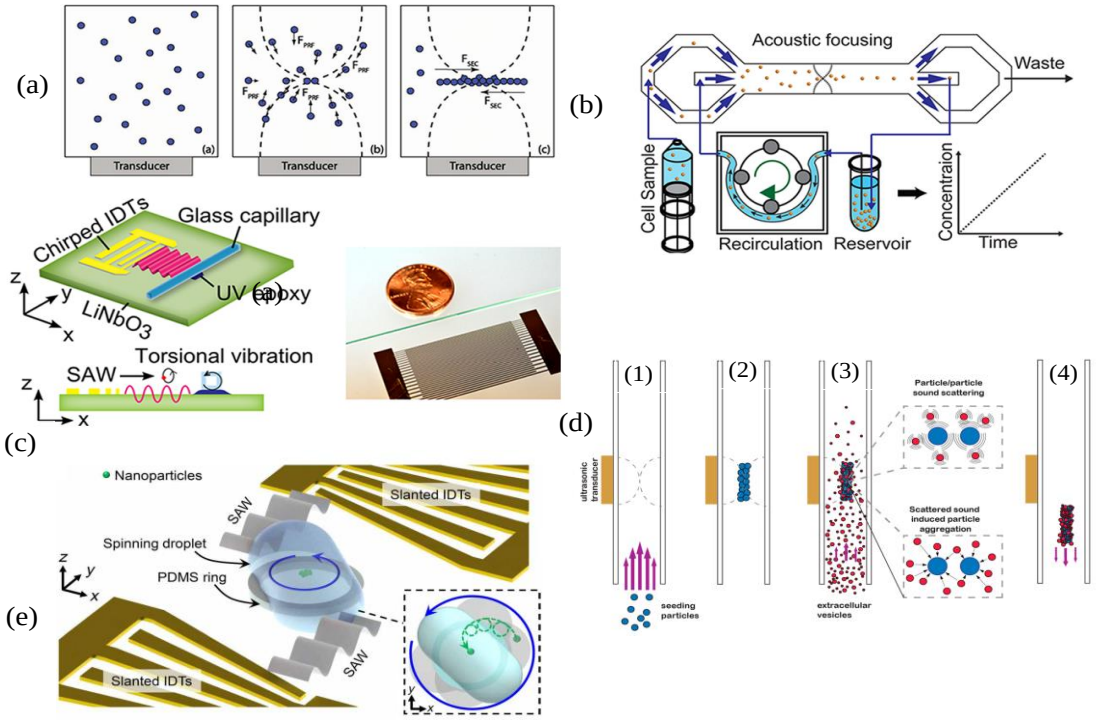

Fig.1.6 (a) Illustrations of particles being trapped in a standing acoustic wave field. [49] (b) An acoustic focused recirculating cell concentrator. [50] (c) Acoustic system capable of confining particles as small as 100 nm in diameter within a glass capillary. [51] (d) Schematic illustration of acoustic trapping for EV isolation. (e) illustration of the acoustofluidic centrifuge system. [55]

1.2.2 Cell washing

Acoustofluidic manipulation has also been utilized for cell washing, which is the process of removing cells from their original medium and replacing it with a new carrier fluid. Li et al used a tilted angle SAW to transfer inflammatory cells from a human sputum sample. [57]As shown in **Fig. 1.7(a)**, the microchannel is aligned with the IDTs at a 15° inclination. [58] When the IDTs are activated by an RF signal, two identical surface acoustic waves (SAWs) are produced and propagated in opposite directions. Within the microchannel, the interference of the waves produces a standing surface acoustic waves (SSAW) field. The tilted angle design causes the periodically dispersed pressure nodes and anti-nodes to form an angle with regard to the flow direction. The inflammatory cells in the liquefied sputum sample are subjected to

acoustic radiation forces and Stokes resistance resulting in they move towards the pressure nodes as the sample flows into the SSAW field. The inflammatory cells travelling through the SSAW field are diverted from the flow due to the angle between the pressure node and the direction of flow caused by the combination of acoustic radiation force and Stokes resistance. As a result, inflammatory cells were successfully transported from human sputum to buffer solution and collected at the top exit.[57] Li et al successfully isolated leukocytes from cell debris using a similar method.[58] Leukocytes were extracted from lysed blood samples and placed in a phosphate buffered saline (PBS) solution. The parameters of the medium must be considered in acoustic-based cell washing applications where particles are conveyed through a liquid–liquid interface. It has been established that acoustic impedance variations can cause unintended liquid redistribution, resulting in lower washing efficiency.[59] liquid redistribution can be decreased and wash efficiency enhanced by altering the acoustic characteristics of one or both liquids. In addition to actively removing particles from contaminated samples, holding the cells with sonic waves while washing them with clean media is another technique for achieving buffer medium exchange. Augustsson et al employed standing acoustic waves to keep the cells in the main channel and buffer exchange is accomplished through the progressive cross-flow of particle-free buffer from the branch channels.[60] As shown in **Fig. 1.7(b)**, before reaching the first flow junction, the particle suspension was injected through an 11-mm long acoustically active pre-focusing section of the main channel, which concrete beads or cells towards the center of the flow in a narrow band. A specified proportion of the main channel flow is aspirated from one side outlet of the channel while the same amount of fresh wash buffer is injected via the opposite inlet at the first crossflow junction. Because the particles are restricted in the channel center, they will stay in the main channel while the prescribed proportion of the carrier buffer is extracted via the side exit. On the other hand, the band of particles will migrate towards the side outlet, bringing them closer to the main channel's sidewall. After the first buffer extraction junction, the band of particles will continue to suffer an acoustic standing force. It will be centered in the center of the flow along the 6-mm long segment preceding the next buffer exchange junction. The process of exchanging the carrier buffer is repeated when reaching the next crossflow junction for 5 times to exchange

the buffer.[60]

In many biological and diagnostic applications, it is necessary to purify the cell sample to reduce the background noise of the cells. Many acoustic microfluidic systems have also been developed for cell washing and in-droplet separation of biomolecules. Park et al. presented a method acoustofluidic device (shown as **Fig.1.7c**) to achieve droplet washing by first pushing the encapsulated polystyrene particles to the end of the droplet, splitting the droplet in half, followed by merging with a second droplet and splitting in half again.[61] Liu et al. presented an interesting acoustic microfluidic system that achieves continuous background dilution in droplets containing cells with high sample recovery. [62] The system (shown in **Fig.1.7d**) includes droplet generation, acoustic focusing, droplet separation, microinjection, and serpentine mixing on the same chip. This microfluidic system can achieve background dilutions up to 4.3-fold (from 1.00 mg/ml to 0.23 mg/ml) with a particle recovery of 87.7% for polystyrene beads. Gerlt et al. designed a microfluidic system to accomplish a high throughput, (114 droplets/min) high separation efficiency (97.95% ± 1.9%) washing of yeast. In this system, as shown in **Fig.1.7e**, the nanoliter droplets containing particles are produced at a T-junction. The particles are trapped in the tip of the droplet by the interplay of acoustic forces in two dimensions and internal flow fields. The droplets are subsequently split at a second T-junction into two daughter droplets—one containing the supernatant and the other containing the corresponding particles.

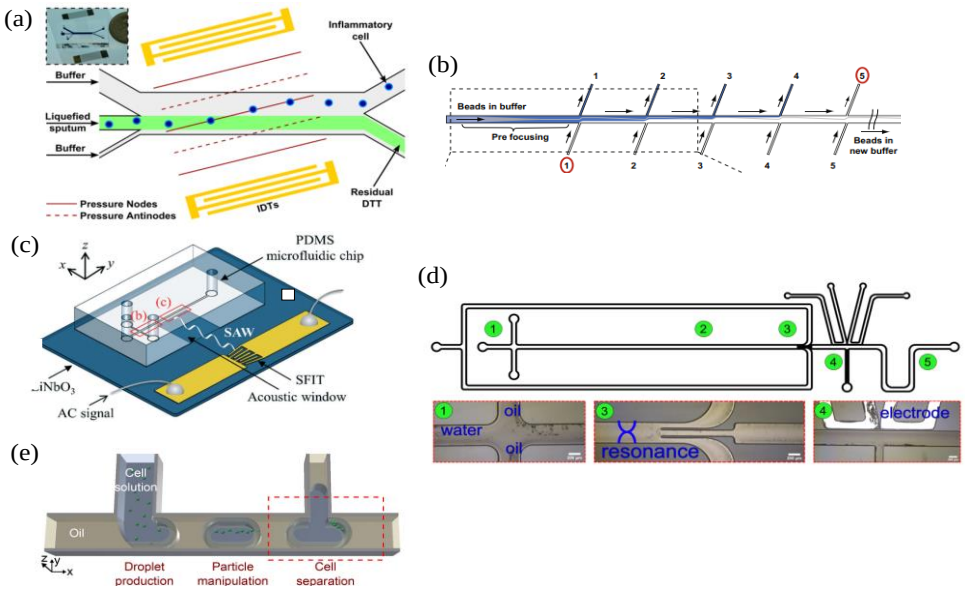

Fig. 1.7 (a) A schematic and optical image of the SSAW-based washing device. [58] (b) The acoustic washing apparatus is schematically depicted with the pre-focusing segment and the first five buffer exchange connections. The original buffer (black) is taken from the upper side of the main channel at the first four junctions, while a new colorless buffer is inserted to the lower side. Because each junction exchanges 25% of the main flow, the buffer injected at inlet 1 will end up at outlet 5. [60] (c) a perspective-view schematic diagram of the acoustofluidic device for in-droplet microparticle washing and enrichment. [61] (d)The design of the chip. The chip contains five different unit operators:(1) droplet generation, (2) acoustic focusing, (3) droplet split, (4) picoinjection, and (5) serpentine mixing. [62] (e) working principle of cell separation (washing) in nanoliter droplets. [62]

1.2.3 Cell Sorting

Cell sorting refers to sorting of target cells by properties or types from complex and heterogeneous mixtures, which is usually for downstream analysis or purifying cells into well-defined populations.[63] Many research studies have been introduced in which cell sorting has played a critical role in cell biology, cell-based diagnostics, and therapies.[64, 65] For example, in bioprinting or cell patterning, precise cell sorting and manipulating of different types of cells is done in the preparation stage.[66] Sorting of erythrocyte and leukocytes from blood has been employed to diagnose various illness such as malaria, anemia and myeloma[67]. Sorting of stem cells promotes manipulating differentiation of cells in therapy for injured tissues.[68] For the above purposes, a range of methods has been reported. Conventional cell sorting approaches

such as fluorescence-activated cell sorting (FACS), magnetically-activated cell sorting (MACS) and centrifugation methods, however the above methods are limited by the following disadvantages, use of labeled cells, large sample volumes, risk of sample contamination, long operation time, and high operating cost.[69] Extensive research studies have been made to isolate cells by employing acoustofluidics, and they have promoted development in cell sorting methods. Compared to above approaches for cell sorting, acoustic microfluidic systems have advantages of label-free and biocompatibility.[44]

The sorting throughput is an important design parameter for acoustically based cell sorting machines. Schmid et al. separated droplets and cells using a moving SAW-induced flow.[70] They used a tiny PDMS column as a coupling medium for the SAWs to limit the area of the sorting region, which allowed them to confine the acoustic flow to a modest length of about 150 μm. As shown in **Fig. 1.8a**, the droplets enter the sorting device via inlet channel A. The top and bottom focusing channels B and C send droplets into the lower default outlet I by focusing them on the middle of the channel. If a droplet passes through the interrogation region D and emits a fluorescence signal, the IDTs E generates a SAW that travels along with a narrow path F to the contact post G, where the resulting sound field directs the droplet upwards into the upper outlet H. It was stated that the theoretical maximum sorting volume was 3000 drops/s. Ding et al. demonstrated a multichannel cell sorting device based on SAW [71]. The device, as illustrated by **Fig. 1.8(b&c)**, employs chirped IDTs that a variety of frequencies can activate. Different pressure node placements can be determined by active different frequencies. The paper revealed five channels of cell sorting and a droplet sorting throughput of 200 events/sec. Ren et al devised focused IDTs to replace the commonly used parallel IDTs to improve the throughput of SAW-based cell sorting. [72]As illustrated in **Fig. 1.8d**, focused IDTs were proven to considerably shorten the length of the sorting area to less than 160 m, which enable the devices to be operated at a high sorting rate with consuming lower power. For 10 μm polystyrene particles, a practical sorting throughput of 3000 events/sec was reached. Collins et al used a 386 MHz moving surface wave to perform single particle sorting in a PDMS microchannel. [73] As illustrated in **Fig. 1.8e**, they operate single particles in continuous flow at

sorting speeds of up to 10,000 times/sec by lowering the beam size to 25 μm. Acoustic-based parallel flow cell sorting is a promising way for breaking past the present throughput restriction of 50,000 events/s, which utilize an acoustic standing wave to focus multiple parallel particle streams. Easy handling and high output throughput potentially make acoustic FACS to be a more appealing method for rare cell characterization, collection, and subsequent downstream culture.[74] Ren et al suggested a sheathless FACS system that uses a SAW-based cell focusing device as shown in **Fig. 1.8f**.[75] This device changes the cell from its initial trajectory to the nearest pressure node in the cell focusing area via the x and z components of the acoustic radiation force. Three-dimensional focusing is achieved by carefully controlling the relative placements of pressure nodes and cells. A winding channel is placed between the entrance and the SSAW focus area on this case to cause the cells to pre-concentrate around the selected pressure node; it can also prevent the cells from clustering together and establish a regular spacing between neighboring cells.[76] The focused cells are then interrogated by an in-plane integrated optical detection system using a single-mode fiber (SMF) connected to the laser and a multi-mode fiber (MMF) connected to a photomultiplier tube. The SSAW-based cell deflection device is activated when fluorescently labeled cells are detected and enter the deflection area. The pressure node of the deflected SSAW field is moved and aligned with the collection outlet in comparison to the pressure node of the focused SSAW field. As a result, the battery is pushed to a new equilibrium point in the deflection area before being discharged via the collecting outlet. Sorting of mammalian cells (HeLa) was successful by this device, with a sorting purity of more than 90% and an output of 2500 events/sec.

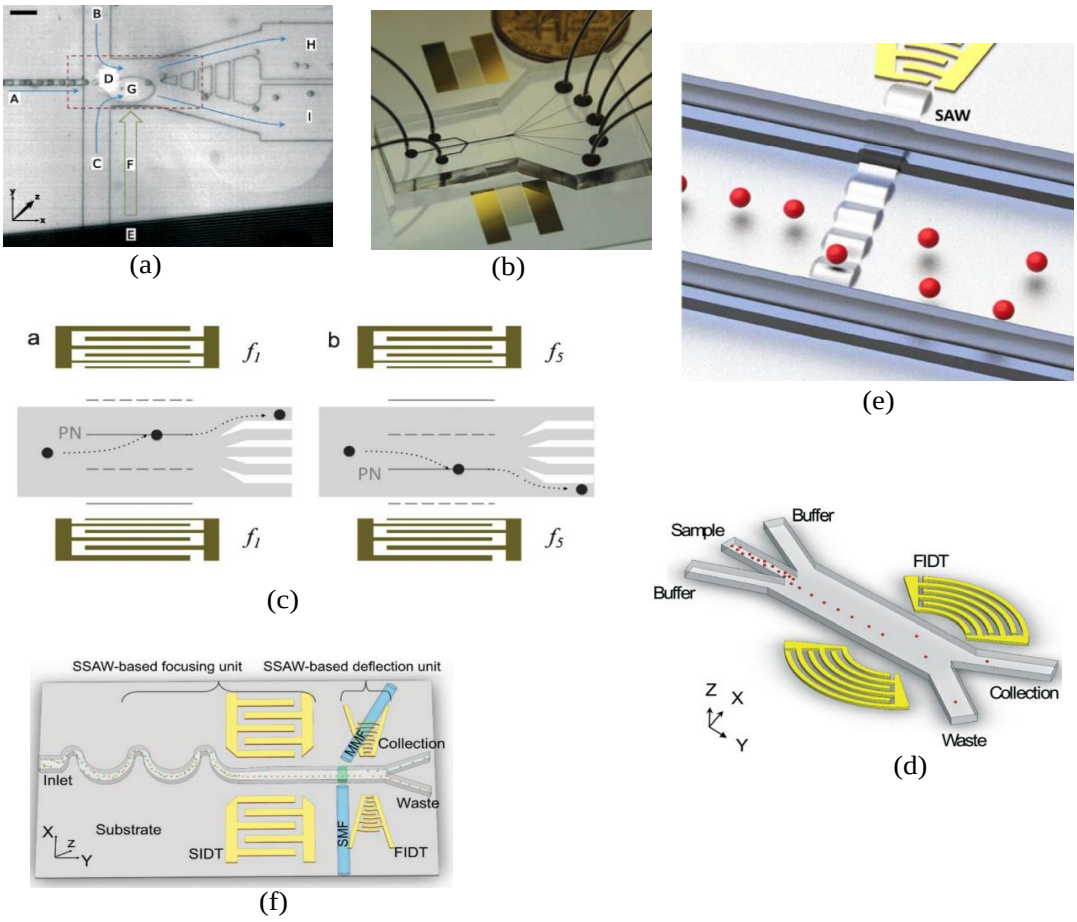

Fig. 1.8 (a) Top view of the droplet sorter setup. Droplets enter the sorting apparatus via channel A. The top and bottom focusing channels B and C send droplets into the channel's center, directing them toward the lower default output I. Suppose a droplet passes through the interrogation region D and emits a fluorescence signal. In that case, the interdigitated transducer E generates a surface acoustic wave (SAW) that travels along with a narrow path F to the contact post G. The resulting sound field directs the droplet upward into the upper outlet H. [71] (b) An optical picture of the SSAW-based cell-sorting device with 3 inlets and 5 outlets. [72] (c) Working mechanism of the SSAW-based cell-sorting device. When the SSAW is switched on at frequency of f_1 and f_5, all particles/cells are driven to the pressure node (solid lines) and directed in the upper or bottom outlet. [72] (d) A schematic illustration of an acoustic sorting device that uses focused IDTs. The center intake is infused with a sample solution containing the cells/particles to be sorted, while both side inlets are injected with a buffer solution. [73](e) A schematic illustration of an acoustic sorting system utilizing moving SAWs and focused IDTs. [74] (f) Schematic of the SSAW-based FACS chip. [75]

CTCs are cancer cells that leave the primary tumor and enter the circulatory system, where

they might spread to form secondary tumors[77]. These cancer cells can help researchers better understand the causes of cancer metastasis and provide crucial information for cancer diagnosis and treatment. CTCs can be used which are separated from peripheral blood in a timely and effective manner. Augustsson et al used a two-stage acoustic fluid separation platform with a pre-alignment module and a separation module to demonstrate the separation of cancer cells from WBCs in 2012. [78] With recoveries of 72.5-93.9%, purity of 79.6-99.7%, and a throughput of 70 μL/min, cultured cancer cell lines were mixed into WBCs and separated by this device. Latterly, Antfolk et al used an enhanced platform to obtain 94.8 ± 2.8% cancer cell recovery and 2.2 ± 0.6% WBC contamination.[79] A concentration module was introduced following isolation in another study by the same group.[80] A complete separation process is shown in **Fig. 1.9a**, 5 and 7 μm polystyrene particles are injected into the inlet (a) and pre-aligned in horizontal and vertical dimensions (y and z). Through the inlet (b), cell-free liquid is introduced and the 5 μm PS beads are separated in the separation channel and refocused in the concentration channel (1) when the 7 μm beads are ejected through the outlet. 5 μm beads are then ejected through the outlet (3) and the cell-free liquid is collected (2). Magnusson et al. created a clinical-scale automated acoustic flow control device that could handle 5 mL of erythrocyte-removed paraformaldehyde-fixed blood (1:2 dilution) at a flow rate of 75 μL/min with an 86.3% recovery rate and 162-fold enrichment for breast cancer cell line cells.[81] Zalis et al used a similar platform to Augustsson's work to show that live cancer cells may be distinguished from dead cancer cells. [82] Previous research has shown that contaminated cancer cells can be separated but dealing with patient samples is more difficult because CTCs in peripheral blood are extremely rare (typically less than 100 cells in 1 mL of blood). As illustrated in **Fig. 1.9c**, Li et al used the title-angle SAW approach to isolate CTCs from clinical patient samples at a rate of 20 μL/min.[2] Wu et al recently demonstrated a high throughput (125 μL/min) acoustic platform for CTC isolation to boost processing speed. They changed the channel configuration and optimized the operating parameters of the SAW-based vertical separation platform, as illustrated in **Fig. 1.9d**.[83] A vertical acoustic resonator was made by placing a piece of glass into the fluid channel's roof. As a result, acoustic reflection at the fluid-glass contact dramatically enhances the sound pressure intensity, allowing for faster processing

in practical applications.

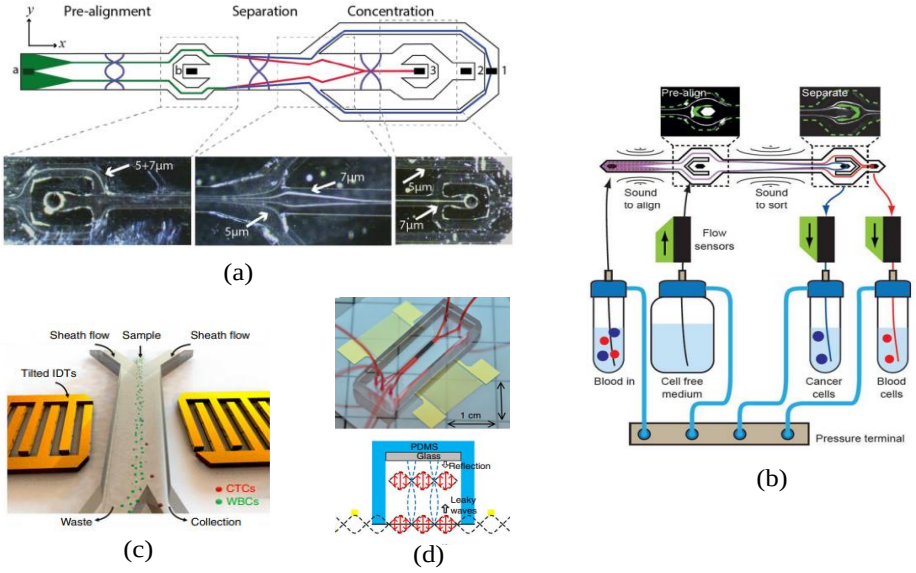

Fig. 1.9 (a) An integrated acoustic separator with prefocusing, separation, and concentration units. [81] (b) The separation principle within the chip and the external fluidic components of the acoustophoresis cell separation platform are depicted schematically. Individual sample reservoirs are inflated individually using a computer-controlled multichannel pneumatic terminal. An aqueous suspension of cells (shown by red and blue circles and lines) from the sample input tube through the pre-focusing channel enters the chip. [81] (c) Circulating tumor cells (CTCs) are separated from WBCs by using a tilted-angle SAW-based device. [82] (d) High-throughput isolation of CTCs by using standing SAW and PDMS/glass hybrid channel. [83]

1.2.4 Cell mechanophenotyping

Interrogating the mechanical properties of cells and microorganisms reveals a multitude of insights into their state. Hence, such measurements have been used to obtain stem cell differentiation stage[84], disease progression in blood-related pathologies such as sickle cell disease[85] and provide insight into the metastatic propensity of tumor cells.[86-89] The mechanical characteristics of cells are expressed using biomechanical properties such as deformability, Young's modulus, and compressibility. Atomic force microscopy (AFM) are commonly used to measure these mechanical properties but the throughput is low and (approximately 1 cell/min).[90], which precludes this technique from being used for characterization of large cell populations. Furthermore, the application of force via a sharp tip risk damaging the

interrogated cells and as such makes any viability-dependent processes downstream less feasible. Acoustic microfluidics becomes an excellent tool for cell mechanophenotyping because of its contactlessness and biocompatibility. For example, Xie et al established a method for deforming and evaluating the deformability of cells suspended in an auditory flow field using acoustically oscillating bubbles. In a single experiment, their approach evaluates the average deformability of hundreds of HeLa, HEK, and HUVEC cells (**Fig. 1.10(a&b)**). Furthermore, a paper demonstrated that the stiffness (i.e., elastic modulus) of a single suspended cell could be measured by the change in the resonant frequency of a suspended microchannel resonator via acoustic scattering of waves [91] as shown in Fig. (**Fig. 1.10c**), they correlated frequency shifts and cell mechanical properties (stiffness, Young's modulus) by acoustic scattering and evaluated changes in mechanical properties of L1210 cells during mitosis. Acoustofluidics also offers a one-of-a-kind method for measuring cell compressibility using acoustic radiation force. Hartono et al studied the compressibility of several cell types by recording the trajectory of cells in the acoustic field.[92] To determine the compressibility of cells, a mixture of cells and polystyrene beads was flowed into the channel, and their trajectories under acoustic radiation were recorded. The trajectory of the bead is mapped to the energy-acoustic density. At the same time, the experimental trajectory of a specific cell was also tracked. The size of the cells can be measured under a microscope, and their densities are taken from the literature. Since the movement of the cells and the polystyrene beads are carried out together, they are considered to be subjected to the same sound field. Therefore, they have the same energy acoustic density and then use the energy acoustic density value calculated from the polystyrene beads to minimize the difference between the experimental and simulated trajectories of the cells by fitting with the compressibility of the cells to get the compressibility of the cell. Cancer cells compress more than normal breast cells, implying that compressibility could be utilized as a diagnostic biomarker.[93]. Wang et al. injected cells from the same initial position to simplify the experiment, with a piezoelectric transducer at the bottom of the linear flow channel, creating an acoustic field within the channel, and a downstream imaging camera to record the exit position of the cells. As the cells enter the main channel, they can move in the lateral Y direction under the acoustic stretching force. To improve the consistency of the

cell entry point, a hydrodynamic flow focusing system is used in the side channel. Thus, the cells are first aligned to the center of the side channel before entering the main channel so that the cells are always introduced to the same position in the acoustic field. [94] After calibration, they discovered variations in multiple cell lines at a throughput of 10 cells per second (**Fig. 1.10d**) and mechanophenotype the head and neck cancer cell lines 37B, M4e, and Tu686 with a 20–30% overlay. In another study, Augustsson et al. used the acoustic impedance of cells to evaluate their mechanical properties. Cells flowing through a microchannel migrate laterally under the influence of an acoustic field into a stream with increasing acoustic impedance. Finally, individual cells reach their iso acoustic point (IAP), at which the acoustic contrast between the cell and the surrounding fluid becomes zero and lateral displacement ceases. When reaching the end of the microfluidic channel, the lateral position of individual cells can be recorded and then translated into an effective cellular acoustic impedance, since at this point the impedance of the cells is equal to the impedance of the medium (**Figure 1.10e**). This method was applied to measure the effective acoustic impedance of monocytes, lymphocytes, neutrophils, BA-F3 and MCF7 cells. It shows a great variation in different cell lines. (**Fig. 1.10e**).[95] The measurement of thousands of individual suspension cells were only cost a few minutes which make this a suitable method for high throughput mechanophenotyping of cells.

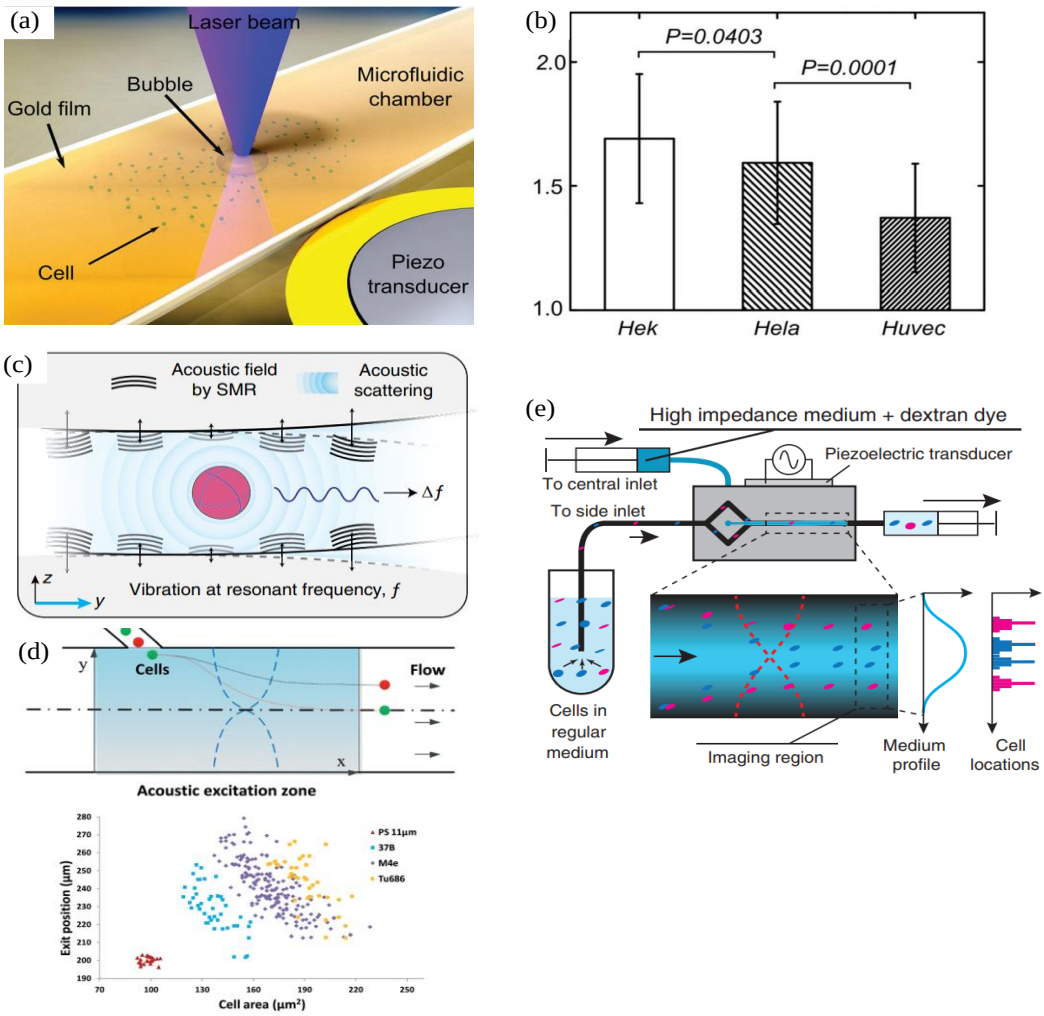

Fig. 1.10 (a) schematic for the configuration of microfluidic chamber and piezo transducer. [90] (b) statistical analysis indicated that the HEK cell has the largest deformability, while HUVEC has the least deformability. [90] (c) A conceptual illustration of frequency shift due to acoustic scattering. A particle interacts with acoustic fields (black waves) generated by the SMR vibration (black arrows) at resonant frequency *f*. The particle–fluid interaction causes acoustic scattering (blue waves), which shifts the resonant frequency. [91] (d) Working principle of the acoustofluidic cytometer. Cells are introduced from the side inlet into the acoustic resonance field, where cells with different biophysical properties (such as size, density and compressibility) experience different acoustophoretic forces while passing through the acoustic resonance field, and therefore exit at different Y-positions. Red spheres indicate cells that have a smaller acoustic contrast factor compared to the cells shown as green spheres. Scatter plot of the cell size (in the form of cross-sectional cell area) and cell exit position (Y-direction) of head and neck cancer cell lines to quantify and group the cells based on their different biophysical properties. (n = 290). [94] (e) Schematic of the size-insensitive acoustic-mechanical phenotyping system. [95]

The acoustic contrast factor of a defined acoustofluidic system reflects the properties of the

bioparticle and the medium in terms of density and compressibility.[96] It is an essential parameter to determine the magnitude of the acoustic radiation force and its sign determines whether a bioparticle will move toward the pressure node (PN) or the antinode (AN). For example, using surfactant to modify the sign of the acoustic contrast factor, Zhao et al. has managed to migrate 300-nm particles from the PN to the AN. [97] Owning to the opposite sign of the acoustic contrast factor, standing surface acoustic wave (SSAW) is able to separate lipoproteins from extracellular vesicles without labelling.[98] Other studies utilised the migration trajectory to derive compressibility of living cells. Wu et al dragged microparticles and cells towards the microfluidic channel sidewall at different segments to calculate the compressibility.[99] The same group also demonstrated the compressibility of three cell types measured by fitting the trajectories.[100] Continuous flow-based acoustofluidic method has characterised various cell types by registering the position when cells leave the acoustic field.[94] Acoustofluidic methods for mechanical phenotyping of cells have demonstrated the advantages in simplicity in the measurement system setup and less dependent on high-profile cameras. By registering the displacement trajectory of the single-cell in the acoustofluidic device, its acoustic contrast factor or other acousto-mechanical properties can be derived.

1.2.5 Rotation of cells

Precise rotational manipulation of particles, cells and multicellular organisms is an essential capacity in biotechnology that impacts various disciplines including single-cell analysis[101], drug discovery[102] and organism studies[103]. For example, distinct rotational behaviors due to different cell morphologies has been identified as a potential diagnosis method.[104] Providing three-dimensional (3D) interrogation, rotational manipulation can reveal hidden genetic, cellular and structural details that are vital in small organism phenotyping[105], screening[106] and microsurgery[107]and which are not visible in typical translational manipulation.

Optical tweezers are widely used to generate rotational manipulations, but their results are limited by the physiological damage to cells and other biological samples due to laser-induced heating.[108]Acoustofluidic methods with three-dimensional rotational have been developed to

circumvent these constraints. In this case, the body of interest rotates with the acoustics, and a single static view captures a planar image throughout the revolution which enables hidden features to be discovered. Ahmed et al rotated cells and model organisms using the sonic flow created by oscillating bubbles triggered by acoustic wave.[109] As in **Fig.1.11a**, a PDM-based microfluidic channel and a piezoelectric transducer are combined, which captures air microbubbles when the fluid is injected. A piezoelectric transducer mounted on a glass sheet next to the channel generates acoustic waves. When the trapped microbubbles are exposed to an acoustic field with a wavelength much larger than the diameter of the microbubbles, oscillations are generated, which in turn generate acoustic streaming, such oscillating bubbles in can be excited to generate different acoustic streaming pattern (vortexes) to rotate the cells. The author demonstrated cell rotation around a variable axis that is dependent on bubble size and excitation frequency in this work. Furthermore, they were able to precisely rotate the model creature Caenorhabditis Elegans (C. Elegans) with a transducer pulse of 5 milliseconds. Individual dendrites can be spotted using a fluorescent microscope along the length of the worm due to this rotation. Similarly, Tang et al. describe an ultrasonically actuated, bubble-array-based method to rotate a large number of cells simultaneously and separately in controlled space. [110] As shown in **Fig.1.11b,** they set up each rotating unit as a horseshoe structure for capturing microbubbles and generating the acoustic streaming needed for cell rotation and arrayed them to increase throughput. Rotation of the Hela cells at 120 rpm was accomplished using this structure. A drawback of these microbubbles-based methods is their enlargement over time, which eventually shifts their resonance frequency.

Specific channel structures and surface acoustic waves can also generate acoustic streaming to rotate objects to overcome this drawback. Feng et al. designed an ingenious channel structure to perform the rotation.[111] As shown in the **Fig.1.11c**, the structure consists of a PDMS microchannel with six microstructures and a piezoelectric transducer providing acoustic energy. Inlet and outlet holes are punched in the PDMS chip for loading and unloading cells. The length, width and depth of the microchannels are 5 mm, 1 mm and 200 μm, respectively, and each microstructure is designed to have a constant length of 400 μm, a tip

angle (θ) of 20◦ and a depth of 200 μm to generate acoustic streaming for cell rotation. Diatom cells and swine oocytes were rotated using this structure with different vibration modes. Zhang et al recently used SAWs to achieve C. elegans rotation (**Fig.1.11d**).[112] When the IDT on one side is activated, a traveling SAW is generated. The traveling SAW then propagates into the PDMS microchannel and induces an acoustic steaming inside it. The induced acoustic streaming creates a vortex inside the PDMS microchannel that can be used to rotate C. elegans in a certain direction. The direction of rotation depends on which side of the IDT is activated. They employed a 1.5-millisecond signal pulse to produce four rotation angles and exhibited the rotation in a continuous stream (**Fig. 1.11d**).

In addition to utilizing the method using acoustic streaming, parameters modulation of the acoustic wave is also used for the rotation operation. Here, a single parameter (direction, amplitude, phase) parameter is slowly varied with time. These methods were investigated by Schwarz et al. For direction modulation, a hexagonal chamber and the device is developed as shown in **Fig. 1.11e**, the drive consists of three independent piezoelectric transducers aligned with the fluid wall. By selectively driving one of the piezoelectric sensors, a standing wave can be driven in one direction, and the particles in it are rotated by the switch of the three transducers. The speed of rotation depends on the switch frequency of the sensors. For amplitude modulation, a square chamber and the device is developed as shown in **Fig. 1.11f**, the drive consists of two orthogonal piezoelectric transducers aligned with the chamber wall.[113] The acoustic waves generated by the orthogonal electrodes are superimposed in the chamber, and the potential field and the position of the object in the chamber are changed as the amplitude of the two acoustic waves changes. If the amplitude changes continuously, the continuous rotation or controlled change of the angular position of the object in the chamber is achieved. A 180° rotation of the glass fiber with 36 rpm was accomplished by amplitude modulation. The principle is similar to that of amplitude modulation, with the difference that the mode change in the chamber is caused by the change in the phase difference of the orthogonal acoustic waves.[113] A 180° rotation of the clumps of copolymer particles was accomplished by phase modulation (**Fig.1.11g**).

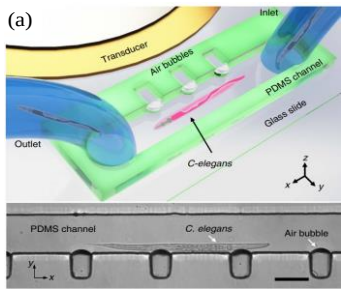
(a)
Inlet
Transducer
Air bubbles
PDMS channel
Glass slide
Outlet
C-elegans
PDMS channel
C. elegans
Air bubble

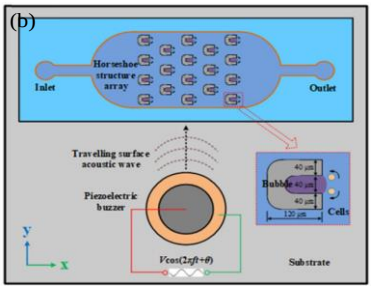
(b)
Horseshoe structure array
Inlet
Outlet
Travelling surface acoustic wave
Piezoelectric buzzer
Substrate

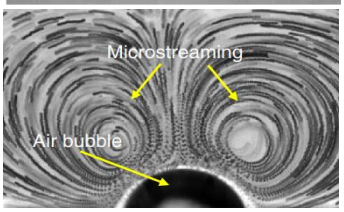
Microstreaming
Air bubble

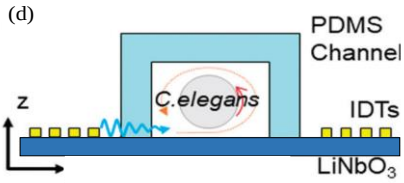
(d)
PDMS Channel
C.elegans
IDTs
z
LiNbO3

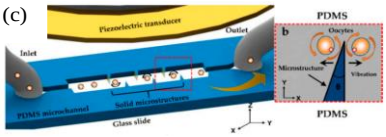
(c)
Piezoelectric transducer
Outlet
Inlet
PDMS
Oocytes
Microstructure
Vibration
PDMS microchannel
Solid microstructures
Glass slide
PDMS

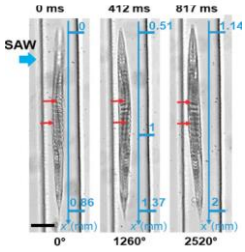
0 ms
412 ms
817 ms
SAW
0.51
1.14
1
0.86
1.37
2
0°
1260°
2520°

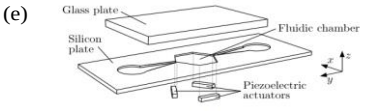
(e)
Glass plate
Fluidic chamber
Silicon plate
Piezoelectric actuators

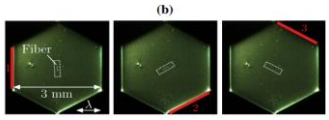
(b)
Fiber
3 mm

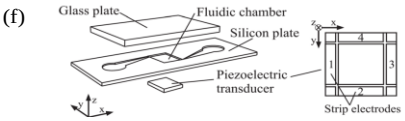
(f)
Glass plate
Fluidic chamber
Silicon plate
Piezoelectric transducer
Strip electrodes

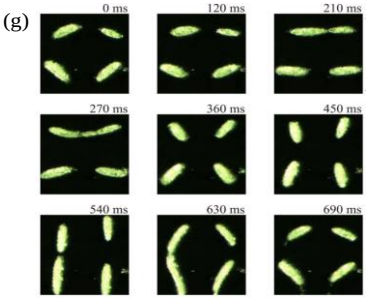
(g)
0 ms
120 ms
210 ms
270 ms
360 ms
450 ms
540 ms
630 ms
690 ms

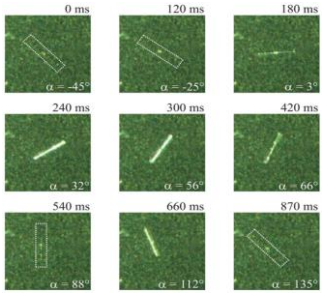
0 ms
120 ms
180 ms
α = -45°
α = -25°
α = 3°
240 ms
300 ms
420 ms
α = 32°
α = 56°
α = 66°
540 ms
660 ms
870 ms
α = 88°
α = 112°
α = 135°

Fig. 1.11 (a) A schematic of the acoustofluidic rotational manipulation device and an optical image of acoustic microstreaming as microbubble oscillation. [109] (b) Bubble array based acoustofluidic device for simultaneous rotation of massive cells using ultrasonic excitation. [110] (c) Design of the rotational device with microstructures. [111] (d) Images showing the rotation of C. elegans in a continuous flow, where the SAW comes from the left IDT. [112] (e) Exploded view of hexagonal chamber which is etched into silicon and three distinct piezoelectric transducers and the image of a fiber rotation. [113] (f) Exploded view of square which is etched into silicon and 2 strip electrodes and the image of a fiber rotation. [113] (g) The image of the clumps of copolymer particles rotation. [113]

1.3 Motivation

The one-dimensional (1D) standing wave model is the most used theoretical model to guide the design of microparticle manipulation devices in acoustic fluids, especially SSAW-based acoustic fluids. As shown in **Fig.1.12**, it assumes that the acoustic field formed in the microchannel is driven by SSAW, where PNs and ANs are alternately distributed with a separation distance of one-quarter wavelength of SAW. The particles can be pushed onto the PNs and captured by the acoustic radiation force. In this way, many functions can be performed, such as particle or cell separation, sorting, enrichment, patterning, etc. The surface acoustic wave driving system is based on surface acoustic waves propagating on a piezoelectric substrate with some of their energy leaking into the fluid field as longitudinal waves. These leaked waves drive the acoustic field in the fluid to manipulate the particles. To better understand the mechanism of particle motion in the acoustic fluid channel and to manipulate the particles more accurately, it is necessary to develop a two-dimensional (2D) SSAW microfluidic model to systematically analyze the acoustic field generated by vibrations on the piezoelectric substrate and the flow field affected by the leakage waves in the microfluidic platform. It is the one of the motivations of this thesis to combine the results of numerical calculations and practical experiments to form a trustworthy theoretical model.

Additionally, an acoustic tweezer based on an enhanced tilted angle (ETA) configuration was developed and applied for mechanophenotyping of live cells. To utilise the ETA device to simplify the measurement effort, I also developed a dedicated algorithm to derive the acousto-

mechanical properties of cells by recording the value of the minimum input poIr for driving the cells to the PN. The algorithm greatly reduces the complexity of data processing and the reliance on high-speed image capture device, facilitating the development of real-time mechanical phenotyping of live cells. The acoustic contrast factors of polystyrene (PS) microspheres, with diameters of 5 μm and 15 μm Ire measured and compared with the nominated values to verify the accuracy of the measurement. Two cancer cell types, A549, MDA-MB-231, and leukocytes Ire thereafter characterised using the ETA device for measuring their acoustic contrast factors and compressibility. The results demonstrated the successful cell mechanophenotyping, highlighting the versatility of the ETA applications in mechanical phenotyping of cells.

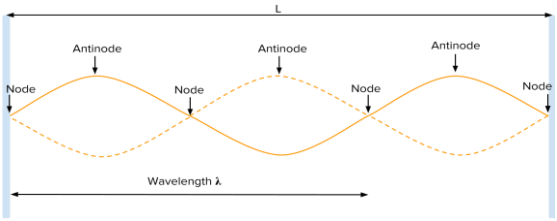

Fig. 1.12 Pressure nodes and pressure antinodes of standing wave

Chapter 2 Theory and mechanism

The study of acoustofluidics is essentially a study of particle motion in acoustics driven microfluidic devices and the laws of fluid motion. In an acoustic field, the fluid medium flows because of the acoustic field, and this flow is called acoustic streaming. The particle motion in the fluid medium is the result of a combination of factors, the two most obvious being the acoustic radiation force due to the presence of the acoustic field, and the fluid drag force due to the difference in speed between the particle motion and the medium motion, which is mainly due to viscous forces. Because of the small mass of the particle, the gravitational force on the particle is negligible in this microscopic environment, so that the particle is moving under the combined effect of radiation force and drag force, the two forces. These two forces have their own tendencies to change depending on the nature of the particle and the nature of the medium, thus influencing the state of motion and the way the particle is arranged.

2.1 Acoustofluidics theory

When the acoustic wave enters the fluid, the acoustic wave is affected by the fluid, the acoustic wave equation in the fluid is needed to be determined firstly, and this derivation comes from the Navier–Stokes equations equation, as follows

$$p = p(\rho) \tag{1}$$

$$\partial_t \rho = -\nabla \cdot (\rho v) \tag{2}$$

$$\rho \partial_t v = -\nabla p - \rho(v \cdot \nabla)v + \eta_0 \nabla^2 v + \beta \eta_0 \nabla(\nabla \cdot v) \tag{3}$$

Where p is the pressure, ρ is the density, v is the flow rate, η_0 is the fluid viscosity, and β is the viscosity ratio. As both p and ρ change during fluid vibration, a multi-order expansion of these physical quantities is generally adopted in research, where the subscripts of the variables indicate the order of the expansion.

$$p = p_0 + p_1 + p_2 + \cdots \tag{4}$$

$$\rho = \rho_0 + \rho_1 + \rho_2 + \cdots \tag{5}$$

$$v = v_0 + v_1 + v_2 + \cdots \tag{6}$$

2.1.1 First order perturbation equations

In the traditional acoustic theory, acoustic waves are generally considered small-amplitude medium perturbations. Simplifying Eqs. (6-8) to obtain the first-order acoustic wave equations,

$$\rho = \rho_0 + \rho_1, \tag{7}$$

$$p = p_0 + c_0^2 \rho_1, \tag{8}$$

$$v = v_0 + v_1 \tag{9}$$

where c_0 is the proportionality constant that is approximately equal to the speed of sound in the fluid, ρ_0, p_0, v_0 is the medium's density, pressure, and velocity, and ρ_1, p_1, v_1 are the amount of disturbance induced by the acoustic wave. As the medium is at rest, $v_0 = 0$. Substituting Eq. (9) into Eqs. (4) and (5) yields the continuity and momentum equations for the first- order terms:

$$\frac{1}{c_0^2}\frac{\partial p_1}{\partial t} = -\rho_0 \nabla \cdot v_1 \tag{10}$$

$$\rho_0 \frac{\partial v_1}{\partial t} = -\nabla p_1 + \eta \nabla^2 v_1 + \beta \eta \nabla(\nabla \cdot v_1) \tag{11}$$

I assumed the first-order density, pressure, and velocity to be harmonic time dependence, i.e.

$$\rho_1(r,t) = Re\left[\rho_1 \mathrm{e}^{\mathrm{i}\omega t}\right] \tag{12}$$

$$p_1(r,t) = Re\left[p_1 e^{\mathrm{i}\omega t}\right] \tag{13}$$

$$v_1(r,t) = Re\left[v_1 e^{\mathrm{i}\omega t}\right] \tag{14}$$

where ω is the angular frequency, ρ_1, p_1, and v_1 are time dependent but may vary with the spatial location and ω. It is equal to the wave frequency f multiplied by 2π. From Eq. (9), it can be shown mathematically that $p_1 = c_0^2 \rho_1$. Substituting the complex mass density, pressure, and velocity in Eqs. (13) and (14) into Eqs. (10) and (11) yields the governing equations for solving p_1 and v_1,

$$\frac{\mathrm{i}\omega p_1}{c_0^2} = -\rho_0 \nabla \cdot v_1 \tag{15}$$

$$\mathrm{i}\omega \rho_0 v_1 = -\nabla p_1 + \eta \nabla^2 v_1 + \beta \eta \nabla(\nabla \cdot v_1) \tag{16}$$

The above equations are sufficient for solving the case of acoustic wave propagation in a medium and are adequate in the conventional acoustics. However, for the acoustic radiation force, the acoustic field under the first-order acoustic approximation has a zero average value over a period, so that the acoustic field has a zero average value over a considerable time scale and no acoustic radiation forces generated. Therefore, the derivation of the formula for the acoustic radiation force requires consideration of the second-order term of the acoustic field.

2.2.2 Second order perturbation equations

As can be seen from the theory in section 2.2.1, for acoustic vibrations with sinusoidal excitation, the acoustic pressure, velocity, and density perturbations in the medium are averaged over one vibration period to zero so that the acoustic radiation force on the particles in the medium is also zero when averaged over time. This is caused by the fact that I have neglected the vibrational terms above the second order in deriving the acoustic wave equation. Here, by keeping the second-order terms of Eqs.(6-8), i.e., by considering the second-order effect in the medium, I can obtain second-order perturbation equations,

$$p = p_0 + p_1 + p_2 \tag{17}$$

$$\rho = \rho_0 + \rho_1 + \rho_2 \tag{18}$$

$$v = v_1 + v_2 \tag{19}$$

Substituting Eqs. (17-19) into Eqs. (4) and (5) and collecting all second-order terms yields the equations for the second- order terms:

$$p_2 = C_0^2 \rho_2 + \frac{1}{2}\left(\frac{\partial c_0^2}{\partial \rho}\right)_0 \rho_1^2 \tag{20}$$

$$\frac{\partial p_2}{\partial t} = -\rho_0 \nabla \cdot v_2 - \nabla \cdot (\rho_1 v_1) \tag{21}$$

$$\rho_0 \frac{\partial v_2}{\partial t} = -\nabla p_2 + \eta \nabla^2 v_2 + \beta \eta \nabla(\nabla \cdot v_2) - \rho_1 \frac{\partial v_1}{\partial t} - \rho_0 (v_1 \cdot \nabla) v_1 \tag{22}$$

In general, the second-order terms are negligible relative to the first-order terms. However, suppose the time averaging results for the higher-order terms are not zero. In that case, the

second-order terms need to be considered. Their time averaging is calculated for a period, representing the time averaging effect of the acoustic wave on the particles. Defining the average $\langle X \rangle$ of the physical quantity X over time τ as

$$\langle X \rangle = \frac{1}{\tau} \int_0^{\tau} X(t)\, \mathrm{d}t \tag{23}$$

Averaging Eqs. (21) and (22) over a period yields，

$$\rho_0 \nabla \cdot \langle v_2 \rangle = -\nabla \cdot \langle \rho_1 v_1 \rangle \tag{24}$$

$$-\nabla \langle p_2 \rangle + \eta \nabla^2 \langle v_2 \rangle + \beta \eta \nabla (\nabla \cdot \langle v_2 \rangle) = \langle \rho_1 \frac{\partial v_1}{\partial t} \rangle + \rho_0 \langle (v_1 \cdot \nabla) v_1 \rangle \tag{25}$$

Substituting the complex mass density, pressure, and velocity in Eqs. (13) and (14) into Eqs. (24) and (25) yields the governing equations for solving $\langle v_2 \rangle$ and $\langle p_2 \rangle$,

$$\rho_0 \nabla \cdot \langle v_2 \rangle = -\frac{1}{2} \mathrm{Re}[\nabla \cdot (\rho_1^* v_1)] \tag{26}$$

$$\eta \nabla^2 \langle v_2 \rangle - \nabla \langle p_2 \rangle = \frac{1}{2} \mathrm{Re}(\mathrm{i}\omega \rho_1^* v_1) + \frac{\rho_0}{2} \mathrm{Re}(v_1^* \cdot \nabla v_1) + \frac{\eta \beta}{2\rho_0} \mathrm{Re}\{\nabla [\nabla \cdot (\rho_1^* v_1)]\} \tag{27}$$

where the asterisk denotes the complex conjugate of the quantity.

It is noted that the time average $\langle f, g \rangle$ for two sinusoidally varying complex numbers f, g can be obtained from

$$\langle f, g \rangle = \frac{1}{2} Re[f(r) g(r)^*] \tag{28}$$

The second order acoustic pressure and velocity are the key factors in deriving the acoustic radiation force.

2.2 Forces on a Particle

2.2.1 Acoustic Radiation force

For deriving the acoustic radiation force for a compressible, spherical particle in an inviscid fluid in an acoustic field of wavelength λ, I need to assume that the particle is sufficiently small (micrometer-sized), i.e., $a << \lambda$, and the particle density ρ and the compressibility κ

ensuring that the particle's scattering is weak point-scatter. So that first-order scattering theory can be applied. Under the weak scattering theory, the first order acoustic field is the sum of the velocity potential of the incoming wave ϕ_{in} and scattered wave ϕ_{sc}, as shown in **Fig. 2.1**.

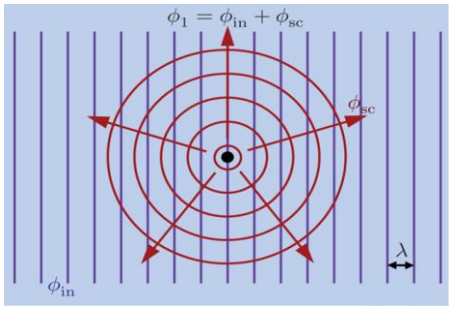

Fig.2.1 Sketch of the far-field region $\boldsymbol{r >> \lambda}$ of an incoming acoustic wave (blue lines) of wavelength $\boldsymbol{\lambda}$ scattering off a small particle (black dot) with radius $\boldsymbol{a << \lambda}$, leading to the outgoing scattered wave $\boldsymbol{\phi_{sc}}$ (red circles and arrows).

The resulting first-order wave is $\phi_1 = \phi_{\mathrm{in}} + \phi_{\mathrm{sc}}$.

$$\phi_1 = \phi_{\mathrm{in}} + \phi_{\mathrm{sc}} \tag{29}$$

$$v_1 = \nabla\phi_1 = \nabla\phi_{\mathrm{in}} + \nabla\phi_{\mathrm{sc}} \tag{30}$$

$$p_1 = \mathrm{i}\rho_0\omega\phi_1 = \mathrm{i}\rho_0\omega\phi_{\mathrm{in}} + \mathrm{i}\rho_0\omega\phi_{\mathrm{sc}} \tag{31}$$

Once the first-order scattered field ϕ_{sc} has been determined by a given incoming field ϕ_{in}, the acoustic radiation force F_r can be obtained by integrating the time-averaged second-order pressure p_2 and momentum flux tensor $\rho_0\langle v_1 v_1\rangle$ over a fixed surface, $\partial\Omega$, in the bulk fluid around the particle[114],

$$F_r = -\oiint_{\partial\Omega} \langle n \cdot [p_2 I + \rho_0(v_1 v_1)]\rangle \mathrm{d}A \tag{32}$$

where n is the unit normal vector of the particle surface directed into the fluid, I is the unit tensor. An analytical expression of the force has been derived by Settnes and Bruus,[115]

$$F_r = -\frac{4}{3}\pi a^3 \nabla\left[\frac{1}{2}\mathrm{Re}[f_1]\kappa_0\langle p_{in}^2\rangle - \frac{3}{4}\mathrm{Re}[f_2]\rho_0\langle v_{\mathrm{in}}^2\rangle\right] \tag{33}$$

where f_1 and f_2 are the scattering coefficients, and κ_0 is the isentropic compressibility of the fluid defined as,

$$\kappa_0 = -\frac{1}{V}\left(\frac{\partial V}{\partial \hat{p}}\right)_S = \frac{1}{\hat{\rho}}\left(\frac{\partial \hat{\rho}}{\partial \hat{p}}\right)_S, \tag{34}$$

V and S are the volume and entropy of the fluid. By neglecting the second and the higher order terms, it can be shown that $\kappa_0 = 1/(\rho_0 c_0^2)$.[116] The scattering coefficients can be calculated by

$$f_1 = 1 - \frac{\kappa_\mathrm{p}}{\kappa_0} \tag{35}$$

$$f_2 = \frac{2(1-\gamma)(\rho_\mathrm{p} - \rho_0)}{2\rho_\mathrm{p} + \rho_0(1-3\gamma)} \tag{36}$$

where

$$\gamma = -\frac{3}{2}\left[1 + \mathrm{i}\left(1 + \frac{\delta}{a}\right)\right]\frac{\delta}{a} \tag{37}$$

$$\delta = \sqrt{\frac{2\eta}{\omega\rho_0}} \tag{38}$$

ρ_p and κ_p are the mass density and the compressibility of the particle, respectively. δ is called the viscous penetration depth or the characteristic thickness of the viscous boundary layer.[117] Considering that most cases of acoustic radiation force are from a one-dimensional planar standing wave sound field, where

$$\phi_{in}(z,t) = \frac{p_a}{\rho_0\omega}\cos(kz)\cos(\omega t) \tag{39}$$

$$p_{in}(z,t) = p_a\cos(kz)\sin(\omega t), \tag{40}$$

$$\rho_{in}(z,t) = \frac{p_a}{c_0^2}\cos(kz)\sin(\omega t), \tag{41}$$

$$v_{in}(z,t) = -\frac{p_a}{\rho_0 c_0}\sin(kz)\cos(\omega t)e_z, \tag{42}$$

With these fields, the time averages needed in eqn (33) are simply by

$$\langle\cos^2(\omega t)\rangle = \langle\sin^2(\omega t)\rangle = \frac{1}{2}, \tag{43}$$

The resulting radiation force on a small, spherical particle is finally found,

$$F_\mathrm{r} = -\left(\frac{\pi P_0^2 \mathrm{V_P}\beta_\mathrm{m}}{2\lambda}\right)\varphi\sin(2kx) \tag{44}$$

$$P_0 = \sqrt{\frac{\alpha P_{\mathrm{I}} \rho_{\mathrm{s}} C_{\mathrm{s}}}{A_{\mathrm{w}}}}, \tag{45}$$

$$\varphi = \frac{5\rho_{\mathrm{p}} - 2\rho_{\mathrm{m}}}{2\rho_{\mathrm{P}} + \rho_{\mathrm{m}}} - \frac{\beta_{\mathrm{P}}}{\beta_{\mathrm{m}}}, \tag{46}$$

where P_0, λ, V_{P}, β_m, β_{p}, φ, k, x, μ, R_{P}, α, P_{I}, ρ_{s}, ρ_{p}, ρ_{m}, C_{s} and A_{w} are acoustic pressure amplitude, SAW wavelength, cell volume, compressibility of medium, cell compressibility, acoustic contrast factor, acoustic wavenumber, distance from a pressure node, viscosity of the medium, cell radius, power conversion efficiency, RF input power, the density of the substrate, cell density, the density of the medium, surface wave phase velocity, and acoustic working area, respectively.

2.3 Force analysis in microfluidics

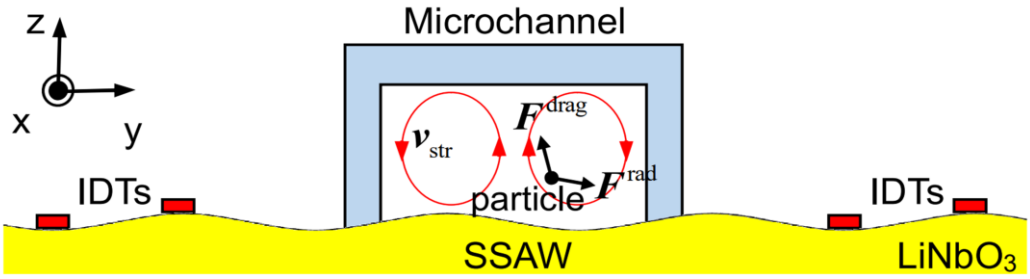

Fig. 2.2 The force exerted on the microparticle inside the acoustic microchannel is the combination of the acoustic radiation force and Stokes drag force.

Acoustofluidic manipulation is the study of particle motion in acoustically driven microfluidic devices and the laws of fluid motion. As shown in **Fig. 2.2**. In an acoustic field, a fluid medium will flow because of the acoustic wave, which is called acoustic streaming. The particle movement in the fluid medium results from two main forces, acoustic radiation force, and

streaming drag force. Acoustic radiation force results from the interaction of the acoustic wave with particles. Streaming drag force is due to the difference in speed between particle and medium movement. With the gravitational and buoyant forces on the particles canceling each other out, the acoustic radiation and streaming drag forces determine the motion of the particles. The equation of motion of a particle according to Newton's laws of motion is

$$ma = F_r + F_d \tag{47}$$

where m is the particle mass and a is the particle acceleration, and the streaming drag force of a spherical particle in a fluid following the equation, which is

$$F_{\mathrm{d}} = -6\pi\mu R_{\mathrm{P}}(u - u_{\mathrm{f}}), \tag{48}$$

where π is the circumference, μ is the viscosity of the medium, u is the relative velocity of the particle to the medium velocity. [118] The acoustic radiation force is closely related to the distribution of the acoustic field. The streaming drag force on the particle is closely associated with the relative velocity of the particle and the fluid. In this chapter, governing equations of fluid flow and acoustic radiation force are discussed in turn.

2.4 Surface acoustic wave

A surface acoustic wave, also called Rayleigh acoustic surface wave, is an acoustic wave that propagates along the surface of an elastic material, with most of the acoustic energy trapped near the surface. The study of SAWs dates back to 1885, when Lord Rayleigh reported the propagation mode and some properties of SAWs.[119] The generation of SAWs relies on the inverse piezoelectric effect, which describes that material expansion and compression occur in piezoelectric materials when a charge with potential is applied (see **Fig.2.3**). The transducers to generate SAW devices usually consist of a piezoelectric material as a substrate on which metallic interdigital transducers (IDTs) are deposited as electrodes (see **Fig.2.4**). When an IDT is fed with an alternative signal, an alternative electric field is generated within the piezoelectric material. This electric field induces mechanical stresses in the elastic piezoelectric material and therefore generates vibrations that propagate at the interface

between the IDT and the piezoelectric material, i.e., the surface of the piezoelectric material. one of the most important design considerations for SAW devices is the IDT design. The simplest IDT mode is a straight rectangular finger electrode connected by a pair of bus bars. The width of the SAW is determined by the overlap length of the interfinger electrodes (see **Fig.2.5**).

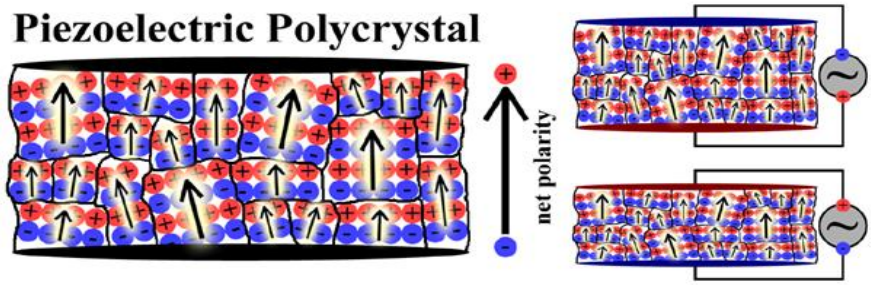

Fig. 2.3 Demonstration of a polycrystalline piezoelectric material at rest (left) and under antagonistic applied voltages (right).

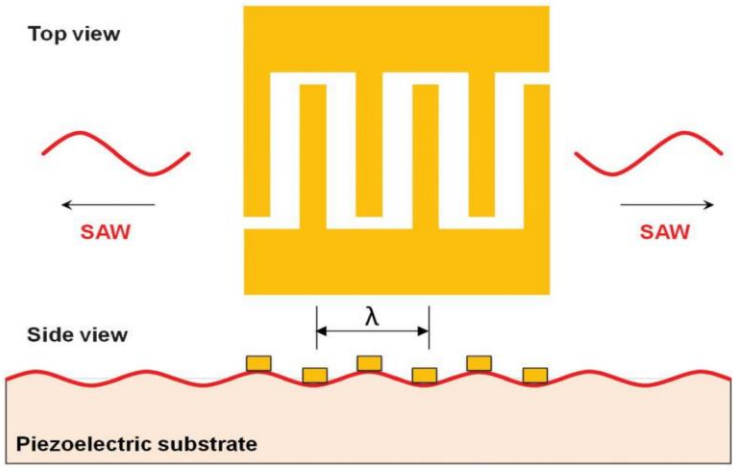

Fig. 2.4 SAW generation illustration

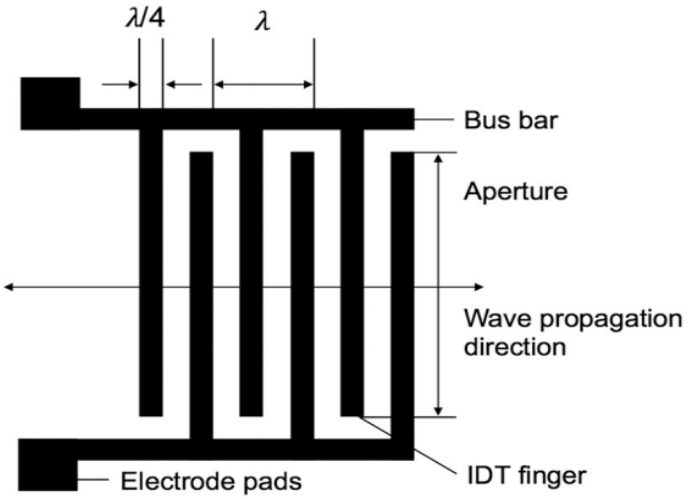

Fig. 2.5 A typical design of IDT

Chapter 3 Experimental setup

3.1 GaN-based microfluidic system

In order to investigate the particle operation using GaNAT and to compare the results with simulations, I needed to first measure the reflection function of the two IDTs in terms of S11 (reflection coefficient) using a vector network analyser (VNA, E5061B ENA Series, Keysight, USA). The measurement results were used to design an impedance matching network for the IDTs to maximise power transfer to approach the theoretical results, while reducing the risk of damaging the power amplifier when operating at high power. The experimental setup is shown in **Fig.3.1**. Radio frequency (RF) signals were amplified by a power amplifier (100A250A, Amplifier Research) to drive a GaNAT. power meter (U2004A, Keysight Technologies, UK) to monitor the incident and reflected power of each IDT in real time.

After adding the matching circuit, I prepared two batches of mixed polystyrene microsphere samples, e.g. 15 μm and 5 μm, and 15 μm and 1 μm, and injected them into the microchannels separately using a syringe pump. When the samples were uniformly dispersed within the microchannels, an RF signal was applied to the GaNAT. The input power of the GaNAT used to drive the particles was set to 40 dBm (10 W)

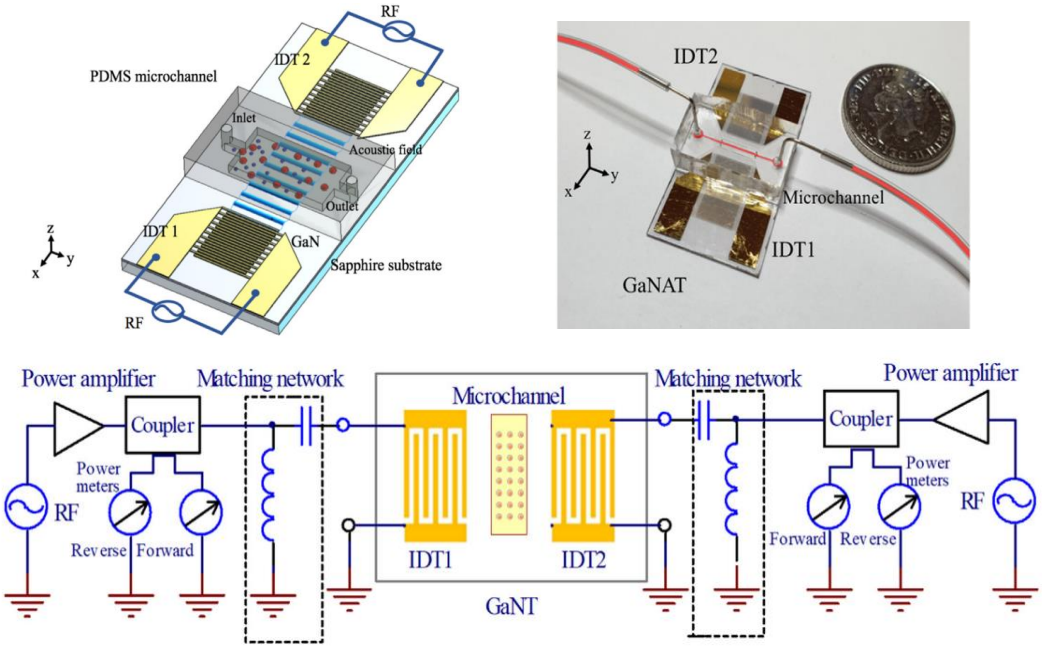

Fig. **3**.1 The experimental setup of the GaN-based microfluidic system

3.2 Cells Mechanophenotyping

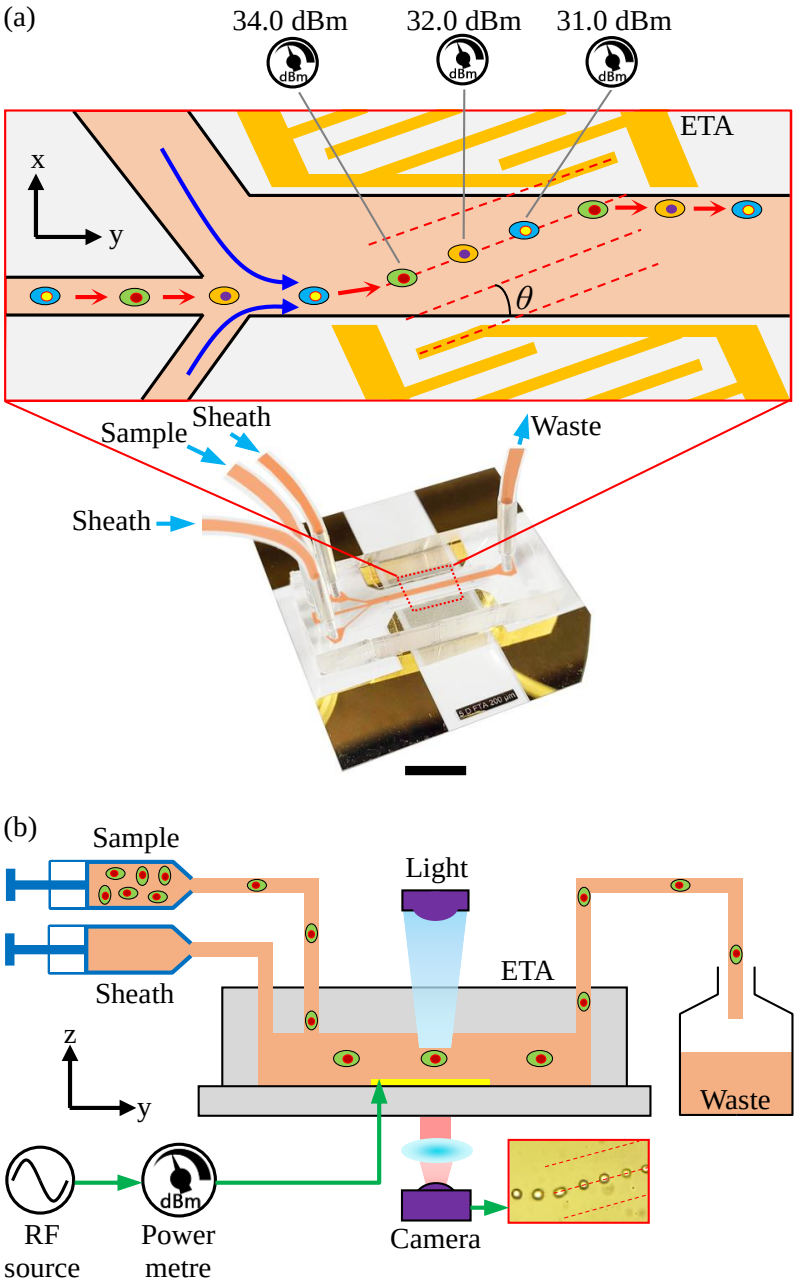

Fig. 3.2 An enhanced titled angle (ETA) acoustofluidic device for mechanical phenotyping of cells. (a) Working mechanism of the ETA-based cell mechanophenotyping. The input power for effectively trapping cell to the PN is associated with the cell's mechanical properties. Cells are convergent to the first nearest PN driven by the acoustic radiation force ($\boldsymbol{F}_r$). The scale bar is 1 cm. (b) The diagram of the system setup. The power metre is used for registering the minimum input power for trapping the cells to the first nearest PN.

Fig. 3.2a show a photo of the ETA device used in the present work. The device is consisted of

a PDMS channel and ETA IDTs patterned on a 128° Y-cut X-propagation $LiNbO_3$ piezoelectric substrate. The IDTs were deposited onto the $LiNbO_3$ substrate using a photolithography technique followed by a lift-off process. The IDTs were patterned with 52 pairs of finger electrodes, which have identical finger width and spacing of 50 μm resulting in a high quality factor of the IDT (Q≈26). The aperture size is 10 mm to accommodate the channel length. The working frequency was measured by using a vector network analyser (E5061B ENA, Keysight). The measured value of ~19.632 MHz is close to the theoretical value of 19.985 MHz determined by $f=c/\lambda$, where c is the speed of sound in $LiNbO_3$ (3,997 ms^{-1}), λ is the SAW wavelength (200 μm). The minor difference between the measured and theoretical values could be caused by the capacitance/inductance introduced by the busbars connected with the IDTs. I used ethanol as a temporary lubricant during the alignment between fingers and channel.

The PDMS channel had a central inlet for sample flow, and two sheath flow inlets to hydrodynamically focus the cells before entering the acoustic field. The channel was fabricated using standard photolithography and PDMS casting techniques. The length, width, and height of the channel in the acoustic region were 1 cm, 800 μm, and 60 μm, respectively. The PDMS channel and the $LiNbO_3$ substrate were aligned under an inverted microscope and bonded after treated with oxygen plasma (HPT-100, Henniker Plasma). The device was sat on the inverted microscope with a camera to record the trajectory of the cells / microparticles (Fig. 1b). Three inlets were connected to three plastic syringes which were driven by three syringe pumps (WZ-74905, Cole-Parmer) separately. The ETA IDT was electrically connected to a signal generator (N5166B CXG, Keysight Technologies) through a power amplifier (100A250A, Amplifier Research) and a coupler (86207A, Keysight Technologies). The forward and reflected powers were measured using two power meters (U2004A, Keysight Technologies). Before the introduction of microparticles or cells, ethanol was used to flush the PDMS channel to remove air bubbles. Then, 2.5% bovine serum albumin (BSA) was used to coat the channel walls to avoid bioparticles attachment. The flow rates of the two sheaths were 5 μl/min and 4 μl/min, respectively, while the sample flow rate was 0.2 μl/min.

Before measuring cancer cells and leukocytes, PS microspheres were used to establish the

reference trajectory and validate the accuracy of measuring the acoustic contrast factor. Firstly, 10 μm PS (72986, Sigma-Aldrich) microspheres were chosen to generate the reference trajectory by tuning the input power from 20 dBm to 30 dBm. Then, the acoustic contrast factors of 5 μm (79633, Sigma-Aldrich) and 15 μm PS microsphere (74964, Sigma-Aldrich) were obtained individually to benchmark with the nominated value.

3.3 Cell preparation

In GaN-system experiments, I used commercially mouse renal tumour cells (TSC1-associated tumour cells, Tsc1-204)259 and mouse embryonic fibroblast cells (Tsc1-387-2)260. These two types of cells are widely used to investigate mechanisms of tuberous sclerosis-associated renal tumorigenesis and oncogenic pathway. They are quite different in their sizes, morphologies, and genotypes, and thus are easily recognized in the subsequent analysis. The sizes and viabilities of the cells were measured by a cell counter (NC-3000, Chemometec, Denmark). Mouse renal tumour cells and fibroblast cells were cultured using DMEM containing 10% fetal bovine serum, 50 units/ml penicillin, and 50 μg/ml streptomycin at 37 °C in a humidified incubator with 5% (vol/vol) CO_2 atmosphere. Before introducing to the device, the adherent cells were rendered into suspension by exposure to trypsin, followed by dilution into PBS at a concentration of 1 × 106 cells/ml. Cell samples were stored in Eppendorf tubes within an ice bath to keep the temperature at 4 °C during the experiment. To assess cell viability, acridine orange (30 μg/ml) and diaminophenylindole (100 μg/ml) were used to stain the sample at a ratio of 1:20. The stained sample was pipetted onto a counter slide and analyzed by the cell counter.

In mechanophenotyping study, I used commercially sourced A549 (CCL-185, ATCC) and MDA-MB-231 (HTB-26, ATCC) cells. Leukocytes were collected from whole blood donated by healthy volunteers using EDTA tubes (367835, BD). This study had been granted Huazhong Agricultural University's ethics committee approval prior to commencing the blood sampling. The whole blood was firstly incubated with lysis buffer for 12 mins to remove the erythrocytes. Next, leukocytes were collected by centrifuging the blood solution at 1,300 rpm for 5 minutes

at room temperature. Two fluorescent dyes Hoechst 33342 (62249, Thermo Fisher Scientific) and propidium iodide (P1304MP, Thermo Fisher Scientific) were used for staining the cells. This fluorescent labelling approach was simply to allow tracking of cell trajectories in the device, by florescent microscopy. After staining, the leukocyte, A549, and MDA-MB-231 pellets were resuspended individually in a liquid mixture of 1 × PBS and glycerol (glycerol and 1 × PBS were mixed with a volume ratio of 1:4 and the final concentrations of three types of cells were close to 2 × 105 cells/mL). Cell samples were photographed under a microscope, and the 2D cell area was measured using ImageJ software. Since the particles in the numerical simulation were assumed to be spherical, the cells were likewise treated as microspheres for calculation.

Chapter 4 Model designs and Numerical setup

4.1 Motivation

To accurately operate and better understand the device characteristics and operating mechanisms during the design phase, a theoretical model was developed to effectively predict the acoustic pressure distribution and particle motion within the system. This theoretical model was first used to analyze the sound pressure and velocity distributions in a conventional PDMS-SAW structure and compared with published simulation results to initially verify the accuracy of the model. Subsequently, I propose to add active vibration source on the top of the microchannel to enhance the acoustic power for the manipulation of particles in the microchannel. To investigate the effectiveness of the new source, I use the model to numerically simulate the particle manipulation and compared the results from acoustofluidic devices with four different hybrid structures, resulting in providing new insights into the design and fabrication of acoustic fluid sensors to improve the efficiency and accuracy of nano- and microparticle manipulation. I also use the model to analyze the acoustic pressure distribution and particle trajectories of GaN-system and compare it with experimental results. This comparison not only justify the manipulation of particles by GaN systems but also demonstrate that the accuracy of the numerical model is not affected by differences in the piezoelectric substrate. After both simulation and experimental validation, the model was used to analyze cell mechanophenotyping system.

4.2 Model design

4.2.1 Boundary conditions

To solve Eqs (15) and (16) to determine p_1 and v_1, a COMSOL software simulation are performed by using the finite element method. I started with a simulation of the conventional acoustofluidic devices, shown in **Fig. 4.1**. Operating under the same radio frequency (RF) signal, two SAWs generated by the IDTs counter-propagate on the substrate to produce a standing SAW (SSAW) within the microchannel. Stable acoustic pressure gradients are formed

in the water flowing in the microchannel which exerts acoustic radiation force and streaming drag force on the particles inside the channel.

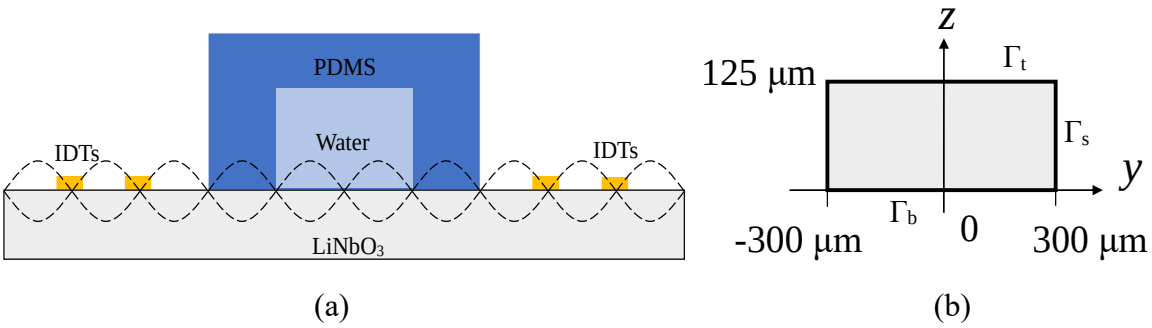

Fig. 4.1 (a) A conventional acoustofluidic device consisting of a PDMS microchannel and a SAW transducer (SAW-PDMS). (b) The computational domain of the model, the boundary $\boldsymbol{\Gamma_t}$, $\boldsymbol{\Gamma_b}$, and $\boldsymbol{\Gamma_s}$ are modelled as the top, bottom and side walls, respectively.

I employ the impedance or lossy-wall boundary condition at the water-PDMS and water-glass interfaces where the energy of the acoustic wave is partially absorbed by the solid walls. After neglecting the higher order terms, the boundary condition at these interfaces is given by

$$n \cdot \left[-p_1 I + \eta(\nabla v_1 + (\nabla v_1)^T) - \left(\frac{2}{3}\eta - \eta_b\right)(\nabla \cdot v_1) I\right] = -Z_0 (n \cdot v_1) n \tag{49}$$

where $Z_0$is the acoustic impedance of the wall. Its values for different wall materials are shown in Table 1. To derive the boundary condition at the water-LiNbO3 interface, I considered the LiNbO3 substrate to be actuated by the SSAW, and ignored the wave decay along the propagation path in the substrate because of the short path length. Specifically, I assumed the displacement of the substrate in the normal direction of a wall to be,[120]

$$u = Re\left(u_0 \mathrm{i}\left(e^{\mathrm{i}[\omega t - k_s(W/2+y)]} - e^{\mathrm{i}[\omega t - k_s(W/2+y)]}\right)\right) n \tag{50}$$

Neglecting the higher order terms, the continuity of the velocity at the water-LiNbO3 interface requires,

$$v_1 = -\omega u_0 \left[e^{-\mathrm{i}k_s(W/2+y)} - e^{-\mathrm{i}k_s(W/2-y)}\right] n \tag{51}$$

To solve Eqs. (26) and (27) for determining the second order pressure and velocity fields, I

assumed the boundary conditions to be $\langle v_2 \rangle$ =0 on the channel wall in this and all configurations appearing below. The boundary condition for $\langle p_2 \rangle$ was not specified. Instead, I required the average of $\langle p_2 \rangle$ over the cross-sectional area of the microchannel to be zero.

4.2.2 Mesh

Computational mesh with the maximum element dimension d_{b} at the domain boundary and $10d_b$ in the bulk fluid domain is reasonable to capture the physics of the model. I use an illustrative mesh with d_b= 30 δ, where δ is the viscous penetration depth defined in Eq. 38. For verifying the convergence of the numerical solutions, I defined a relative convergence function $C(\mathrm{g})$,

$$C(\mathrm{g}) = \sqrt{\frac{\int (\mathrm{g}-\mathrm{g}_{\mathrm{ref}})^2 \mathrm{d}y\mathrm{d}z}{\int (\mathrm{g}_{\mathrm{ref}})^2 \mathrm{d}y\mathrm{d}z}} \tag{52}$$

where g is the solution of p_1, v_1 and $\langle v_2 \rangle$ with a given d_{b}, and $\mathrm{g}_{\mathrm{ref}}$ is the reference solution with the smallest d_{b} that was chosen to be 0.2δ in the study. At this dimension, the number of elements was 5.6×10^5 in the simulation domain. I observed that the value of C(g) was less than 0.002 when d_{b} was less than 0.3 δ. Therefore, all simulations were performed at this mesh size.

To simulate the fluid flow and particle distribution patterns, I first solved Eqs. (15) and (16) to determine p_1 and v_1. The results were substituted into Eqs. (26) and (27) to solve for $\langle v_2 \rangle$ and $\langle p_2 \rangle$. Finally, the particle velocity and trajectories were determined by solving Eq. (40).

4.2.3 Model instruction

4.2.3.1 Model Wizard

1.In the Model Wizard window, click 2D.

2.In the Select Physics tree, select Acoustics>Thermovicous Acoustics> Thermoviscous Acoustics, Frequency Domain

3.Click Add.

4.In the Select Physics tree, select Fluid Flow>Single-Phase Flow>Laminar Flow

5.Click Add.

6.In the Select Physics tree, select Fluid Flow>Particle Tracing > Particle Tracing for Fluid Flow.

7.Click Study.

4.2.3.2 Geometry

1.In the Geometry toolbar, click Rectangle.

2.In the Settings window for Rectangle, locate the Size and Shape section.

3.In the Width text field, type W.

4.In the Height text field, type H.

5.Click Build Selected.

4.2.3.3 Set parameters

Fill in the blanks according to the datasheet below,

Name	Expression	Value	Description
f0	6.65[MHz]	6.65E6 Hz	Study frequency
omega0	2*pi*f0	4.1783E7 Hz	Study angular frequency
dvisc0	50[um]*sqrt(100[Hz]/f0)	1.9389E-7 m	Mesh viscous penetration depth at f0
lambda0	c_f/f0	2.2511E-4 m	Wavelength
k0	2*pi/lambda0	27911 1/m	Wave number
W	600[um]	6E-4 m	Channel cross section width
H	125[um]	1.25E-4 m	Channel cross section height
A	5[um]	5E-6 m	Particle radius
rho_p	1.05e3[kg/m^3]	1050 kg/m³	Particle denisty
beta0_p	2.38e-10[1/Pa]	2.38E-10 1/Pa	Particle isentropic compressibility
alpha0_p	2.1e-4[1/K]	2.1E-4 1/K	Particle thermal expansion
Cp_p	1.22e3[J/(kg*K)]	1220 J/(kg·K)	Particle specific heat capacity at constant pressure

gamma_p	1.04	1.04	Particle ratio of specific heats
kcond_p	1.54e-1[W/(m*K)]	0.154 W/(m·K)	Particle thermal conductivity
c_p	2.4e3[m/s]	2400 m/s	Particle longitudinal (compressional) wave speed
cT_p	1.15e3[m/s]	1150 m/s	Particle transvers (shear) wave speed
c_f	1497[m/s]	1497 m/s	Fluid speed of sound
rho_f	997[kg/m^3]	997 kg/m³	Fluid density
beta0_f	4.48e-10[1/Pa]	4.48E-10 1/Pa	Fluid isentropic compressibility
alpha0_f	2.75e-4[1/K]	2.75E-4 1/K	Fluid thermal expansion
Cp_f	4.18e3[J/(kg*K)]	4180 J/(kg·K)	Fluid heat capacity at constant pressure
gamma_f	1.012	1.012	Fluid ratio of specifc heats
mu_f	8.9e-4[Pa*s]	8.9E-4 Pa·s	Fluid dynamic viscosity
muB_f	2.47e-3[Pa*s]	0.00247 Pa·s	Fluid bulk viscosity
kcond_f	6.1e-1[W/(m*K)]	0.61 W/(m·K)	Fluid thermal conduction
u0	0.1[nm]	1E-10 m	
lambda	c_p1/f0	6.006E-4 m	
K	2*pi/lambda	10461 1/m	
c_p1	3994[m/s]	3994 m/s	

4.2.3.4 Add boundary condition

As described in the section above, select the corresponding boundary and enter the velocity equation and impedance value, respectively.

4.2.3.5 Mesh

1.In the Model Builder window, under Model 1 (mod1) click Mesh 1.

2.In the Settings window for Mesh, locate the Mesh Settings section.

3.From the Sequence type list, choose User-controlled mesh size.

5. In the Model Builder window, under Model 1 (mod1) >Mesh 1 click Size.

6. In the Settings window for Size, locate the Element Size section.

7. Click the Custom button.

8. Locate the Element Size Parameters section. In the Maximum element size text field, type 60 um.

in the Minimum element size text field, type 1.2 um.

9. in the Maximum element growth rate text field, type 1.4.

10. in the Curvature factor text field, type 0.4.

11. in the Resolution of narrow regions text field, type1.

4.2.3.6 Free Triangular 1

1 In the Model Builder window, click Free Triangular 1.

2 Click Build All.

4.2.3.7 Boundary Layers 1

1 In the Model Builder window, click Boundary Layers 1.

2 Click Build All.

4.2.3.8 Study 1

Step 1: Frequency Domain

1.In the Model Builder window, under Study 1 click Step 1: Frequency Domain.

2.In the Settings window for Frequency Domain, locate the Study Settings section.

3.In the Frequencies text field, type f0.

4.In the physics and Variables Selections window for Frequency Domain, select Thermoviscous Acoustics, Frequency Domain(ta).

5 In the Home toolbar, click Compute.

4.2.3.8 Study 2

Step 1: Stationary

1.In the Model Builder window, under Study 2 click Step 1: Stationary.

2.In the Settings window for Frequency Domain, locate the Study Settings section.

3.In the physics and Variables Selections window for Stationary, select Laminar Flow(spf).

4.In the Home toolbar, click Compute.

4.2.3.9 Particle Properties 1

1. In the Model Builder window, under Model 1 (mod 1)>

Particle Tracing for Fluid Flow (fpt) click Particle Properties 1.

2 In the Settings window for Particle Properties, locate the Particle Properties section.

1. In the ρp text field, type rho_p.

2. In the dp text field, type 2*a.

4.3 Novelty SAW systems

Three different model configurations are considered. Fig. 3.4(a) shows the model of a novel structure of an acoustofluidic chip[83] for high throughput CTC separation, which employs a glass slide as the acoustic reflector attached on the top of the channel, namely hybrid PDMS-glass resonator (I call it SAW-Glass). The reflector prevents the acoustic energy loss caused by the PDMS absorption on the top. To further increase the acoustic pressure in the microchannel for enhanced manipulation of nano- and micro-particles, two new acoustofluidic structures have been developed, as shown in **Fig. 4.2b** and **Fig. 4.2c**. In **Fig. 4.2b**, the top wall of the microchannel is sandwiched between two identical SAW transducers and the side walls are made of PDMS, I call this structure as SAW-SAW. The SAW-SAW model can provide stronger acoustic pressure gradients in the microchannel. By tuning the phase difference between the top and bottom SAW transducers, the acoustic pressure distribution can be controlled. The model shown in **Fig. 4.2c** is similar to that shown in **Fig. 4.2b**, except the top wall that is formed by a PZT. This structure is called PZT-SAW. The RF signals are driving both the PZT and SAW transducers to produce an integrated acoustic field in the microchannel. Changing the input parameters such as the frequency and voltage of the PZT and SAW transducers can vary the integrated acoustic field.

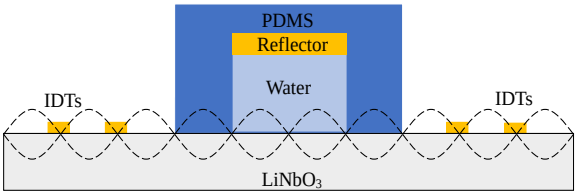

(a) hybrid SAW PDMS-glass resonator (SAW-Glass)

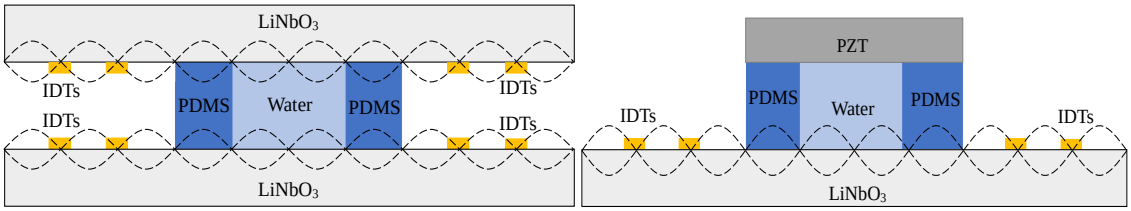

(b) Double-SAW transducer (SAW-SAW) (c) PZT-SAW transducer (PZT-SAW)

Fig. 4.2 (a) A hybrid acoustofluidic resonator employing a glass slide as the reflector positioned at the top of the PDMS microchannel (SAW-Glass). (b) A novel acoustofluidic configuration equipped by two SAW transducers as the top and bottom plates (SAW-SAW). (c) An integrated acoustofluidic configuration consisting a top PZT and a bottom SAW transducer (PZT-SAW).

For the SAW-SAW configuration, Eq.(43) is used as the velocity boundary condition on the bottom wall. For the top wall, Eq. (53) is used as the boundary condition,

$$v_1 = -\omega u_0 \left\{ e^{-\mathrm{i}[k_s(W/2+y)-\Delta\varphi]} - e^{-\mathrm{i}[k_s(W/2-y)+\Delta\varphi]} \right\} n \tag{53}$$

which is the same as Eq. (43) except a phase difference, $\Delta\boldsymbol{\varphi}$. For the water-PZT interface, I assumed that PZT vibrated only in the z direction. Thus, the displacement and the velocity of the substrate at this interface are,

$$u = Re(u_T e^{\mathrm{i}\omega t}) n \tag{54}$$

$$v = Re(\mathrm{i}\omega u_T e^{\mathrm{i}\omega t}) n \tag{55}$$

where $\boldsymbol{u_T}$ denotes the maximum amplitude of the PZT surface displacement, which is controlled by the applying RF voltage. Again, the continuity of the velocity at the water-PZT interface requires,

$$v = \mathrm{i}\omega u_T n \tag{56}$$

4.3 Numerical model of GaN system

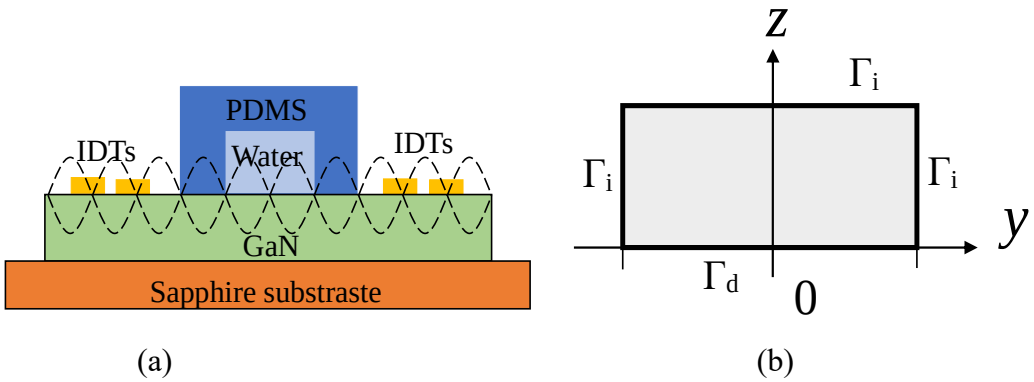

Fig. 4.3 (a) a GaN-based microfluidic system employing a GaN-sapphire substrate. (b) The computational domain of the model, the boundary Γi, and Γd are modelled as impedance condition and motion condition, respectively.

As described in Chapter 2, the PDMS walls of the channels are modelled by using impedance boundary conditions, while the effect of the piezoelectric substrate is modelled using a displacement function at the substrate boundary. Computational domain Ω is shown in **Fig. 4.3b** as a rectangular microchannel, where the boundary affected by the impedance condition is denoted by Γi, while the boundary affected by the motion is denoted by Γd. The GaN-based microfluidic system has a surface wave with a wavelength λ = 280μm, a frequency f = 19.4 MHz, a channel of 280 μm *60 μm. The boundary conditions are discussed in detail in section 2.4. Relevant parameter values used in the numerical simulations are shown in Table 3.

4.4 Numerical simulation and Algorithm for Cells Mechanophenotyping

4.4.1 Numerical simulation

A. x-z planes

Numerical simulations were performed to reveal the trajectories of particles on the x-z and x-y planes respectively. The cross-sectional acoustic pressure distribution and particle trajectory were solved using the finite element software package COMSOL Multiphysics. The model is built as described in Section 2. The module “Pressure Acoustics” was used to numerically

compute the acoustic pressure distribution in the frequency domain. The trajectories of particles were simulated using the "Particle Tracing model". The system was simplified by the two-dimensional cross-sectional modelling in a rectangular domain with a width of 800 μm and height of 60 μm. Polydimethylsiloxane (PDMS) walls of the channel were modelled applying with impedance boundary conditions, and the piezoelectric substrate was modelled applying a displacement function at the domain bottom. An attenuation coefficient is introduced to describe the different distances of the IDEs from the channel

$$v_1 = -\omega u_0 \{ e^{-c_d(W/2+y)} e^{-i[k_s(W/2+y)]} - e^{-c_d(W/2-y)} e^{-i[k_s(W/2-y)]} \} n \quad (57)$$

In the x-z plane simulation, I studied three different sizes of PS microsphere: 5 μm, 10 μm, and 15 μm. The input power applied to the IDTs varies in the range of 20 dBm to 34 dBm, with an incremental step of 0.5 dBm.

B. x-y planes

The projections of the particles' trajectories on the x-y plane were predicted by integrating Equation (4) with respect to time in MATLAB, MathWorks, with a given position when a particle initially enters the microchannel. Considering the use of the FTA device, where the IDTs direction has an angle with the channel direction, I introduce two axes for the simulation study as shown in **Fig. 4.4**, where the x-axis of the xyz axis is parallel to the fluid direction, the x-axis of the xzy axis is parallel to the IDE. The origin of the xyz and xyz axes are at the channel's center and the channel's upper wall at the fluid inlet, respectively.

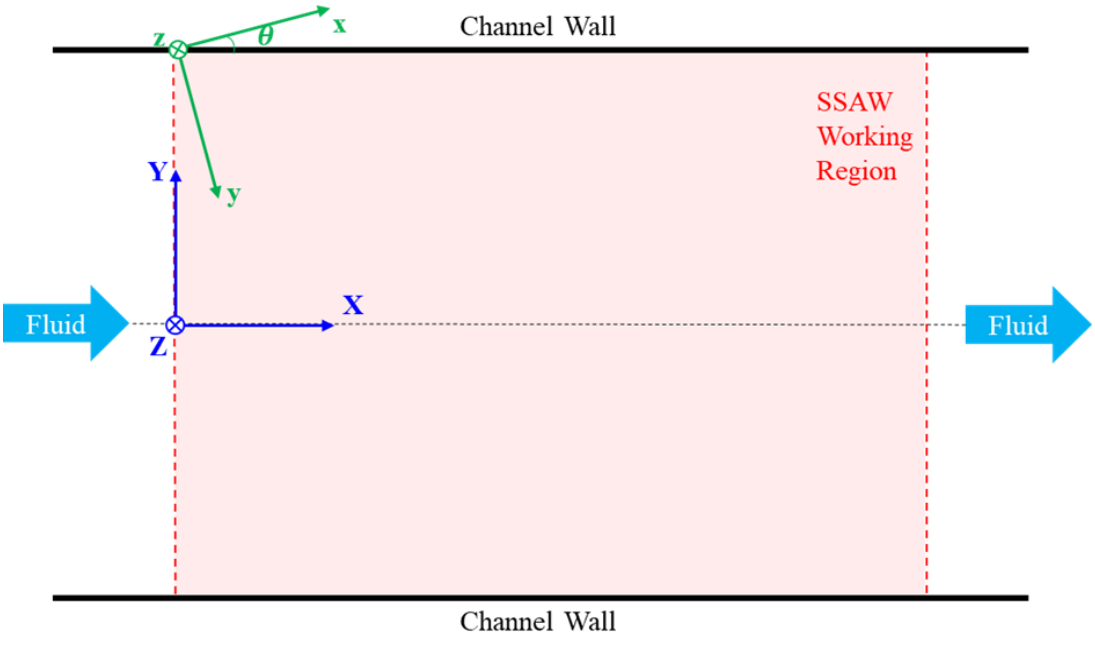

Fig. 4.4 Demonstration of XYZ and xyz axes sets from a plan view of the microfluidic channel

The coordinates of the two coordinate systems can be related by the following equation,

$$x = \mathrm{X}\cos(\theta) + Y\sin(\theta), \tag{58}$$

$$y = X\sin(\theta) - \left(Y + \frac{w}{2}\right)\cos(\theta), \tag{59}$$

Given the position axes aligned with the IDTs (xyz coordinate axis), it is possible to obtain a formula for the velocity acting on the particle in these directions. The particle's velocity in the y-direction is composed of two components, one due to the acoustic radiation force and another due to the fluid velocity. The velocity of a particle in the x-direction is determined only by the velocity of the fluid *t*, as no radiation force is exerted in this direction. A mathematical calculation of these particles' velocity yields (60) and (61),

$$u_y = u_r + u_f\sin\theta \tag{60}$$

$$u_x = u_f\cos\theta \tag{61}$$

The velocity $\boldsymbol{u_r}$ due to acoustic radiation force in fluid flow is derived by assuming that inertial effects are negligible and equating the acoustic radiation force (Eq.45) to the Stokes drag force (Eq.47) acting on the particle,

$$u_r = \alpha\frac{\pi R_\mathrm{P}^2\beta_\mathrm{m}P_\mathrm{I}\rho_\mathrm{s}c_\mathrm{s}}{9A_\mathrm{w}\lambda\mu}\sin(2ky) \tag{62}$$

The velocity of the microchannel fluid, which the particle is suspended in, $\boldsymbol{u_f}$, is given in

$$u_f = \frac{h^2\nabla p}{2\mu}\left[1 - \frac{Z^2}{h^2} + 4\sum_{n=1}^{\infty}\frac{(-1)^n}{{a_n}^3}\left(\frac{cosh\left(a_n\frac{Y}{h}\right)}{cosh\left(a_n\frac{w}{h}\right)}\right)cos\left(a_n\frac{z}{h}\right)\right] \tag{63}$$

The pressure gradient, ∇p, is calculated as the following equation,

$$\nabla\mathrm{p} = \frac{\Delta p}{L} = \frac{12\mu Q}{h^3 w\left(1 - 0.63\frac{h}{w}\right)} \tag{64}$$

To solve the particle's trajectory, the velocity equation equations are rewritten in differential form as follows.

$$\frac{\mathrm{d}y}{\mathrm{d}t} = u_r + u_f\sin\theta \tag{65}$$

$$\frac{\mathrm{d}x}{\mathrm{d}t} = u_f\cos\theta \tag{66}$$

Combining Eqs.(62) and (63), solving these ODEs, and evaluating the solution over a range of times will continuously output the particle's position in the microchannel and hence its trajectory.

Before solving, I need to analyse the velocity of the fluid. The fluid velocity is computed by applying Eq.63 in the program and dealing with the infinite summation using the built-in MATLAB symbolic summation function 'symsum'. By doing this computation over a range of different Y positions over the channel width and assuming that the Z position at the channel center is constant, it is possible to build a velocity distribution for a specific experimental setup. The figure illustrates the aforementioned fluid velocity distribution for a device configured with an 800 µm wide channel.

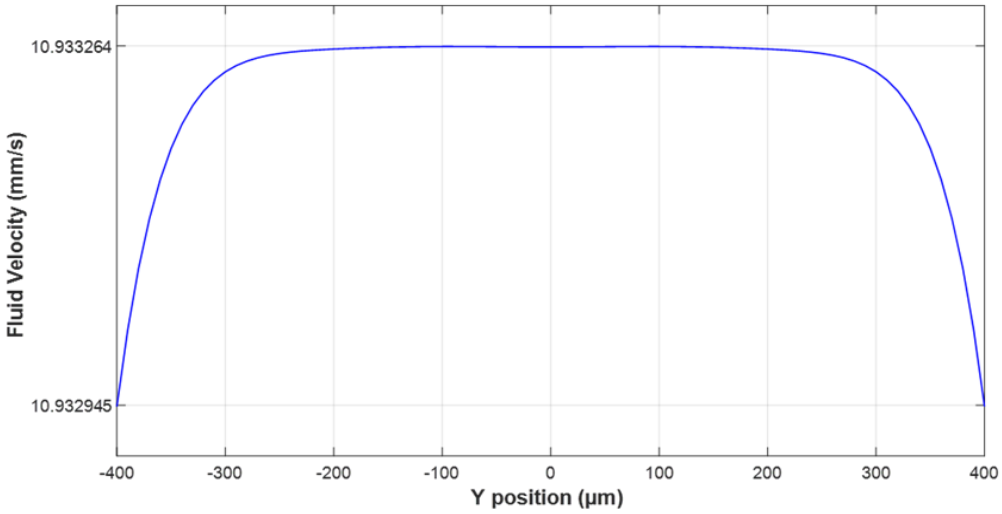

Fig. 4.5 Example Fluid Velocity Distribution Across a Microchannel Width.

Several essential elements can be seen in the distribution in **Fig. 4.5**. The fluid velocity is constant throughout a substantial portion of the channel's middle, for starters. Furthermore, when the minimal velocity observed close to the channel wall is compared to the velocity at the channel's center, there is only a 0.0029 percent difference.

I compared the workload generated by including the whole velocity distribution and simply

using the fluid velocity's central value when executing the application. It was discovered that running the program with the complete velocity distribution took 1433 percent longer than running it with the fluid velocity constant. Because the variation in fluid velocity is small enough not to influence the simulation, the authors elected to treat the distribution of fluid velocity along the channel's width as a constant.

I also require other crucial parameters for the calculation, such as the initial Y position and evaluation time. The initial Y position is the particle's Y coordinate value as it enters the microchannel's SSAW working area. The user must provide the beginning Y position range to be evaluated, which allows the computer to analyze the particle's trajectory within a defined range of initial values, which is required due to the variety of such initial positions in practice. The simulation can be repeated for these two initial conditions by entering a maximum and minimum Y position, resulting in a range of trajectoires as an output. It is worth mentioning that the starting X and Z locations are set to zero, reflecting the start of the SSAW working area in the length direction and the channel center in the height direction. Notably, the initial Y position reflects the experimental observation's location, which substantially impacts the trajectory simulation. The diagram below depicts a plot of the pressure node and anti pressure node lines created in the microchannel working region to demonstrate this.

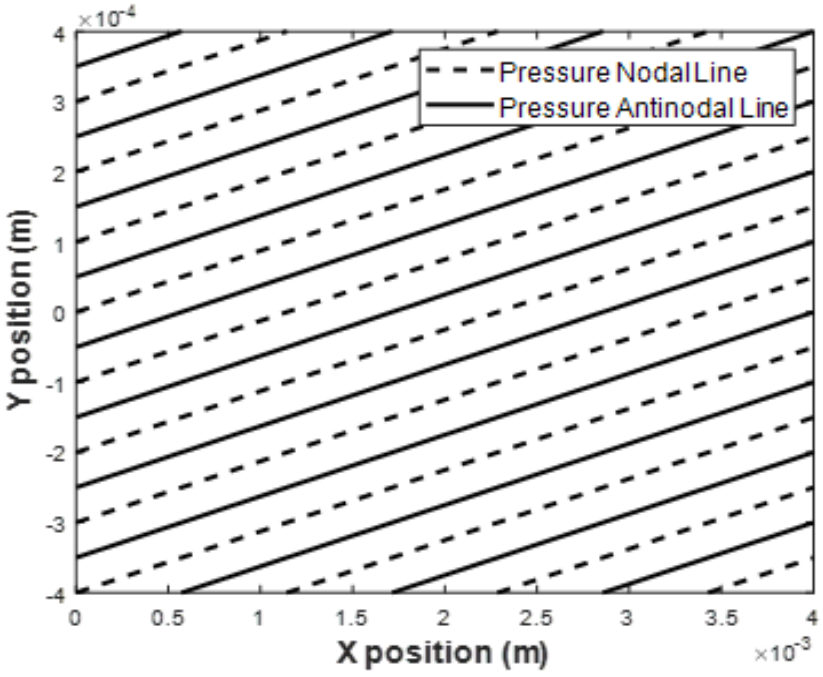

Fig. 4.6 Plot of the pressure node and antinode lines generated in the working region of the microchannel.

The pressure lines in **Fig.4.6** indicate how the beginning Y position substantially impacts the simulated trajectory since the particle will experience varying SSAW induced pressure fields as it travels along the X-direction at different initial Y values. Furthermore, with high IDT input power, this beginning position determines which pressure nodal line the particles tend to align with, dictating their course.

Evaluation time was set in the software to acceptable values to enable a full trajectory simulation with good resolution. The time duration specifies how long the program will assess the trajectory, whereas the time step determines how many sample points will be analyzed.

Cell trajectories were evaluated for a range of initial Y positions to represent the actual circumstance. Two trajectories were generated, one with the maximum initial Y position and one with the minimum initial Y position. After simulating these two trajectories, the area between these two trajectory lines might be colored to reflect the area where the actual cell trajectory would be expected to be followed.

4.4.2 Algorithm for cell mechanophenotyping

I intend to accomplish cell mechanophenotyping with cells' trajectories in microcirculation channels. The authors' first method was to apply image processing techniques to the experimental trajectory video results, but this approach has several significant flaws. First, the durability of the image processing was not assured; susceptibility to camera brightness variations and the requirement for high-quality photos limited the method's application. Second, the issue discovered was that once the cell's trajectory was aligned with the pressure node line, the approach could not determine a unique solution for cell characterization. Although this method was not used in the study, the authors thought it was necessary to discuss because it cost a significant amount of time and effort. More importantly, it resulted in the outcomes of the method provided in this chapter.

One crucial finding was made when constructing the previously mentioned video processing method. Using the trajectory simulation program, by plotting trajectories for a given experimental set up, with a specified input power and particle size, it was observed that there existed a φ value that achieved convergence to the pressure nodal lines. An illustration of this is shown below.

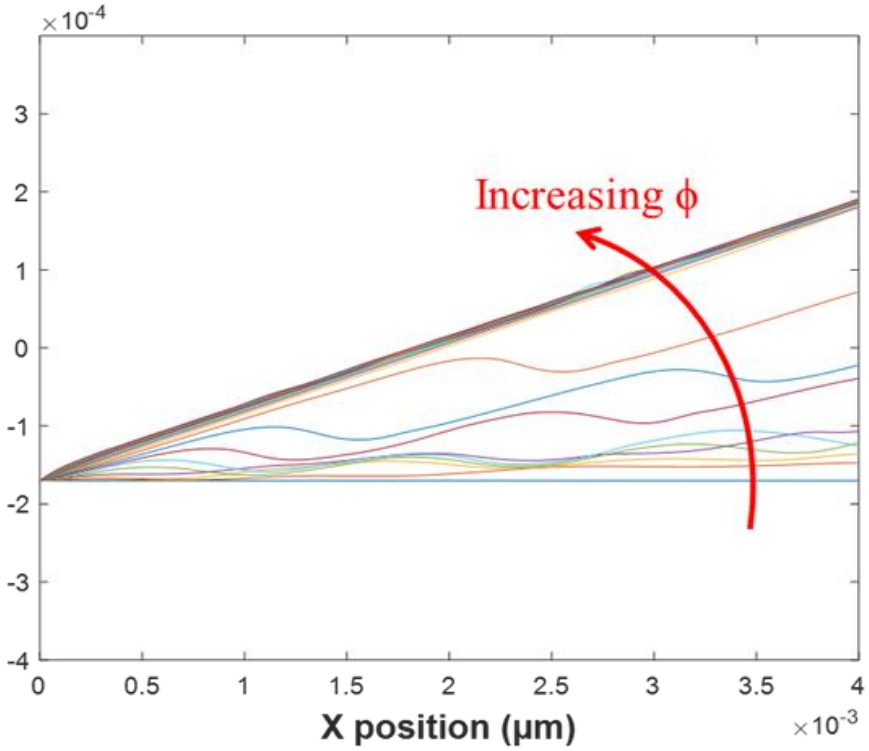

Fig. 4.7 Plot of the effect of incrementing the acoustic contrast factor, φ, on simulated trajectories.

The key observation in **Fig.4.7** is that as the value of φ increases, the trajectory becomes more aligned to the pressure node line, which makes sense as a more significant φ leads to a larger velocity due to acoustic radiation forces. At a particular value of φ, the trajectory plotted can be seen to align with the pressure node line, behaving as an almost linear trajectory. Beyond this value of φ, the trajectory does not change much, which is why the video processing method is ineffective.

By tuning the input power, I can control different cells to follow the similar trajectory converging to the PN line. The benefit of using only the input power as the input variable to determine the mechanical properties of cells is the simplicity of reading power values from power meters. This can eliminate the use of a high-profile camera to capture the migration path and simplify the calculation of the acoustic contrast factor and compressibility. By solving Eqn (1)-(5), the velocity of the cell in the ETA device can be expressed by,

$$u = A\varphi \sin(2kx) + u_{\mathrm{f}}, \tag{67}$$

$$A = \alpha \frac{\pi R_{\mathrm{P}}^2 \beta_{\mathrm{m}} P_{\mathrm{I}} \rho_{\mathrm{s}} c_{\mathrm{s}}}{9 A_{\mathrm{w}} \lambda \mu}, \tag{68}$$

where A is considered as the velocity amplitude induced by the acoustic radiation force. Considering the cells' movement time (T) in the channel, the displacement (S) of the cell can be described by integrating the velocity over time,

$$\boldsymbol{S} = \int_0^T u \, \mathrm{d}t = \int_0^T A\,\varphi \sin(2kx) + u_{\mathrm{f}} \, \mathrm{d}t. \tag{69}$$

Given the inclined angle of θ between the IDTs alignment and the channel centreline as shown in **Fig. 1a**, Eqn (69) can be transformed into:

$$\boldsymbol{s}_{\mathrm{x}} = \int_0^T [-A\,\varphi \sin(2kx) \sin\theta + u_{\mathrm{f}}] \, \mathrm{d}t, \tag{70}$$

$$\boldsymbol{s}_{\mathrm{y}} = \int_0^T A\varphi \sin(2kx) \cos\theta \, \mathrm{d}t \tag{71}$$

where $\boldsymbol{s}_{\mathrm{x}}$ is the transverse component of the displacement in the channel and $\boldsymbol{s}_{\mathrm{y}}$ is the longitudinal component of the displacement. For the channel of a rectangular cross-section with the width w, height h, the flow velocity can then be given by the following equation,[114]

$$u_{\mathrm{f}} = \frac{4h^2 \Delta P}{\pi^3 \mu L} \sum_{n,\mathrm{odd}}^{\infty} \frac{1}{n^3} \left[1 - \frac{\cosh\left(n\pi \frac{x}{h}\right)}{\cosh\left(n\pi \frac{w}{2h}\right)} \right], \tag{72}$$

where ΔP is the pressure difference over the channel length L. Assuming a fixed wavenumber k and a fixed flow velocity u_{f}, the product of A and φ indicates the influence of $\boldsymbol{F}_{\mathrm{r}}$ on the cell trajectory. Under the conditions that the device and fluid conditions are unchanged, the product of A and φ shall be the same for any cells following the same trajectory, regardless of the cell mechanical properties. To obtain the product of A and φ under the same device and fluid conditions, a reference microparticle with its known mechanical properties is introduced into the microchannel. The input power is recorded and the trajectory of the microparticle motion is precisely tracked. The product of A and φ for this experiment can be calculated, which is recorded as $A_1\varphi_1$. For other unknown microparticles, by adjusting the input power to recreate the same trajectory with the reference microparticle experiment, the A of the unknown microparticle can then be calculated using Eqn (68). The acoustic contrast factor φ of the unknown microparticle can then be obtained by,

$$\varphi = \frac{A_1 \varphi_1}{A}. \tag{73}$$

I define the trajectory of the reference microparticle as the reference trajectory, and $A_1\varphi_1$ as the reference product. For any other microparticle following the reference trajectory, substituting Eqn (69) into Eqn (73), the acoustic contrast factor can be described by

$$\varphi = \frac{9A_1\varphi_1\lambda\mu A_{\mathrm{w}}}{\pi R_{\mathrm{P}}^2 \alpha P_{\mathrm{I}} \rho_{\mathrm{s}} C_{\mathrm{s}} \beta_{\mathrm{m}}} \tag{74}$$

Therefore, the acoustic contrast factor of any cell/fluid combination can be calculated once the cell radius and the device input power are known. Finally, transferring Eqn (46) to determine the compressibility of cells by substituting the acoustic contrast factor values to

$$\beta_{\mathrm{P}} = \left(\frac{5\rho_{\mathrm{p}} - 2\rho_{\mathrm{m}}}{2\rho_{\mathrm{P}} + \rho_{\mathrm{m}}} - \varphi\right)\beta_{\mathrm{m}}. \tag{75}$$

Chapter 5 Design and fabrication of the SAW devices

5.1 The Design of Acoustofluidic Devices

5.1.1 Typical SSAW device

Fig.5.1 depicts the typical SSAW device 's schematic, which consists of two IDTs and a microchannel attached to the substrate in the space between the IDTs. The two PNs of the SSAW can be placed close to the microchannel's two walls while an AN form in the middle thanks to the width of the microchannel being roughly half the wavelength of the SAW. Two sheath flows are used to control the sample flow width by adjusting the flow rate ratio between the sample and sheath when a sample containing microspheres or cells is introduced from the sample intake. The same radio frequency (RF) signal drives both IDTs, resulting in rayleigh SSAW. Two sheath flows are employed to control the sample width entering the acoustic field by adjusting the flow rate ratio between the sheath and sample. A sample containing microspheres or cells is injected from the sample intake. While other samples are taken from the center outlet, microspheres or cells that are controlled and acted upon by acoustic radiation force travel towards PNs and to be collected at the two sheath exits. Each IDT has 40 pairs of finger electrodes, each with a 50 μm finger width, 1 cm finger length, and 200 m finger pitch. On both IDTs, there are 3 mm between the initial front finger's centers. By measuring the S parameter on a vector network analyzer (VNA, E5061B ENA, Keysight Technologies, U.K.) and sweeping the frequency on a signal generator (RS Pro Arbitrary Waveform Generator), which generates a SAW wavelength of 200 μm, it was determined that the IDT's operating frequency is 19.6 MHz. The microchannel's inlet, outflow, and height are each 100, 80, and 60 millimeters wide, respectively. The central section of the microchannel, known as the acoustic active area, is 120 μm wide. In order to stabilize the flow, the exit channel's width is increased to 200 μm.

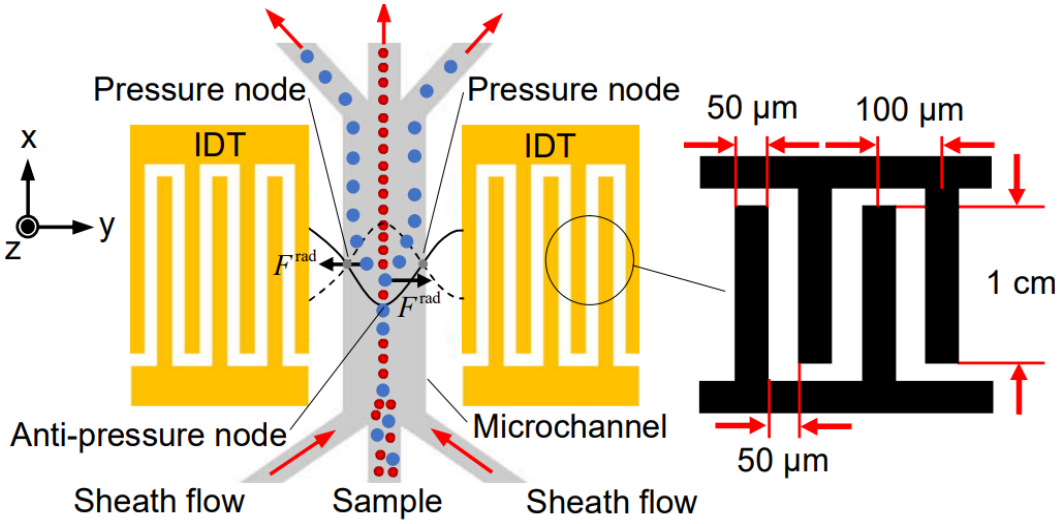

Fig. 5.1 Schematic of the parallel IDTs SSAW device integrating a pair of IDTs and a microfluidic channel, and the dimension of the IDT design. Two opposite IDTs generate SSAW and form PNs where samples are introduced and focused from the inlets are dominated and actuated by acoustic radiation force. Samples migrated to the PNs are collected by the two sheath outlets.

5.1.2 Filled tilted-angle (FTA) IDT device

Tilted-angle SSAW (taSSAW) devices, based on the typical SSAW device, were created to provide more excellent performance while separating cells. The taSSAW device operates on the same principles as the typical SSAW separation device. The main distinction is that the microchannel of the taSSAW device is positioned at an angle to the IDT electrodes, whereas the typical SSAW separation device is parallel to the channel. Due to the tilt angle between the IDEs and microchannel, pressure node lines created by the SSAWs in fluid flow are at an angle to the fluid flow. In the figure below, you can illustrate such a configuration.

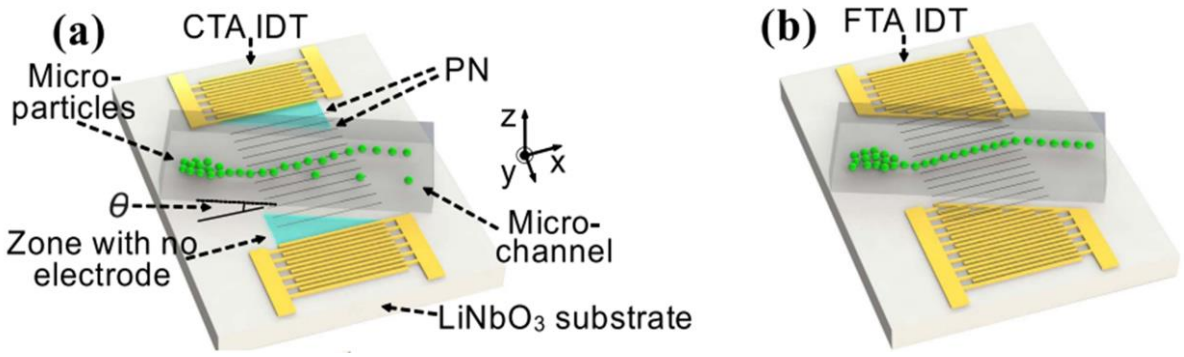

Fig. 5.2 Schematic comparison of a Conventional Titled-Angle (a) and a Filled Tilted-Angle (b) IDT device.

Fig. 5.2a schematic illustrates a typical tilted-Angle (CTA) device with a tilt angle between the IDEs and the microchannel. Concentrating microparticles in the CTA's microchannel will pass across many pressures node (PN) lines unless they follow a pressure node. The primary benefit of having the microparticles cross several PN lines requires less IDT input power to separate particles with characteristics. CTA devices have significant separation efficiency and sensitivity benefits over typical devices. A variation on the CTA is the Filled Tilted-Angle (FTA) device, which is depicted in **Fig. 5.2b.** The FTA is distinguished by the addition of IDE fingers to the cyan-shaded triangular sections of the substrate in the CTA. The FTA device increase separation efficiency by lowering the device's working area and raising the acoustic pressure amplitude.

5.2 Fabrications of interdigital transducers

5.2.1 Photolithography and deposition of interdigital transducers patterns

Photolithography is a technique for transferring patterns onto a substrate using light. All photolithography methods follow this principle. First, the photoresist is placed on the substrate. The substrate is then exposed to electromagnetic radiation, which changes the molecular structure and then the solubility of the material,[121] while a mask of the pattern is placed. After exposure, etching is carried out. The substrate is then immersed in a developer solution.

Developer solutions are usually water-based and can dissolve areas of photoresist exposed to light. There are five steps in a complete photolithography process, wafer preparation, spin coating, development, metal deposition and etching.

A. Wafer preparation

Two materials were selected as the wafer for the SAWs-based system, Lithium niobate ($LiNbO_3$) and Gallium nitride (GaN).

The $LiNbO_3$ is a commonly used piezoelectric material for fabricating acoustofluidic devices due to its outstanding electromechanical coupling coefficient. The $LiNbO_3$-based microfluidic system is developed in the fields of cell detection and separation, liquid manipulation, etc. Because of portability, high sensitivity, cost effectiveness and simple construction, The LiNbO3-based microfluidic system also serves as an excellent lab-on-a-chip equipment.

however, LiNbO3 has a very low thermal conductivity (0.044 W/ (cm·K)), which causes challenges for operating the acoustic tweezer at high powers for high-throughput manipulation of biological cells. GaN is an alternative piezoelectric material recently discovered by Sun et al. that can be used to produce acoustic surface waves for the efficient manipulation of microparticles.[122] Despite that the electricmechanical coupling coefficient of GaN is lower than that of the LiNbO3, GaN thin film is a thermally robust material for high power SAW generation and acoustic tweezers based on GaN demonstrated efficient SAWs produced on the surface with less power reflected, which is invaluable to handle biological samples when using high input power for high-throughput applications. The GaN-based microfluidic system was developed to address the problem of high temperatures when manipulating biological cells at high power and high throughput in LiNbO3-based microfluidic systems due to the very low thermal conductivity of lithium acids (0.044 W/(cm-K)).[123] The high power of the interdigital sensor (IDT) applied to the LiNbO3 wafer generates considerable Joule heat, which is often not efficiently dissipated through LiNbO3, resulting in damage to the LiNbO3 substrate and biological sample.[124] Although the lower effective electromechanical coupling coefficient of GaN can be compensated by increasing the applied electrical power, the good thermal conductivity of GaN ensures the stability of the system and the activity of the biological sample

at high power in GaN systems. GaN-based thin-film devices can also overcome the expensive and brittle nature of bulk LiNbO3 materials and allow SAW functionality by depositing piezoelectric films where acoustic waves are required.[125] GaN has a higher speed of sound than LiNbO3, which allows GaN-based SAW devices to achieve higher resonant frequencies for the same IDT period than LiNbO3-based devices. In addition, the two-dimensional electron gas on which GaN HEMTs are based can be used as an IDT to eliminate mass loading and signal reflection.[126]

In order to verify the accuracy of the simulation model for different piezoelectric materials, I fabricate two IDTs with $LiNbO_3$ and GaN wafer respectively. $LiNbO_3$ wafer is 3 inches, 128° Y-cut, 0.5mm thick and double-side polished. The GaN wafer is a thin film which was grown on a sapphire substrate in [0001] direction, The GaN and sapphire layers are measured to be ~4.5 μm and ~600 μm thick. Numerical and experimental studies of them are shown in later chapters. For subsequent strong and uniform photoresist adhesion, wafers are cleaned in a fume cupboard by being rinsed with acetone, methanol and isopropanol (IPA), respectively. The wafers are then dried by a nitrogen gun blowing.

B. Spin coating

Spin coating is performed in three steps, deposition, spin up and spin off as shown in **Fig. 5.3**. In the first stage the photoresist is deposited on the wafer which is placed on the turntable and then spin up and spin off occur in sequence. The photoresist on the turntable is distributed via centrifugal force. High spinning speed results in thinning of the layer. Thickness of the deposited layer is controlled by the viscosity of the coating solution and the speed of rotation. For the spin coating (4000 rpm, 60 secs,), the AZnLoF 2070 photoresist is deposited on the wafer as 5.5 μm layer, which is followed by a soft bake to strengthening the structure (110 °C, 90 secs).

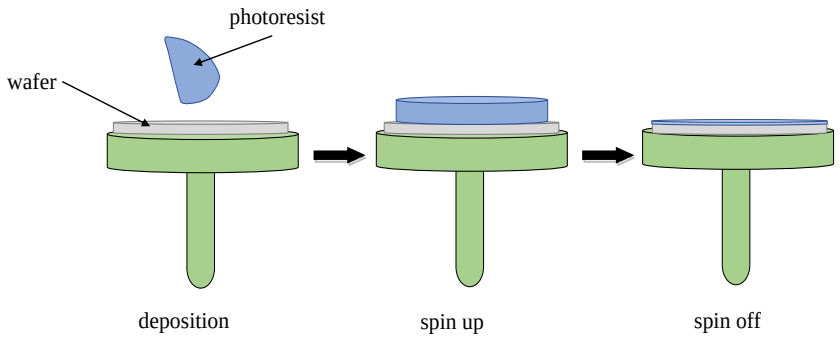

Fig. 3.3 The process of spin coating. The photoresist is deposited on the wafer and followed by spinning up and spinning off.

C. Development

As, shown in **Fig. 5.4**, the wafer with a resist layer of 5μm thin is placed under a mask aligner. UV radiation is emitted through a reticle containing the pattern to be transferred onto the resist. By controlling the UV intensity and exposure time, a precise pattern can be produced. Under the UV exposure (83 mW/cm^2) for 40 secs, the resist becomes more solid. The patterns are the solid part of the thin layer resist left on the wafer after rinsing in the developer.

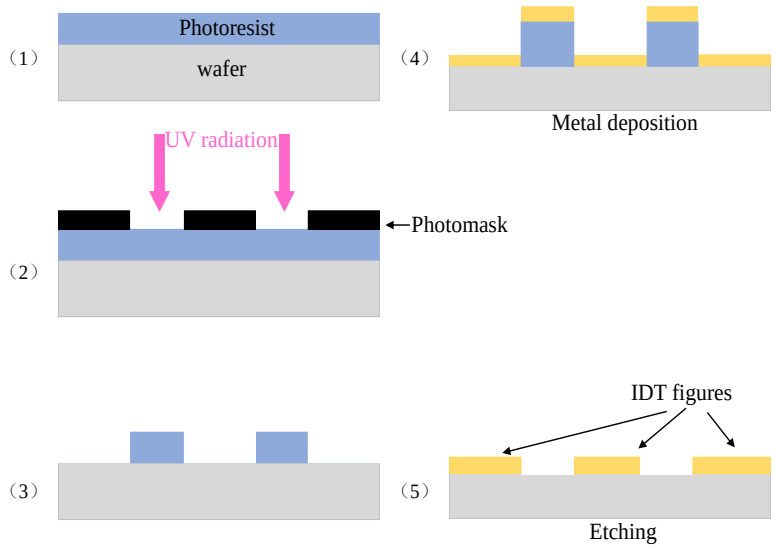

Fig. 3.4 The process of mask alignment, development and wet etching for IDT fabrication. Metal is deposited on the wafer with resist patterns after development, then the IDT fingers are fabricated by the wet etching.

D. Metal deposition

Several properties must be considered when selecting metal materials for pattering finger electrodes on piezoelectric substrates to develop IDT, including substrate adhesion, resistivity, and boiling point. Table 2 displays the metal properties of commonly used IDT fingers. Adhesion is critical for bonding between digital interelectrode and piezoelectric substrates because high adhesion can reduce IDTs wear and even finger loss from the substrate during equipment assembly and transportation, resulting in IDTs being used for a more extended period. Lower resistivity enables lower joule heat generation and improved energy conversion. The boiling point determines the method of depositing the electrode layer onto the substrate that can be used. If the boiling point is low, a thermal evaporation method, which is less expensive, simpler, and faster, can be used. [127] Copper appears to be the most appealing material based on those parameters, but it diffuses into the substrates.[128] Although gold has poor substrate adhesion, it has a lower resistivity, which means the device can be more efficient. It also has the appropriate boiling point, allowing for thermal evaporation methods. As a result, gold is chosen as the material for patterning electrodes.

Table. 2 Properties of electrode materials

Metal	Adherence	Electraical resistivity (μΩ · cm)	Boiling point (K)
Copper	Good	1.7	3200
Aluminum	Good	2.65	2792
Gold	Poor	2.2	3129
Tungsten	Average	5.0	5828
Titanium	Good	50	3560

The Edwards 306A thermal evaporator is used to deposit metal for the patterning of electrodes. As shown in **Fig. 5.5**, the evaporator is made up of a single removable glass bell jar chamber that is pumped by a turbopump and backed up by a rotary pump. In addition, the rotary pump is used to pump the gases from atmospheric pressure. The thermal deposition process begins by opening the chamber and placing the wafer with resist patterns facing down on the substrate holder inside the chamber. The vacuum chamber is sealed after Cr and gold are placed in

separate crucibles. The system is cooled with water, and the rotary pump is turned on until the pressure inside the chamber reaches 5×10^{-2} mbar. After 30 minutes, switch the rotary pump to the turbopump and fill the diffusion pump with liquid nitrogen until the chamber pressure falls below 4×10^{-6} mbar. After closing the turbopump, the evaporated material is heated by increasing the system voltage to 70 volts. The system measures the mass of the material deposited on the wafer in real-time and converts it to thickness. The crucible is switched to the gold-containing one after depositing a 20 nm layer of Cr as the adhesion layer. The evaporation process is repeated until a layer of gold deposition of 100 nm is obtained.

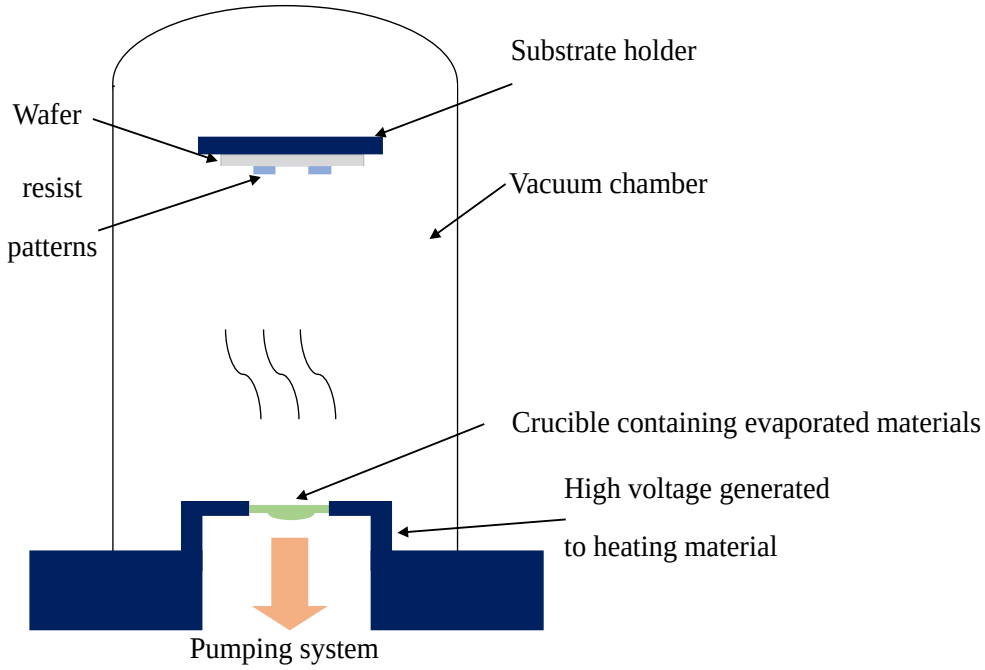

Fig. 5.5 The schematic diagram illustrates the heat evaporation mechanism used to deposit IDT electrodes. The targeted material is evaporated in the vacuum chamber from the electrically heated crucible toward the substrate holder.

E. Etching

The remaining resist is removed in the final etching process, leaving the finger electrodes on the wafer. The wafer can be left in acetone overnight or placed in an ultrasonic bath with acetone to remove remaining resist quickly.

5.3 Fabrications of acoustofluidic microchannel

Micro-milling with a high-precision numerical control system allows for quick manufacturing of hard materials, but the spindle shape limits the microfluidic channel resolution.[129] Direct laser etching to create microchannels is a quick method, but it necessitates specific thermal degradation effect materials and strict control of critical parameters.[130]

The most commonly used material for making microfluidic channels is PDMS, which has the advantages of easy fabrication and low cost.[131, 132] Its transparency allows for real-time monitoring of SAW manipulation, and its acoustic impedance is close to that of water, preventing reflection in the flow.[133] Because of the need for precision and surface roughness in microparticle manipulation, PDMS was chosen as the microchannel material, and photolithography was used to fabricate it.

On a 3-inch single side polished silicon wafer with cleanroom facilities, the SU-8 2050 negative photoresist is used to fabricate the channel molding. Before using, the SU-8 is kept in a bottle overnight to remove any air bubbles that could affect the mask alignment quality. The wafer is cleaned with acetone, methanol, and IPA baths for 5 minutes before being blown with a nitrogen gun. The wafer is placed on a hot plate (180°C, 5 minutes) before resisting deposition to achieve a parched surface for strong resist adhesion. After resisting injection, the wafer is spin-coated in two stages (500 rpm for 15 secs and 2500 rpm for 45 secs) with a 200 rad/s^2 acceleration for an evenly distributed 60 um height layer. Pre-baking takes 3 minutes at 65 degrees, followed by nine minutes at 95 degrees, and post-baking takes 2 minutes at 65 degrees, followed by 9 minutes at 95 degrees. If air bubbles form during baking, the oven should be turned off until the bubbles have burst and then re-baked. The wafer is developed for 2.5 minutes in an ethylene carbonate solvent. Finally, the mold is baked at 180°C for 20 minutes and cooled on a hotplate to fix the resist structure on the wafer. As shown in **Fig. 5.6a**, Silicon elastomer (DOWSIL, SYLGARD 184) and curing agent (DOWSIL, RT Cure) are mixed in a ratio of 10:1 and stirred well. After vacuum treatment, the mixture is poured into a container with a channel mold at the bottom. In order to obtain a fine and stable channel surface,

PDMS needs to be cured naturally at room temperature for more than 48 hours or cured on a hot plate at 65 degrees for 2 hours. Under the PDMS block, a channel is formed after curing. holes are punched through the PDMS block to connect tubing. A photo of a PDMS microchannel is shown in **Fig. 3.6c**.

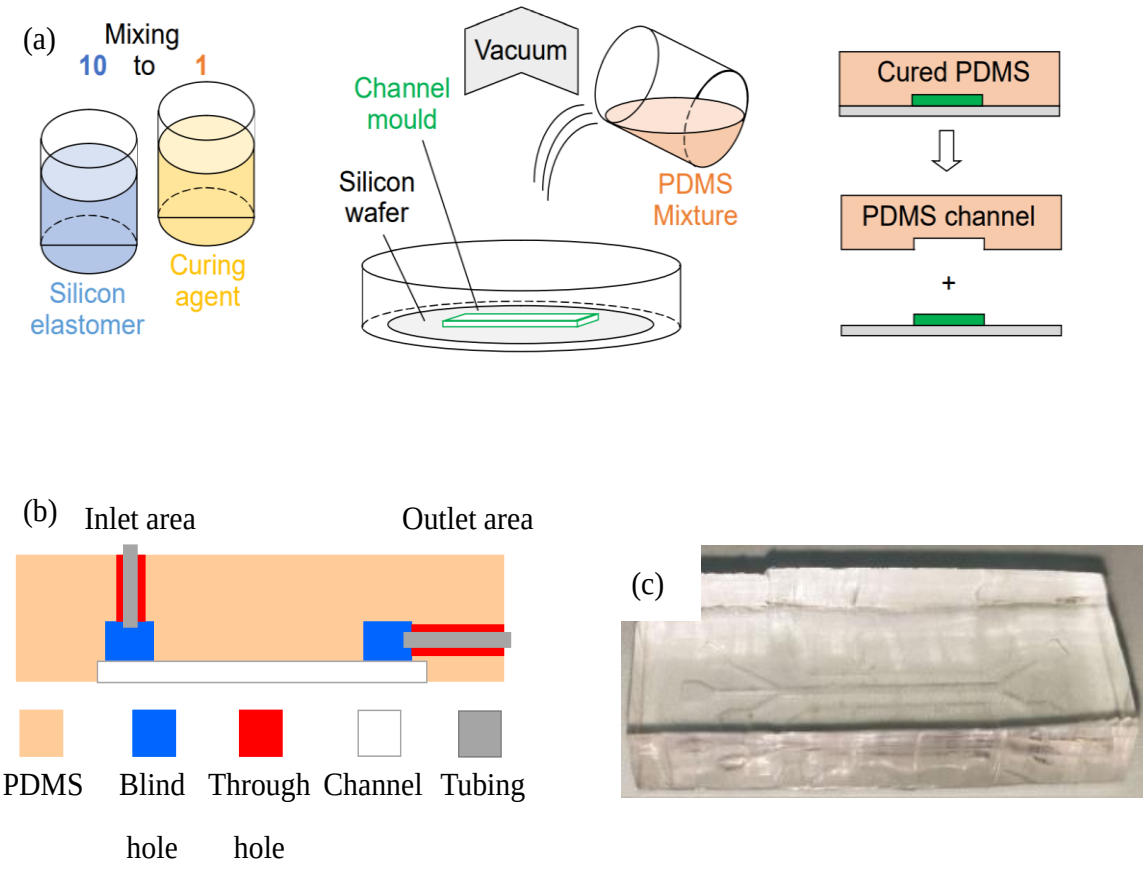

Fig. 5.6 (a)The moulding process of PDMS microfluidic channel fabrication. The silicone elastomer and curing agent are firstly mixed with a ratio of 10 to 1. The mixture is poured in a container with the channel mould followed by a vacuum treatment. The cured PDMS channel is peeled off from the mould. (b) The schematic of hole punching for tubing connection on a PDMS microfluidic channel. (c) the photo of a PDMS microfluidic channel.

5.4 Bonding and Pressing

The bonding of the microfluidic channel and the piezoelectric base with the IDT is essential because the leakage of the channel is likely to cause short circuit on the electrodes. People often use plasma treatment to bond the channel and the IDT wafer in the traditional process.

However, this method requires plasma processing equipment and difficult to recovery from leaks and blockage. I have developed a method of mechanical bonding that is easy to install and recover from leaks and blockage in the first place. In this method, a pressor is used to evenly apply pressure to the channel, making it seamless contact with the wafer. The structure is shown in the **Fig. 5.7**, screws are distributed on both sides of the pressure plate to adjust the pressure. A transparent acrylic plate is placed between the pressor and the PDMS channel to prevent the channel from being deformed and to allow the pressure from the screws to be evenly distributed on the channel. This technique is easy to assemble and disassemble, and in the event of leakage, PDMS channels and IDTs substrates can be quickly bonded and reused simply after cleaning.

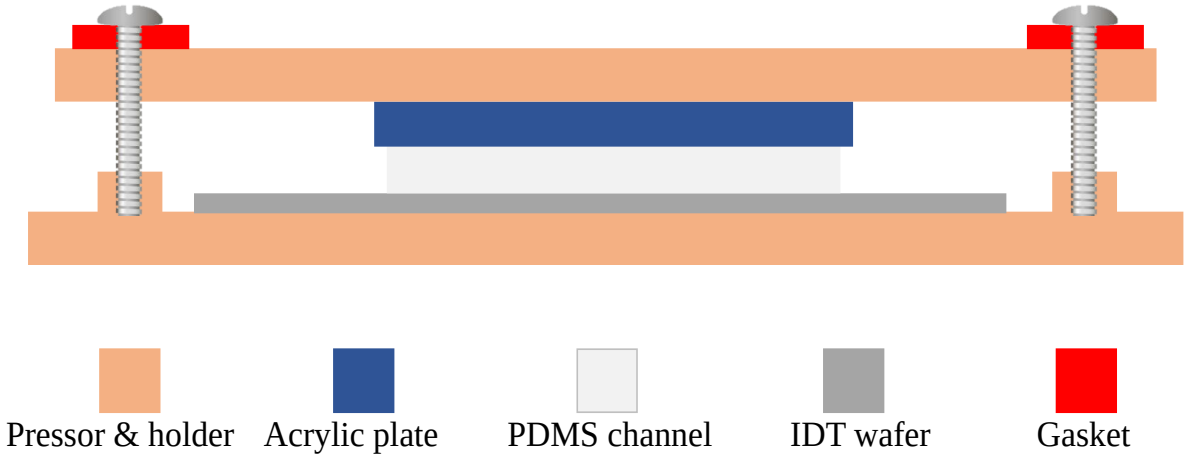

Fig. 5.7 The schematic of the mechanical bonding method for PDMS channel and IDT wafer. A pressor, acrylic plate, channel and IDT are placed on a holder, and fixed by screws and gaskets.

5.5 Characterisation of SAW systems

a) Characterisation of FTA and CTA Devices

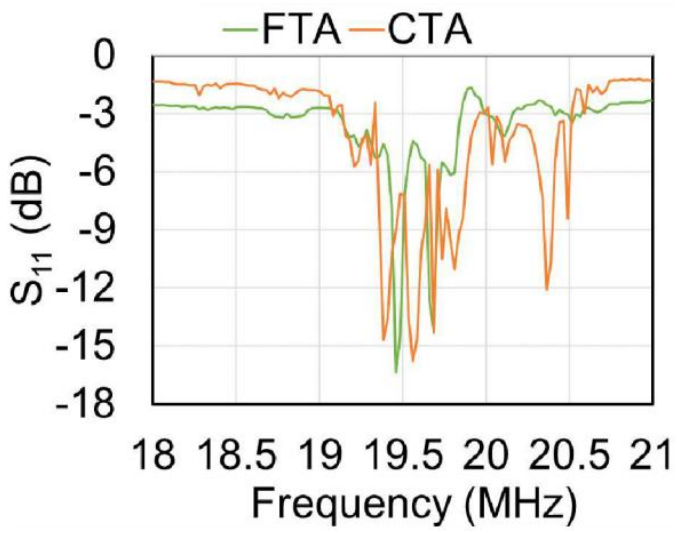

Fig. 5.8 The S11 parameters of the FTA and CTA Devices.

The reflection coefficients (Fig. 5.8), S11, of both the CTA and FTA devices were measured using a vector network analyzer. The FTA device shows a better Q factor allowing a higher energy conversion. The working frequencies of the FTA and CTA devices are 19.5 MHz and 19.6 MHz, respectively. A small difference may be caused by the capacitance and inductance introduced by the added electrodes.

b) Characterisation of GaNAT system

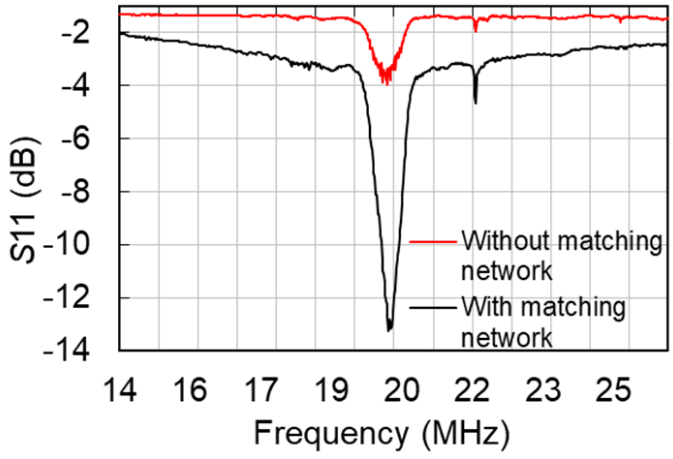

Fig. 5.9 The S11 parameters of the GaNAT system with and without the matching network.

The reflection coefficients (Fig. 5.9), S11, of both the GaNAT system with and without the matching network were measured using a vector network analyzer. The GaNAT system with

matching network shows a much better Q factor allowing a higher energy conversion up to -13 dB. The working frequencies of the GaNAT system with and without the matching network both are 19.8 MHz.

5.6 Conclusion

A complete acoustofluidic system for manipulating particles consists of two main parts: the IDTs and the channel. The IDT part is composed of electrodes and a piezoelectric substrate. In this chapter, I describe the fabrication process of the sensor in the conventional SAW system and the GaN system. The conventional SAW system is fabricated by etching gold electrodes onto $LiNbO_3$ using photolithography, and GaN replaces $LiNbO_3$ as material for piezoelectric bases in GaN systems. I also describe the processing of the microfluidic channels and the method of composition of the sensors. In the following chapters, I will use the different microfluidic systems fabricated with the work presented in this chapter to conduct particle manipulation experiments and compare the results with simulations to investigate the microfluidic properties of the various systems and verify the accuracy generalizability of the simulation models.

Chapter 6 Results and Discussion

6.1 Simulation of conventional SAW-PDMS system

To verify the accuracy of the simulation model, I compared the first-order acoustic pressure, first-order velocity, and second-order velocity of the SAW-PDMS transducer with that of published results.[134] The first-order acoustic pressure distribution comparison is shown in F**ig. 6.1a**. Along the y-axis, a visible standing wave pattern forms. The magenta arrows pointing up the wave radiation from the bottom to the top are indicated, the first-order acoustic pressure with a maximum amplitude of 12.9 kPa. The maximum magnitude of the first-order acoustic velocity distribution v_1 is 5.3 mm/s, as shown in **Fig. 6.1b. Fig.6.1c** depicts the time-averaged second-order velocity $\langle v_2 \rangle$, with a maximum magnitude of 1.47mm/s. The value of $\langle v_2 \rangle$ is negligibly small and rapidly decreases away from the bottom surface. The current numerical results are consistent with published numerical results, indicating that the current numerical model is reliable.

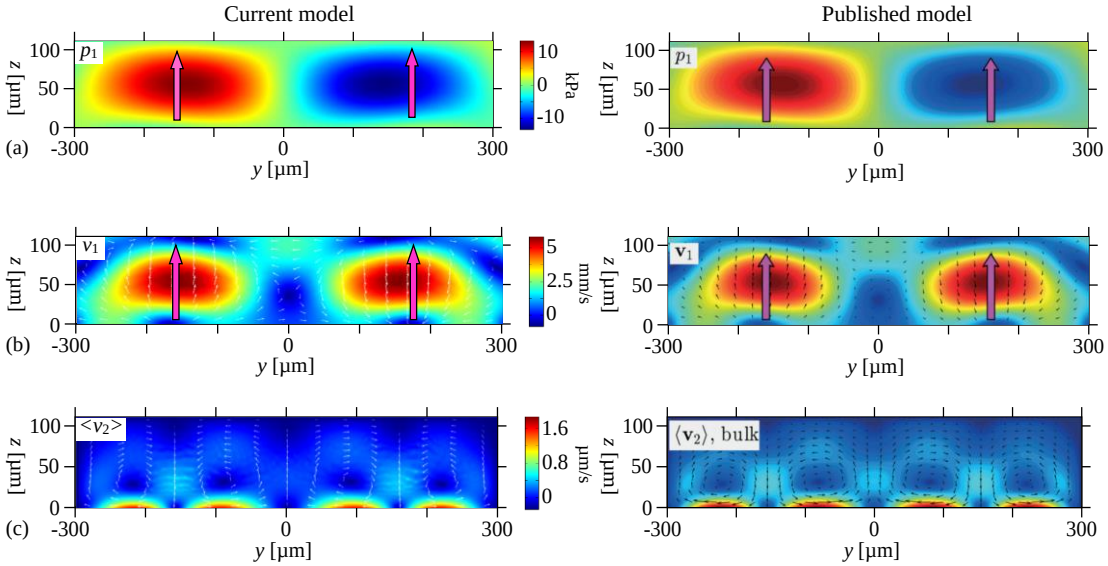

Fig. 6.1 Comparison between the current results (right) and published result (left): (a) first-order pressure field, (b) first-order velocity field, and (c) time-averaged second-order velocity field.

6.2 Simulation of novelty SAW systems

A. Acoustofluidic field and particle trajectories in SAW-PDMS and SAW-Glass channels

All simulations were performed with the wave frequency of 6.65 MHz or the angular frequency of 4.176×10^7 rad/sec. **Fig. 6.2a** shows p_1, the first-order pressure at t = 2πk/ω, where k is any integer in the SAW-PDMS and SAW-Glass microchannels. The pressure distribution in the SAW-Glass channel is similar to that reported by Wu's work[83], where the pressure anti-nodes located near the four corners of the channel. Comparing with the pressure distribution in the SAW-PDMS channel, the larger acoustic pressure range in the SAW-Glass channel attributes to the reflected acoustic energy at the water-glass interface.

Fig.6.2b shows $\langle v_1 \rangle$, the first-order velocity at t = 2πk/ω in the SAW-PDMS and SAW-Glass configurations, the amplitude of the actuation velocity (4.2 mm/sec) is less than the amplitude of the first-order velocity $\langle v_1 \rangle$ in both SAW-PDMS (5.5 mm/s) and SAW-Glass (38.0 mm/s) structures. The glass reflector reflects 89% of the acoustic energy at the water-glass interface allowing the acoustic wave to travel back to the channel, which results in approximately 7-fold increase in the first-order velocity comparing to that in the SAW-PDMS configuration. The time-averaged streaming velocities, $\langle v_2 \rangle$, in the SAW-PDMS and SAW-Glass are shown in **Fig. 6.2c**, with the maximum values of 1.47 μm/s and 5.93 μm/s, respectively.

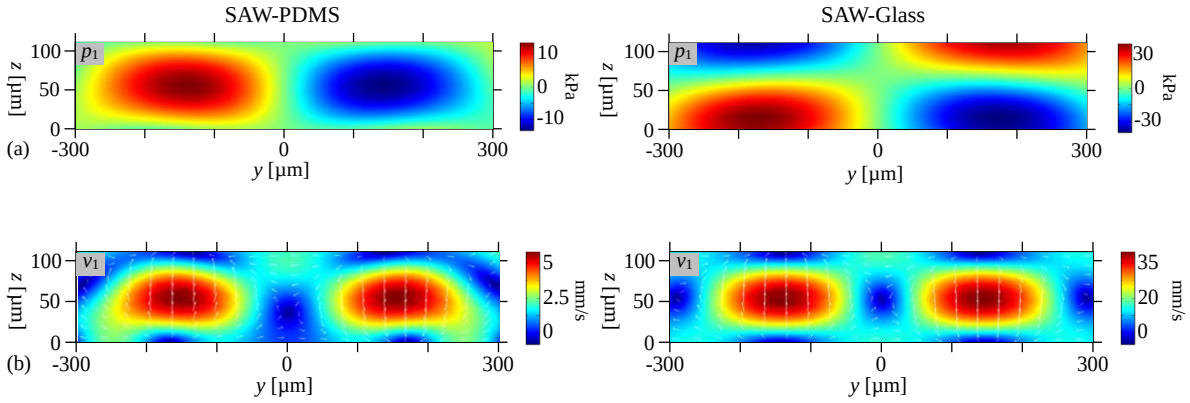

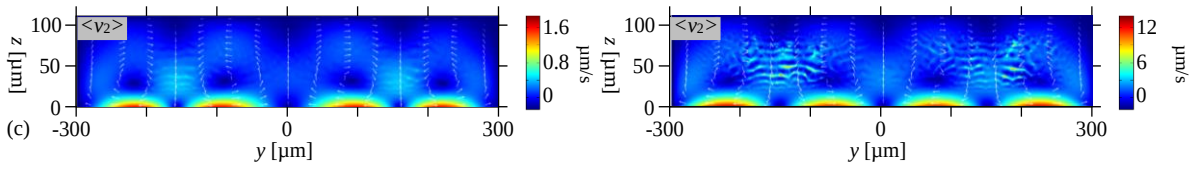

Fig. 6.2 Colour plots of the first-order acoustic pressure $\boldsymbol{p_1}$, the first-order velocity field $\boldsymbol{v_1}$ and the time-averaged second-order velocity $\langle \hat{\boldsymbol{v}}_2 \rangle$ in the SAW-PDMS and SAW-Glass channels. (a) The maximum pressure in the SAW-PDMS and SAW-Glass is 13.3 kPa and 33.6 kPa, respectively. (b) The amplitude of the first-order velocity in the SAW-PDMS and SAW-Glass is 5.5 mm/s and 38.0 mm/s, respectively. (c) The maximum second-order velocity in the SAW-PDMS and SAW-Glass is 1.6 μm/s and 5.93 μm/s, respectively.

The velocity and the trajectory of polystyrene microspheres with diameters of 1 μm, 5 μm, and 10 μm were simulated for both the SAW-PDMS and the SAW-Glass configurations, and the results for a period of 10s are shown in **Fig.6.3**. Both channel structures produce streaming rolls when the particle size is 1 μm (**Fig. 6.3a**), the particle velocity in the SAW-Glass channel is much higher than that in the SAW-PDMS. In **Fig. 6.3b**, 5-μm particles are mainly driven by the acoustic radiation force in the SAW-Glass resulting a faster transition to the pressure nodes, while the SAW-PDMS still shows strong streaming effects on the particles. **Fig. 6.3c** indicates a much higher velocity of 41.0 μm/s achieved in SAW-Glass for 10-μm particles. The particle velocity in the SAW-Glass is generally larger with the trajectory towards the middle of the channel on the z direction.

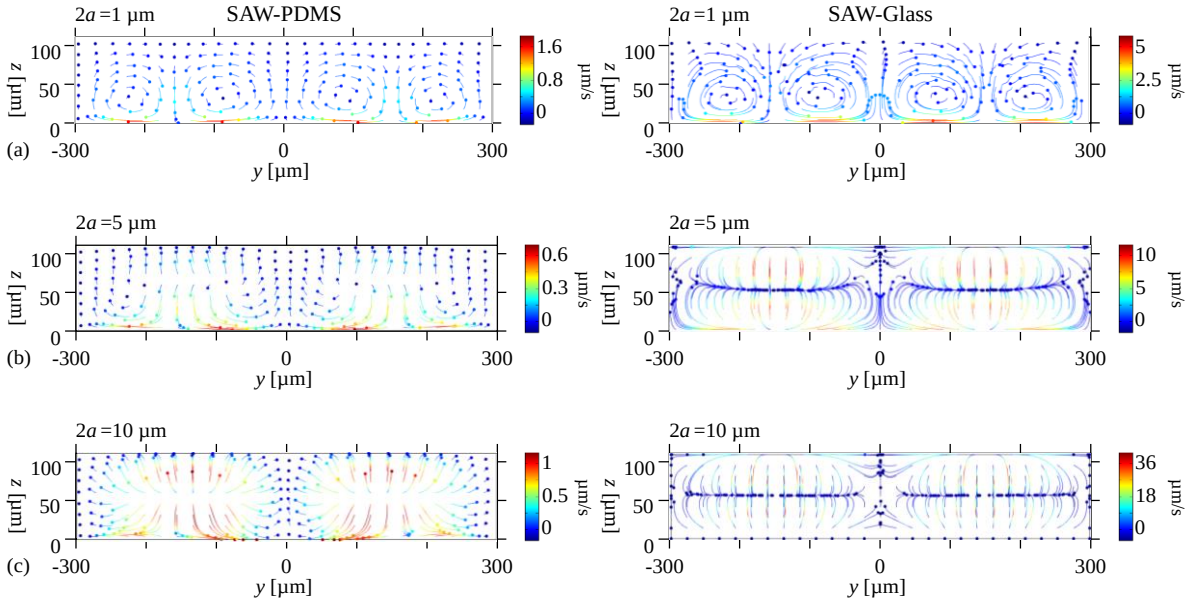

Fig.6.3 Particle trajectories and velocities in the SAW-PDMS and SAW-Glass configurations. (a) Particle size is 1 μm, the maximum velocity is 1.6 μm/s in SAW-PDMS and 5.6 μm/s in SAW-Glass. (b) Particle size is 5 μm, the maximum velocity is 0.5 μm/s in SAW-PDMS and 10.8 μm/s in SAW-Glass. (c) Particle size is 10 μm, the maximum velocity is 1.82 μm/s in SAW-PDMS and 41 μm/s in SAW-Glass.

B. Acoustofluidic field and particle trajectories in SAW-SAW channel

In the SAW-Glass channel, the reflected wave from the water-glass interface interacts with the wave in the water generated by the bottom SAW transducer to produce the PSW (pseudo-standing wave) on the z direction. The PSW can be further controlled by using another SAW to replace the glass positioned on the top of the microchannel. In the SAW-SAW configuration, the phase difference, $\Delta\varphi$, between the two SSAWs generated by the top and the bottom SAW devices can be controlled to manipulate the acoustic energy and pressure distributions within the microchannel. The first-order acoustic pressure p_1, the first-order velocity field v_1, and the time-averaged streaming velocity $\langle v_2 \rangle$ are shown in **Fig. 6.4**, where the left and right panels show the results for $\Delta\varphi = 0$ and $\Delta\varphi = \pi$, respectively.

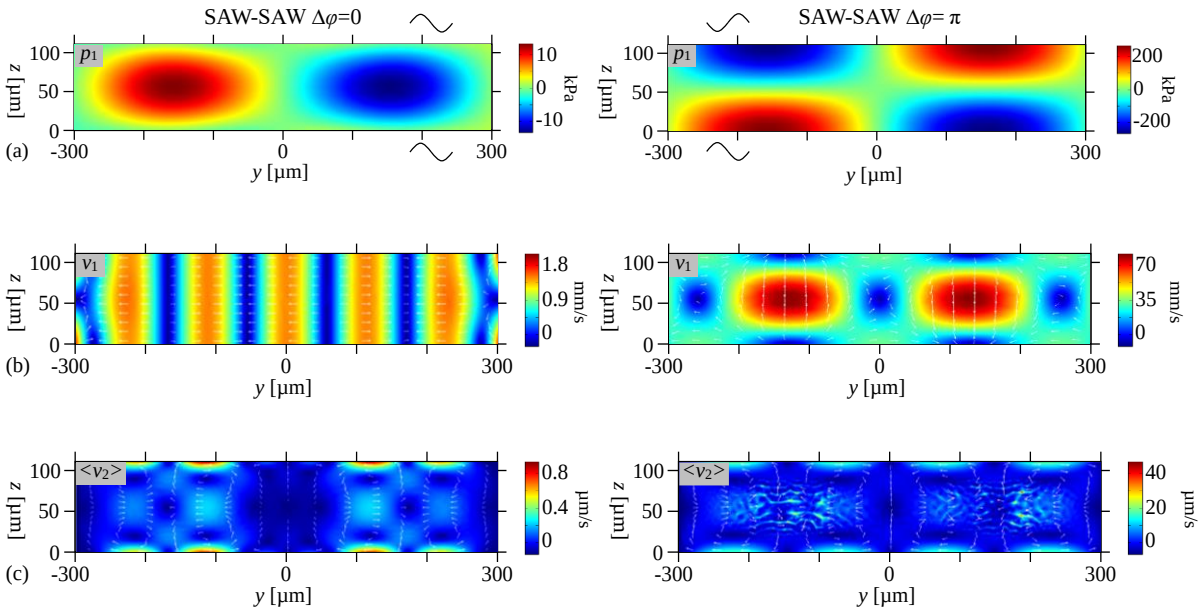

Fig. 6.4 Colour plots of the first-order acoustic pressure p_1, the first-order velocity field v_1 and the time-averaged second-order velocity $\langle \hat{v}_2 \rangle$ in the SAW-SAW channel. The left panel shows the phase difference Δφ = 0 while the right panel shows the phase different Δφ = π. (a) The maximum pressure is 14 kPa and 224 kPa, respectively. (b)

The amplitude of the first-order velocity is 1.8 mm/s and 70.0 mm/s, respectively. (c) The maximum second-order velocity is 0.8 μm/s and 31.0 μm/s, respectively.

Varying the phase difference $\Delta\varphi$ between the top and bottom SAW transducers can redistribute the pressure gradients and alter the pressure amplitude in the channel, due to the phase shift-induced changes in the positions of the nodes and the anti-nodes.[134] The dependence of the maximum acoustic pressure on $\Delta\varphi$ was obtained by sweeping the $\Delta\varphi$. The results are shown in **Fig. 6.5a**. The largest pressure that could be achieved was 232 kPa. It occurred at $\Delta\varphi = 5\pi/6$ or $7\pi/6$ with four pressure anti-nodes (**Fig.6.5b**). The smallest pressure was 14 kPa, occurred at $\Delta\varphi = 0$ or 2π (**Fig.6.5a**). The four pressure anti-nodes presented at $\Delta\varphi=5\pi/6$ or $7\pi/6$ are not entirely symmetrical, which could not produce useful particle trajectories for particle separation. The acoustic pressure of 224 kPa at $\Delta\varphi= \pi$, which is slightly lower than the maximum, is able to produce four symmetrical pressure anti-nodes (**Fig.6.5a**).

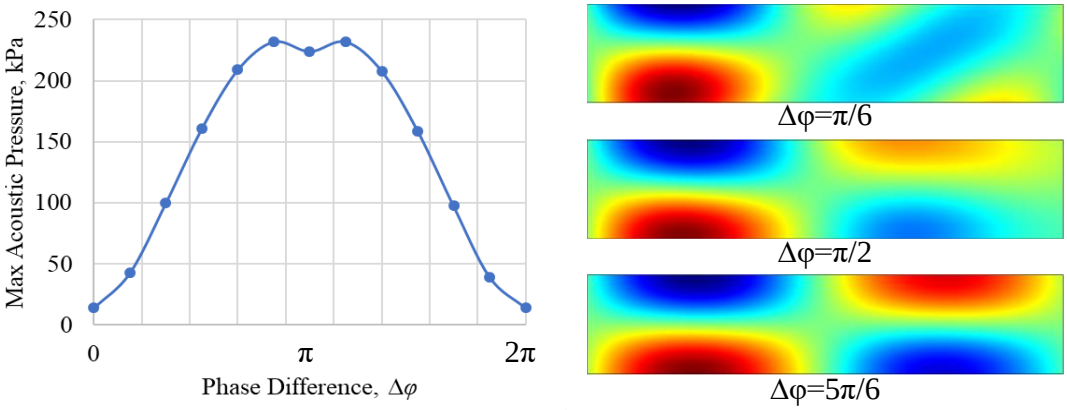

(a) (b)

Fig. 6.5 Plots of the maximum first-order acoustic pressure $\boldsymbol{p_1}$ (a) and the acoustic pressure distribution (b) for phase difference $\Delta\varphi$ between 0 and 2π in the SAW-SAW configuration.

C. Acoustofluidic field and particle trajectories in PZT-SAW channel

The configuration of the hybrid device is shown in **Fig. 4.2c**. Compared with the SAW-SAW configuration, the acoustic pressure in the PZT-SAW channel is higher than that with $\Delta\varphi = 0$, but less than the pressure with $\Delta\varphi = \pi$ (see **Fig. 6.4** and **Fig. 6.6a**). To allow high throughput

particle manipulation by the primary acoustic radiation force to drive particles towards a belt-like distribution in the z direction,[83] it is desired to have two pressure anti-nodes aligned vertically in the channel. I found that it could be achieved by increasing the vibration amplitude of the PZT transducer, e.g., $u_T = 10u_0$. In this case, two pressure anti-nodes were formed (see **Fig. 6.6b**), and the acoustic pressure is higher than that in the SAW-SAW configuration, allowing more power for particle manipulation.

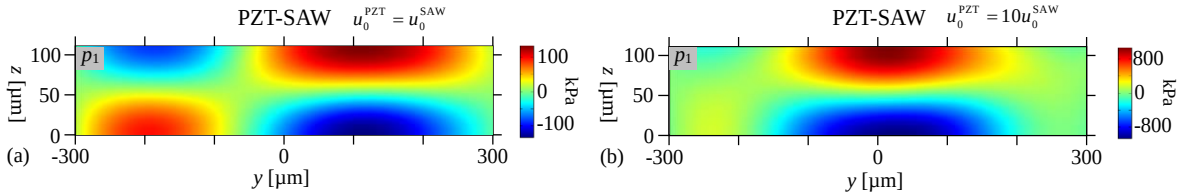

Fig. 6.6 Colour plots of the first-order acoustic pressure $\boldsymbol{p_1}$ for the PZT-SAW configuration when the amplitude of the vibration of the PZT is (a) the same as the SAW transducer, and (b) 10 times higher than the SAW transducer.

To investigate other acoustic pressure values at various microchannel dimensions in the PZT-SAW configuration, I swept the microchannel width (W) and height (H) from λ/2 to λ, and from λ/8 to λ/4, respectively. The maximum acoustic pressure for each set of W and H is shown in **Fig. 6.7a** for $u_T = u_0$ and **Fig. 6.7b** for $u_T = 10u_0$. The largest acoustic pressure of 434 kPa was noted with pressure anti-nodes reduced to two for $u_T = u_0$, and 4,080 kPa for $u_T = 10u_0$. These results demonstrate that changing the dimension of the microchannel is more effective than increasing u_T (see **Fig. 6.6b**) for driving the particles towards a belt-like distribution. The results have potential applications for rapid alignment of particles in the microchannel.

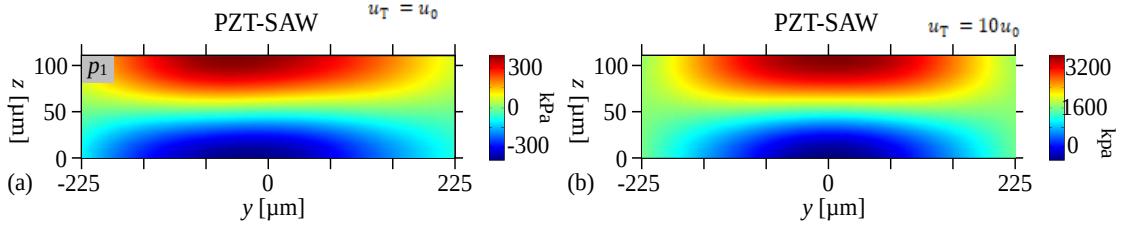

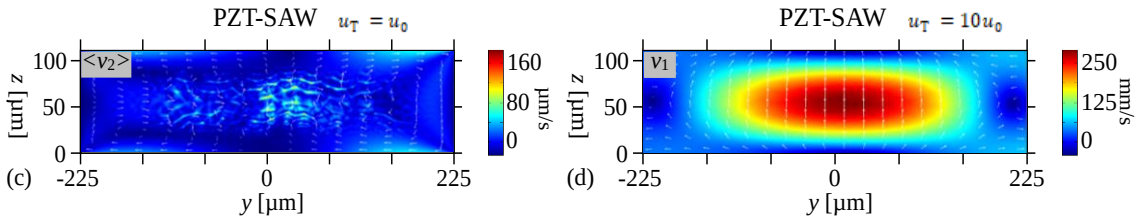

Fig. 6.7 Colour plots of the acoustic pressures for $\boldsymbol{p_1}$ and first-order velocity field $\boldsymbol{v_1}$ for (a)&(c) $\boldsymbol{u_T = u_0}$, (b)&(d) $\boldsymbol{u_T = 10u_0}$. Maximum acoustic pressures were noted at 600 μm (W) × 115 μm (H) and 590 μm (W) × 115 μm (H) for $\boldsymbol{u_T = u_0}$ and $\boldsymbol{u_T = 10u_0}$, respectively.

Fig. 6.8 shows the particle trajectories in the SAW-SAW configuration for $\Delta\varphi = \pi$ and the PZT-SAW configuration for $u_T = 10u_0$. Both configurations struggle to concentrate 1-μm particles due to a lower radiation force vs. drag force ratio. Particles with 5 and 10 μm in diameter are effectively aligned in both the SAW-SAW and the PZT-SAW microchannels. The latter configuration enables a significantly faster transition velocities that are 76 mm/s and 270 mm/s for 5 μm and 10 μm particles, respectively.

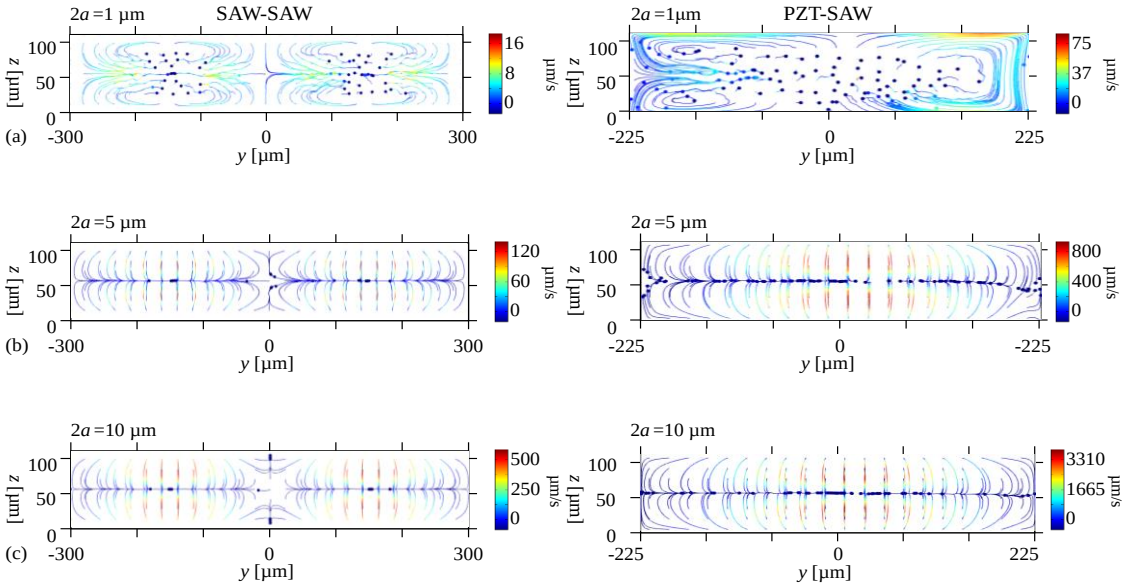

Fig. 6.8 Particle trajectories and velocities in the SAW-SAW (phase difference $\Delta\varphi = \pi$) and PZT-SAW ($\boldsymbol{u_T = 10u_0}$) configurations. (a) Particle size is 1 μm, the maximum velocity is 21.6 μm/s in SAW-SAW and 7.6 mm/s in PZT-SAW. (b) Particle size is 5 μm, the maximum velocity is 155 μm/s in SAW-SAW and 76 mm/s in PZT-SAW. (c) Particle size is 10 μm, the maximum velocity is 582 μm/s in SAW-SAW and 270 mm/s in PZT-SAW.

6.3 GaN-based microfluidic system

Three PNs and two ANs are created inside the microchannel, as illustrated in **Fig. 6.9a**. In **Fig.6.9b**, the equivalent time-averaged second-order velocity $\langle v_2 \rangle$ is depicted with four streaming vortices. The substrate vibration induces this boundary-driven streaming, with the maximum streaming velocity near the bottom substrate (the four high velocity regions at the bottom in **Fig.6.9b**). The resulting gradients in both the x and z directions cause the flowing vortex to move from near to far, as represented by the white arrows in **Fig. 6.9b**. At PNs, streaming goes upward, but at ANs, it flows downward. To study the trajectory of microparticles in the GaN-based microfluidic system, two group of microparticle mixtures, e.g., 15 μm and 5 μm, as well as 15 μm and 1 μm, were simulated, with the results shown in **Fig. 6.9(c–f)**, and **Fig. 6.9(g–j)**, respectively. Both the 15 μm and 5 μm microparticles are dominated by the acoustic radiation force, with the particles traveling towards the nearest PNs. The two transient moments illustrated in **Fig.6.9d** and **Fig.6.9e** demonstrate that the 15 μm microparticles travel faster than the 5 μm microparticles. For instance, large numbers of 5 μm microparticles are still traveling down the channel, whereas the majority of 15 μm microparticles have already reached the PNs in an instant depicted in **Fig.6.9e**. Given enough time, both microparticles can assemble at the PNs as their final destination, as seen in **Fig. 6.9f**. Whereas the mixture of 15 μm and 1 μm microparticles is driven by both the acoustic radiation force and streaming drag force, resulting in a streaming vortex as illustrated in **Fig. 6.9i**, the 15 μm microparticles are already aggregated at the PNs. Additionally, as illustrated in **Fig.6.9j**, simulations results indicate that 1 μm microparticles only follow a streaming pattern to accomplish partial aggregation.

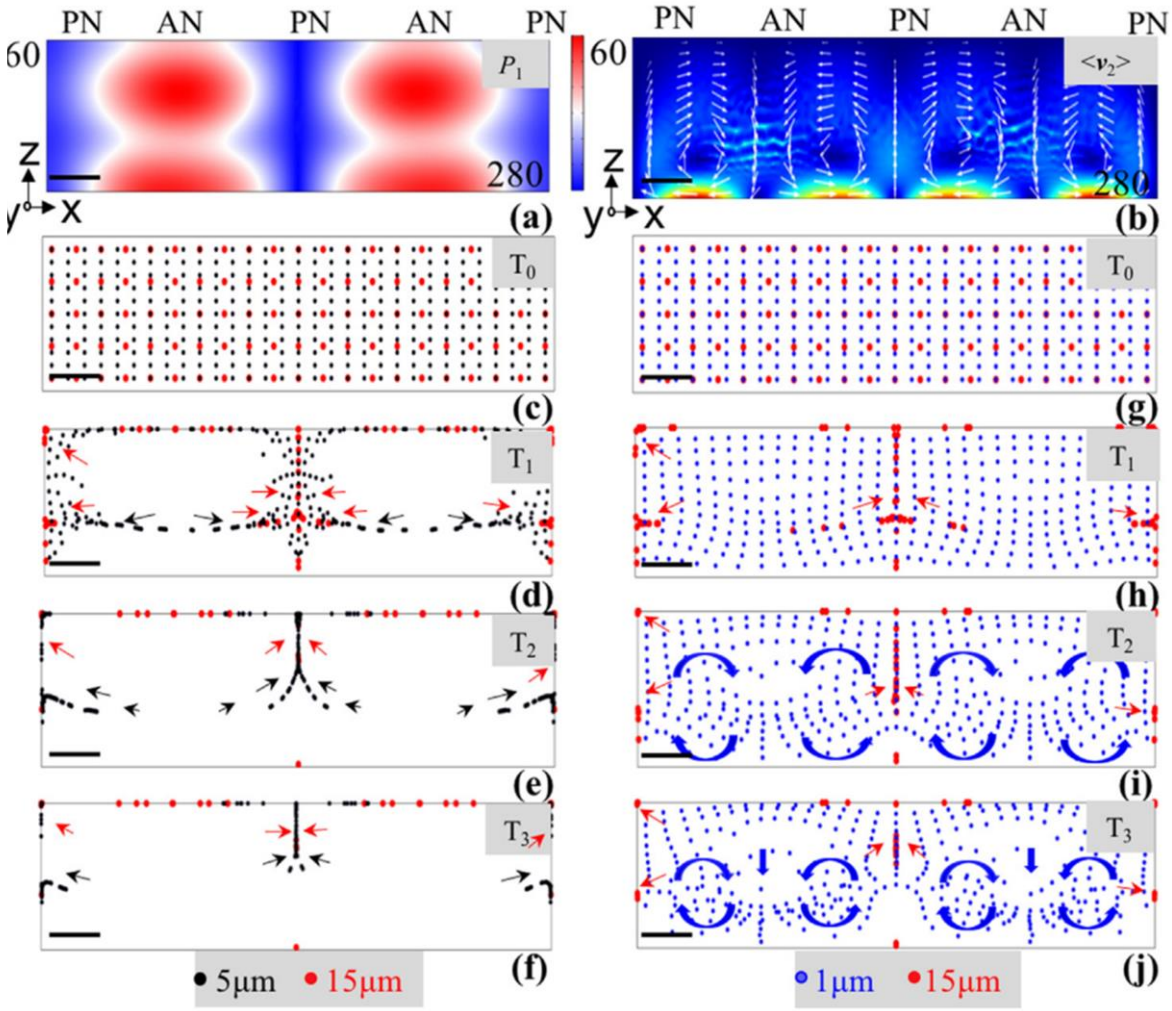

Fig. 6.9 Numerical simulation of the acoustic pressure, time-averaged second-order velocity and microparticles trajectories of GaN-based microfluidic system. (a) The first-order acoustic pressure p1 inside the microchannel. (b) The time-averaged second-order velocity field $<v_2>$. (c–f) The microparticle trajectories of the mixture of 5 μm (black) and 15 μm (red) at a series of time points. (g–j) The microparticle trajectories of the mixture of 1 μm (blue) and 15 μm (red) at a series of points. The scale bar is 20 μm.

Microscope pictures were obtained at 0 s, 5 s, 15 s, and 1 min following the application of SSAWs on a combination of 15 μm and 5 μm polystyrene microspheres (**Fig. 6.10 (a–d)**). 5 μm microspheres move slower towards PNs than 15 μm microspheres. This is illustrated in Fig. 8b, where 15 μm microspheres have already gathered at PNs after 5 s (red arrows). Still, a considerable number of 5 μm microspheres remain spread throughout the microchannel

(black arrows). On 15 s, both sizes of microspheres have accumulated at the PNs, with a significant quantity of 5 μm microspheres still enroute to the PNs (**Fig. 6.10(c)**). The experimental results demonstrate that the acoustic radiation force successfully induce both sizes of particles to move toward PNs. Due to their size disparities, 5 μm and 15 μm suffer acoustic radiation forces of varying magnitudes, resulting in varying movement velocities. The majority of these microspheres create three traces of microspheres at their final positions at 1 minute, demonstrating that acoustic radiation force mostly drives large particles in the GaN-system. The practical results correlate well with the simulated results depicted in **Fig. 6.10(c–f)**. When a mixture of 15 μm and 1 μm microspheres is used (**Fig. 6.10(e–h)**), the majority of the 15 μm microspheres move rapidly to the PNs after 5 s and are well aligned after 15 s. (red arrows). However, 1 μm microspheres exhibit no clear aggregation pattern after 5 s (**Fig.6.10f**), which is consistent with **Fig.6.10h**. After 15 seconds, 1 μm microspheres exhibit a significant streaming impact, forming four streaming vortices as illustrated in **Fig.6.10g** (see blue arrows). It is worth noting that after 1 minute, two traces of 1 μm microspheres form adjacent to the center PNs (**Fig.6.10h**), which is consistent with the simulation presented in **Fig.6.10j**. The final position varying from the different sizes of microspheres suggests that the simulation model is reliable with different piezoelectric substrate.

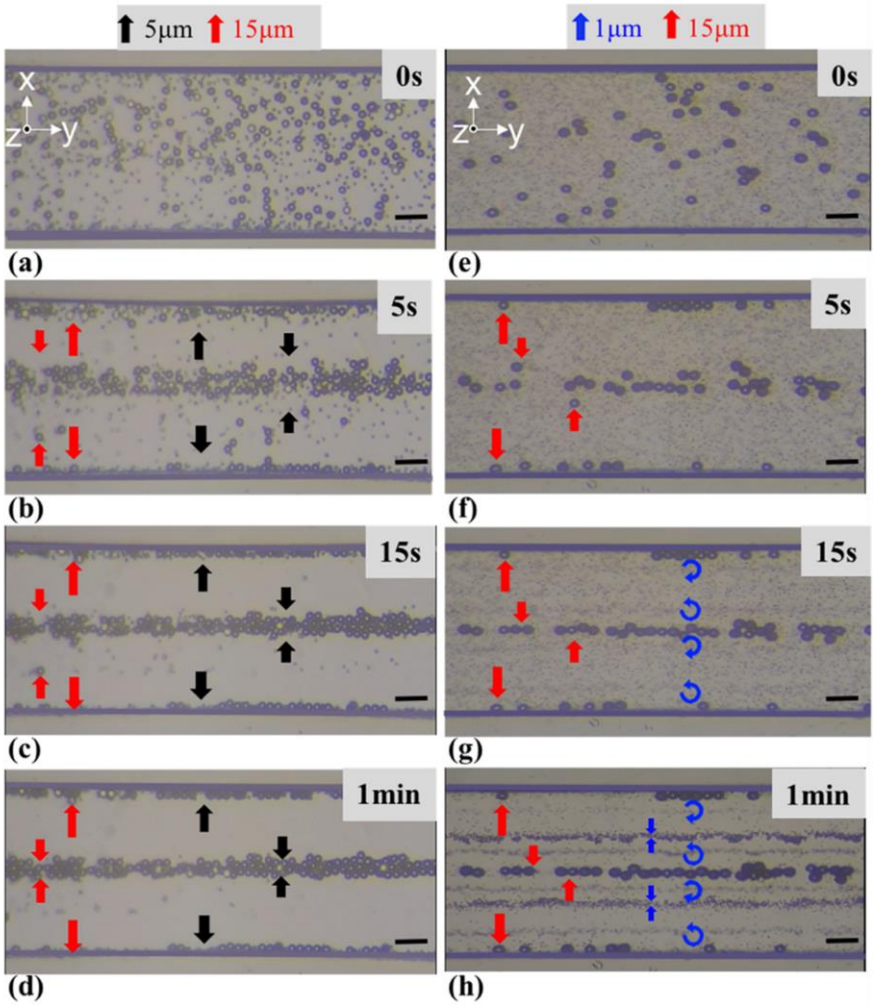

Fig. 6.10 Experimental results of the mixture of 5 μm and 15 μm polystyrene microspheres and the mixture of 1 μm and 15 μm polystyrene microspheres. (a–d) The distribution of 5 μm and 15 μm microspheres driven by the SSAW field within the microchannel between 0 s and 1 min. (e-h) The distribution of 1 μm and 15 μm microspheres driven by the SSAW field within the microchannel between 0 s and 1 min. The scale bar is 50 μm.

6.4 Cell mechanophenotyping result

6.4.1 numerical result

Cells focused by two sheath flows are flowing into the channel and subsequently actuated by the acoustic radiation force (F_r) towards the PN lines. The cell trajectory depends on the mechanical property of the cell, the condition of the medium, and the device's configuration.

The device was sat on an inverted microscope with a camera to record the trajectory of the cells / microparticles (**Fig. 6.11c**)

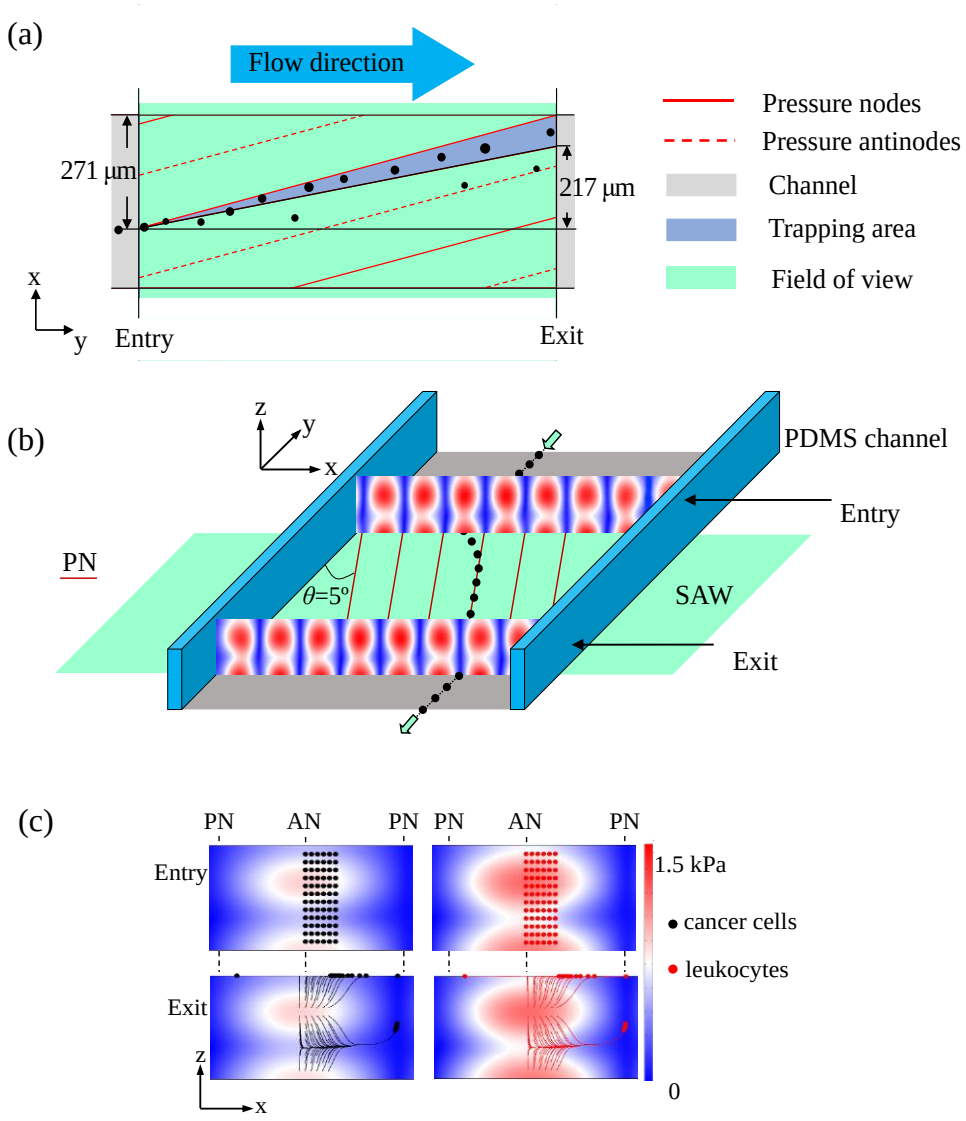

Fig. 6.11 (a) Under the threshold input power, 80% of cells are convergent to the lateral position (x-axis) between 217 µm and 270 µm when leaving the field of view. (b) Acoustic pressure distribution at the entry and exist (colours indicate the magnitude of acoustic pressure, from 0 kPa (blue) to 1.5 kPa (red)). (c) Two cell types (leukocytes and cancer cells) follow the same converging trajectory under different input powers, represented by acoustic pressures.

Before measuring cancer cells and leukocytes, commercially sourced PS microspheres were used to establish the reference trajectory and validate the accuracy of method for obtaining the acoustic contrast factor. Firstly, 10 µm PS (72986, Sigma-Aldrich) microspheres were chosen

to generate the reference trajectory by tuning the input power from 20 dBm to 30 dBm. Then, the acoustic contrast factor of 5 μm (79633, Sigma-Aldrich) and 15 μm PS microsphere (74964, Sigma-Aldrich) was obtained independently to benchmark with the nominated value.

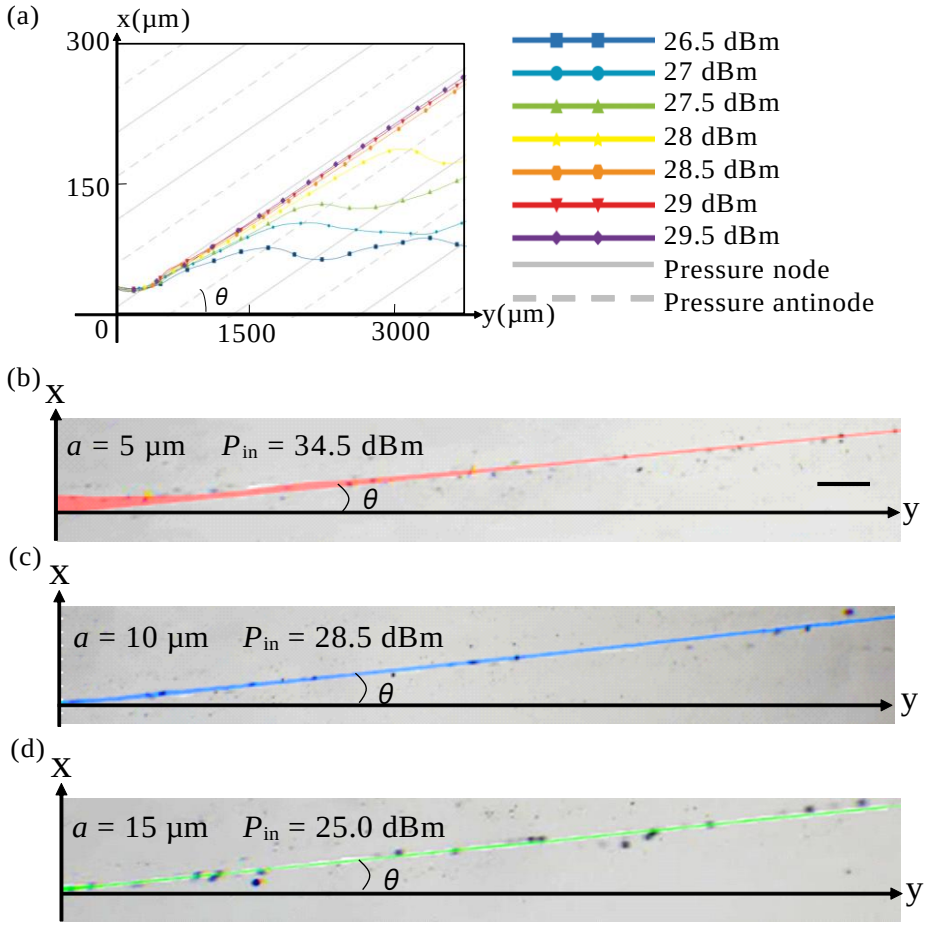

Fig. 6.12 (a) Plot of numerical trajectories for 10 μm PS microspheres with increment of the input power. Convergence to the first nearest PN line presents once the threshold input power is met. (b)-(d)Optical images show the experimental trajectories of PS microspheres converging to the first nearest PN line. The blue, red, and green bands are simulation trajectories under the respective input power. (Scale bars, 200 μm)

To test the feasibility of using the acoustic contrast factor to mechanophenotype cells, adenocarcinoma human alveolar basal epithelial cells (A549), triple-negative breast cancer cells (MDA-MB-231), and leukocytes were tested separately in the FTA device. The entering position of the field of view of the microscope was located at the beginning of the acoustic field, where the cells started to deflect. To determine the threshold input power, the lateral displacement of the cell was recorded while tuning the input power until most of the cells are

converged to the PN line. Considering there was a deviation (similar with the particle deviation in simulation results shown in **Fig. 6.12**) before cells were converged to the PN line, the cells that displaced over 80% of the maximum lateral displacement (~ 271 μm) regarded were to be convergent to the PN line, as shown in **Fig. 6.11a**.

6.4.2 Simulation and reference trajectory

Fig. 6.11b shows the obtained acoustic pressure distribution inside the channel along the y-axis. On the x-z plane, stable PNs and ANs are generated and orderly arranged along the channel with an equal shift of the PNs and ANs due to the inclination angle between the IDT and channel. The microparticles enter the SAW region which consists of a series of ANs (blue area in the simulation) and PNs (red area in the simulation). One can adjust the acoustic pressure intensity by varying the RF input power (represented by the intensity of acoustic pressure) to drive two types of cells, e.g., leukocytes and cancer cells, to converge to the PN following a similar trajectory, as shown in **Fig. 6.11c**. The converging trajectory can be achieved by tuning only the RF input power disregarding the properties of these microparticles (volume, compressibility, and density). One can achieve the same time for converging leukocytes and cancer cells to the PNs under different acoustic pressures of 1.2 kPa and 0.7 kPa, respectively. The COMSOL simulation results prove the feasibility of adjusting the acoustic pressure (determined by the RF input power) to enable the convergence of various cells to the PNs.

On the x-y plane, the lateral movements of given microparticles, e.g., 10 μm PS microspheres, under different input powers ranging from 26.5 dBm to 29.5 dBm is illustrated in **Fig. 6.12**. There exists a threshold input power, 28.5 dBm for 10 μm PS microspheres, which drives the microparticle trajectory to quickly converge to the nearest PN line (solid grey lines) and shift upwards along the PN line. I investigated various particle parameters and found the same trend where cells would be convergent to the first nearest PN line soon after entering the acoustic region when the RF input power was higher than a threshold, while the cell would escape from the first nearest PN line when the input power was smaller than this threshold.

For the ease of observation and judgement, I define the trajectory, which firstly becomes convergent to the first nearest PN line, as the reference trajectory. Considering that the microparticles follow a curved path before being convergent to the PN line, the threshold input power is determined when 75% of microparticles are convergent to the PN. In this article, I use the trajectory of the 10 μm PS microspheres under 28.5 dBm as the reference trajectory, and the reference product $A_1\varphi_1$ is 0.0018. The experimentally obtained reference trajectory is shown in **Fig. 6.12(b)-(d)**, in which the 10 μm PS microspheres follow the theoretical trajectory (blue band). As described in the previous section, the same trajectory corresponds to the same product of A and φ. Therefore, the acoustic contrast factor of any unknown microparticle/cells can be obtained once I observe the threshold input power and the size.

6.4.3 Acoustic contrast factor measurement of microspheres

To validate the accuracy of using this method to calculate the acoustic contrast factor, PS microspheres of 5 μm and 15 μm were tested. The trajectories of the 5 μm and 15 μm PS microspheres firstly conformed to the reference trajectory, being converged to the PN soon after entering the acoustic region, at 34.5 dBm and 25.0 dBm, respectively as shown in Figs. 7.13(b&c), where the red and green bands are the numerical simulation trajectories for the two microspheres, respectively. According to Equation (10), the measured acoustic contrast factor for 5 μm and 15 μm PS microspheres are 0.1985 and 0.1966, respectively, which are 2.37% and 1.39% different from the derived value of 0.1939.[135] The slight error may be due to the size deviation of PS microspheres (5 ± 0.1 μm and 15 ± 0.2 μm). This result that an accuracy of more than 97.36% suggests that the proposed method for mechanophenotyping is reliable.

6.4.4 Measurement of cells area and threshold input powers

As shown in **Fig. 6.14a**, the A549 cells are generally larger than MDA-MB-231 cells, and both types of cancer cells are much larger than leukocytes. The size distribution of leukocytes is more compact than both A549 and MDA-MB-231, which confirms the high heterogeneity of tumour cells.[136]

As the input power increases, the various degrees of cell deflection from the original course are shown in **Fig. 6.14(b-d)**. Once the threshold input power is applied, the cells are converged to the PN line with an inclination angle of $\theta = 5^{o}$ to the channel wall. The larger A549 cells start to deflect subject to the input power of 30 dBm (**Fig. 6.14(b.1)**) whereas the MDA-MB-231 and leukocytes almost remain on their original paths (**Figs. 6.14(b.2)** & **6.14(b.3)**). Increasing the input power to 31 dBm enables the A549 to converge to the PN line (**Fig. 6.14(c.1)**), which also slightly deflects the MDA-MB-231 (Fig. 6.14(c.2)) towards the PN line. The leukocytes keep the baseline trajectory with the input power of 31 dBm or 32 dBm (**Figs.6.14 (c.3&d.3)**), which indicates that a higher threshold input power is required for leukocytes to converge to the PN line. Both the MDA-MB-231 and A549 cells acquire sufficient momentum and are finally converged to the PN line under 32 dBm (**Figs. 6.14(d.1 &d.2)**). The heterogeneity of cancer cells results in intercellular variability in deflection but the wavy trajectories towards the PN line as denoted in **Fig. 6.14(c.2)** are in line with the simulation when the input power is below the threshold power (**Fig. 6.12**).

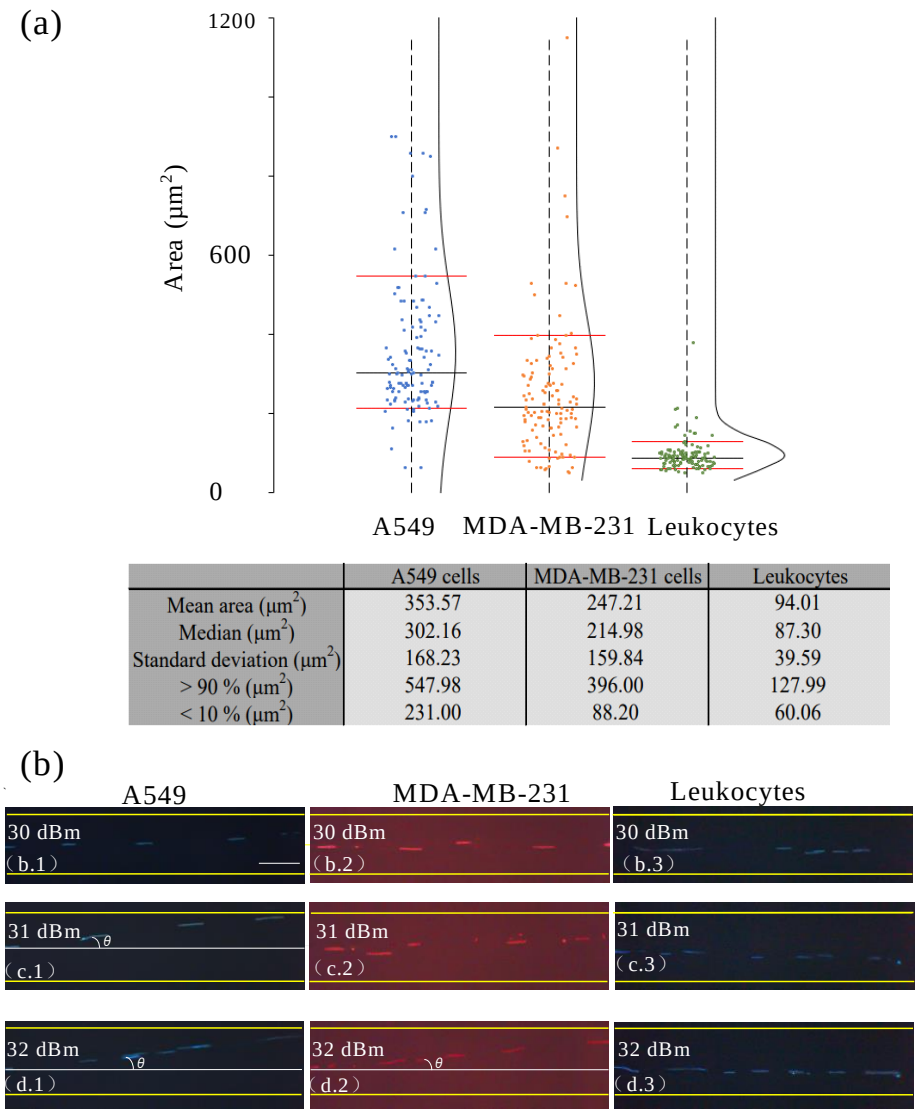

	A549 cells	MDA-MB-231 cells	Leukocytes
Mean area (μm²)	353.57	247.21	94.01
Median (μm²)	302.16	214.98	87.30
Standard deviation (μm²)	168.23	159.84	39.59
> 90 % (μm²)	547.98	396.00	127.99
< 10 % (μm²)	231.00	88.20	60.06

Fig. 6.14 Size distribution and experimental trajectories of A549, MDA-MB-231, and leukocytes. (a) Size distribution of the three cell types. Red horizontal lines show the 10th and 90th percentiles, black horizontal lines show the median value, black curves show the distribution (n = 120). The table show the area measurement results of the A549, MDA-MB-231 cells, and leukocytes. (b)-(d) Fluorescence imaging of the three cell types translating through the channel under the input power of 30 dBm, 31 dBm, and 32 dBm. (Scale bars, 500 μm) The images show that two cancer cells finally converge to the PN line in which 'θ' is annotated. Leukocytes remain close to their original course without notable deflection towards the PN line.

Since the mechanical property of any one type of cells is not uniform, the movement of cells

is not the same and thus does not manifest as a single line of trace during the experimental process. Our results reveal that there exists the trajectory of a cell subset convergent to the PN line at low input powers, while another cell subset shows less or no visible deflection under the same conditions. In order to more accurately assess whether the cell deflection approximates to the reference trajectory, I recorded the changes in x coordinate that occurred as the cell entered and exited the field of view and then calculated the lateral displacements. With the increase of the RF input power, the lateral displacement of the three different cells gradually converged to around 271 μm. For A549 cells shown in **Fig. 6.15a**, as the input power was increased from 29 dBm to 31 dBm, the 75th percentiles (red bars in the figure) were fixed at around 270 μm, and the 25th percentiles increased from 97.5 μm to 237.5 μm. For MDA-MB-231 cells (**Fig. 6.15b**), the 75th percentiles gradually increased from 250 μm to 320 μm and the 25th percentiles increased from 70 μm to 260 μm as the input power increased from 30 dBm to 32 dBm. A similar trend was observed for leukocytes (**Fig.6.15c**), as the input power increased from 32 dBm to 34 dBm. Finally, the cell traces comply with the reference trajectory with the input powers of 31 dBm, 32 dBm, and 34 dBm for A549, MDA-MB-231 and leukocytes, respectively, which are defined as the threshold input powers of the three types of cells. The reason of exceeding the maximum theoretical lateral displacement is probably because, as the input power increases, the cells are also subject to focusing on the z direction (**Fig.6.15c**), which may cause some of the cells to attach to the channel top and change the local acoustofluidic field.

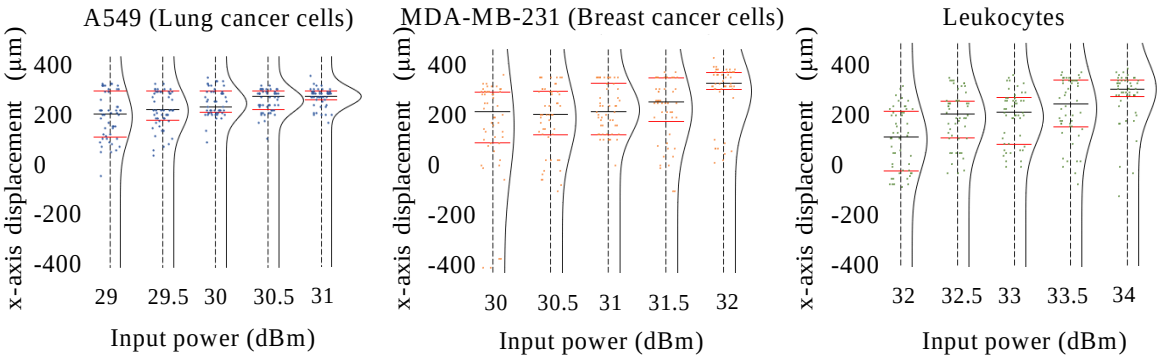

(a) (b) (c)

Fig. 6.15 Distribution plots of cells under different input powers. (a) A549, (b) MDA-MB-231, and (c) leukocytes show convergence to the PN line under 31 dBm, 32 dBm, and 34 dBm, respectively. Top and bottom red horizontal bars show the 25th and 75th percentiles, respectively. Black horizontal bars show the median value, black curves show the distribution (n = 150).

6.4.5 Calculation of the acoustic contrast factor

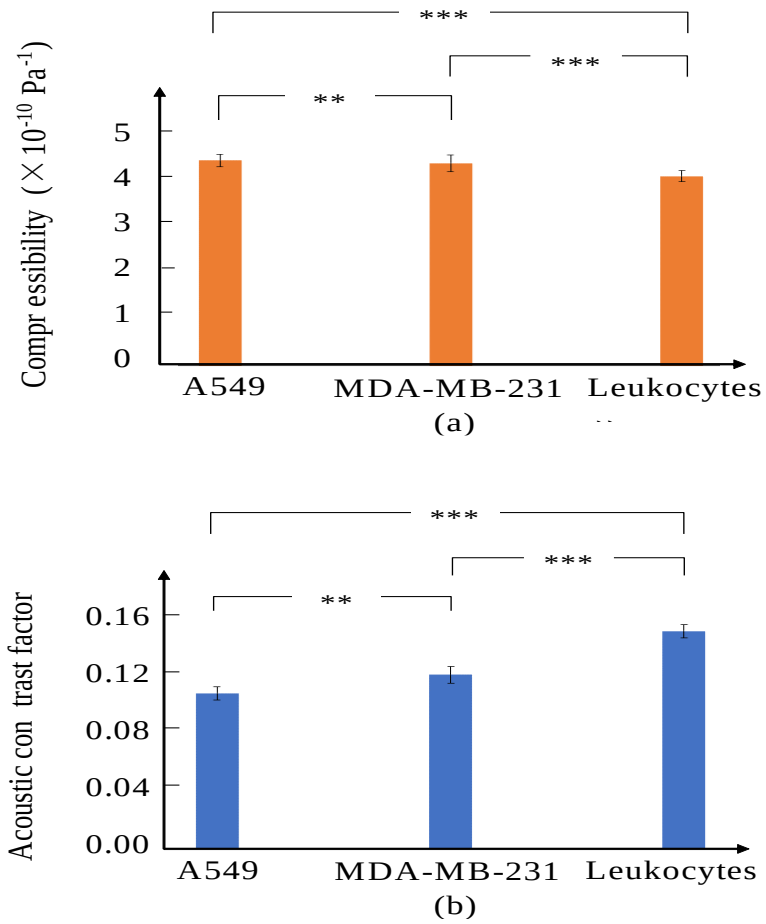

Fig .6.16 The compressibility (a) and acoustic contrast factor (b) of A549, MDA-MB-231, and leukocytes. *** and ** indicate $p<0.001$ and $p<0.01$, respectively.

After obtaining the deflection threshold of input powers and cell areas, the acoustic contrast factors of three types of cells were calculated using Eqn (11), and their compressibility were calculated by assuming the density of the cells (Leukocytes: 1,019±3 kgm^{-3}, tumour cells: 1,051±3 kgm^{-3}).[99, 137, 138] As shown in **Fig. 6.16**, leukocytes have the greatest acoustic contrast

of 0.147, which may be the result of their smaller compressibility and relatively smaller density. The acoustic contrast factors of A549 cells and MDA-MB-231 cells are 0.106 and 0.115. The difference in the acoustic contrast factors between cancer cells (A549 and MDA-MB-231) and leukocytes are found to be 27.9% and 21.5%, respectively. However, the corresponding difference in compressibility of these two groups is 8.0% and 6.7%, respectively. The compressibility of the three cell types is $4.35 \pm 0.01\times10^{-10}$ Pa^{-1} (A549), $4.30 \pm 0.01 \times10^{-10}$ Pa^{-1}(MDA-MB-231), $4.02 \pm 0.01\times10^{-10}$ Pa^{-1} (leukocytes). The difference in the acoustic contrast factors and compressibility between the two cancer cell types (A549 and MDA-MB-231) are found to be 8.2% and 1.2%, respectively. This result suggests that acoustic contrast factor could be a sensitive parameter for mechanophenotyping compared to compressibility. This difference in acoustic contrast factor may arise from the fact that cancer cells are known to be more compressible than normal cells [139] and the invasive cancer cells are stiffer than normal cells.[140] For A549 and MDA-MB-231 cells, even though their cell sizes have some overlap, there was still a 8.2 % difference in acoustic contrast factor, suggesting a clear difference in the mechanical properties of these similarly sized cancer cells. I speculate that the smaller acoustic contrast factor of A549 may be related to their higher invasive capacity, as cells require higher compressibility to migrate through the extracellular matrix and move within the original tissue.[141] [100] The results demonstrate that the acoustic contrast factor can be used as a useful parameter to distinguish and mechanophenotype these three cell types.

Furthermore, once the acoustic contrast factor is known, the trend of cell movement in the acoustofluidic channel could be determined. From an engineering point of view, the need for tracking cells through image processing is greatly simplified. Our method replaces the trajectory fitting in measuring compressibility (such as Ref. [94, 142, 143]) by registering the input power when the cells converge to the reference trajectory. Compared with the multi-tilted-angle surface acoustic wave compressibility cytometry,[99] our method eliminates the need for fabricating the channel with multiple titled walls and saves the cells from impacting on the channel walls. After establishing the reference trajectory, the threshold of the input power can be used to derive the

acoustic contract factor and compressibility. This offers a robust solution for label-free acoustofluidic cytometry eliminating the need of the complex optical system. As an enhanced acoustofluidic chip, the ETA device offers great versatility and dual capability in both separation[144] and mechanophenotyping different types of cells. This will be valuable for identifying and characterising tumour cells without the need of molecular labelling. Given that the complex biological processes behind these phenotypes can manifest as changes in cell structure, I also expect mechanical phenotyping can be an important, rapid and unbiased-single-cell analytical tool to advance our understanding of biological processes.

Frequency is one of the key device parameters when determining the design of the ETA device. Given the square of the particle critical size is inversely proportional to the working frequency,[145] the working frequency of 19.632 MHz in this work results in a critical size of 4 μm, which is considerably smaller than most of the cell types in the experiment. Further increasing the working frequency to 30-40 MHz allows the ETA device to effectively mechanically phenotype smaller cells, e.g., erythrocytes (4-10 μm)[146] and platelets (1-2 μm)[147]. Submicrometer particles have been successfully manipulated and sorted by using a combined electric and acoustic field[148], which embraces both dielectrophoretic and acoustophoretic forces to lower the critical diameter. The combination overcomes the general problem in sole acoustophoresis including that higher frequency causes larger acoustic attenuation in water[149] and stronger streaming effect[150]. The channel dimensions used in the present work can be further optimised to reduce the cell/microparticle aggregation on the top of the channel caused by the vertical focusing. Though reducing the channel height results in less vertical focusing nodes and acoustic attenuation, it can potentially jam the passing cells and block the entire device. The height of 60 μm is recommended by the simulation[151] and friendly for the cell passage.

Given the ETA device configuration is exquisite in both separation and

mechanophenotyping, the future work will integrate acoustic measurement of mechanical properties of cells and acoustic sorting for ultimately constructing a mechanophenotyping-activated cell sorting.

Chapter 7 Conclusion and Future work

7.1 Conclusion

From a simulation perspective, an SSAW microfluidic model is developed to study the acoustic pressure distribution and particle trajectories in SSAW-based microfluidic devices. This model considers the SSAW drive and appropriate boundary conditions to simulate the acoustic propagation through the channel walls. By comparing numerical and published numerical results, I find that the predictions of the two-dimensional SSAW microfluidic model match well with the published results, which indicates the accuracy of the model. Also, I used this model conventional SAW-PDMS, hybrid SAW-glass, new SAW-SAW and PZT-SAW structures were synthesized for comparison. The model with the SAW-SAW sensor significantly increases the velocity of 10 μm particles to 582 μm/sec, compared to 41 μm/sec for the state-of-the-art hybrid SAW-glass configuration. This increase is due to the active acoustic waves generated by the top SAW sensor, as opposed to the passive reflected acoustic waves of the bottom SAW sensor used in most acoustic fluid devices. In addition, it is shown that the longitudinal waves generated by the top PZT actuator in the PZT-SAW model can interact with the acoustic waves generated by the bottom SAW transducer, resulting in stronger acoustic resonance in the microchannel. As a result, the velocity of the particles can be three orders of magnitude higher than that in the SAW-SAW configuration. This provides a good theoretical basis for the update of the particle manipulation system.

From an experimental point of view, the GaN system and the FTA system were developed to manipulate particles with cell mechanophenotyping, respectively. When operating at high input power, the GaN system expressed good thermal stability. The thermal performance can be further improved by using silicon as a substrate, which will also provide compatibility with high-volume, high-volume and low-cost semiconductor fabrication to significantly reduce the cost of these devices. Experimental results using both microparticle and cell manipulation validate the numerical simulation results of the GaN system, demonstrating the accuracy and generalizability of the SAW theoretical model from an experimental perspective.

Acoustophoresis implemented by GaNAT will open the field of exploring multiple physical applications of GaN for monolithic integration with electronics, development of biosensors and MEMS devices were developed to measure the mechanical properties of cells. The input threshold power is determined by observing the proximity of the measured cell trajectory to a reference trajectory established using 10 μm PS microspheres. The acoustic contrast factor, which reflects the compressibility and density of the target cells, is calculated using the threshold power. In validation with PS microspheres, the accuracy of the measurements was greater than 97.63%. acoustic contrast coefficients for A549, MDA-MB-231, and leukocytes were 0.120, 0.158, and 0.102, respectively. this technique provides the opportunity to transfer molecular specificity to label-free cell characterization. Acoustic flow cytometry is expected to be widely used for basic research and biomedical applications, and its immediate utility includes high-throughput differentiation of tumor cell types.

7.2 Future work

The thesis has fundamentally investigated SAW-based acoustofluidic bio-particles manipulation and studied the basic physics involved with this technology using classic theory, numerical simulations, and experiments. However, the work done here is still quite basic and more space in this field can be explored to further extend the functionalities and applications of the technology.

1. I used COMSOL to build the simulation models with finite element method and the surface wave vibrations were simulated with displacement boundary conditions. Although the results obtained were in general agreement with published and experimental results, the whole simulation did not reflect the electromechanical coupling process of the signal from the electrodes to the piezoelectric substrate. A more complex and comprehensive simulation model should be built in the future, which needs to reflect both the piezoelectric dynamics of the SSAW acoustic fluid device and the surrounding elastic solid domain of the microfluid.
2. I also develop a PZT-SAW configuration from a numerical computational perspective, which proves to have theoretically higher acoustic pressure and particle velocity, and based on

the guidance of the simulation results, a new PZT-SAW system should be fabricated in the future to achieve high throughput particle manipulation.

3. I note that three-dimensional simulations of acoustofluidic devices are now rarely mentioned, and that the development of three-dimensional models is important for further studies of acoustofluidic manipulation, which would involve more interfaces and transverse wave diffraction. Three-dimensional simulations are useful for revealing and designing systems with innovative acoustofluidic systems.

4. Many challenges remain in particle manipulation, such as precisely manipulating individual cells without affecting neighboring cells.

5. Much future work needs to be done to continually understand and develop the physical theory of acoustic fields and acoustic streaming flow and develop methods to manipulate individual pressure nodes and individual cells independently.

6. Acoustic hydrodynamics can be combined with other ways, such as magnetics and optics, to thoroughly investigate the complexity of cells and their associated studies.

Bibliography

1. G. D. Chen, F. Fachin, M. Fernandez-Suarez, B. L. Wardle and M. Toner, *Small*, 2011, **7**, 1061-1067.
2. P. Li, Z. Mao, Z. Peng, L. Zhou, Y. Chen, P.-H. Huang, C. I. Truica, J. J. Drabick, W. S. El-Deiry, M. Dao, S. Suresh and T. J. Huang, *Proc Natl Acad Sci U S A*, 2015, **112**, 4970.
3. L. R. Huang, E. C. Cox, R. H. Austin and J. C. Sturm, *Science*, 2004, **304**, 987-990.
4. B. H. Wunsch, J. T. Smith, S. M. Gifford, C. Wang, M. Brink, R. L. Bruce, R. H. Austin, G. Stolovitzky and Y. Astier, *Nat Nanotechnol*, 2016, **11**, 936-940.
5. S. Choi and J. K. Park, *Lab Chip*, 2007, **7**, 890-897.
6. S. Choi, S. Song, C. Choi and J. K. Park, *Small*, 2008, **4**, 634-641.
7. S. Choi and J. K. Park, *Anal Chem*, 2008, **80**, 3035-3039.
8. J. Takagi, M. Yamada, M. Yasuda and M. Seki, *Lab Chip*, 2005, **5**, 778-784.
9. R. G. Larson, *Journal of Rheology*, 2005, **49**, 1-70.
10. Y.-W. Lin, T.-C. Chiu and H.-T. Chang, *Journal of Chromatography B*, 2003, **793**, 37-48.
11. X. Xuan and D. Li, *Electrophoresis*, 2005, **26**, 3552-3560.
12. D. S. Reichmuth, S. K. Wang, L. M. Barrett, D. J. Throckmorton, W. Einfeld and A. K. Singh, *Lab on a Chip*, 2008, **8**, 1319-1324.
13. D. F. Chen, H. Du and W. H. Li, *Sensors and Actuators A: Physical*, 2007, **133**, 329-334.
14. L. Wang, L. A. Flanagan, N. L. Jeon, E. Monuki and A. P. Lee, *Lab on a Chip*, 2007, **7**, 1114-1120.
15. B. Çetin and D. Li, *ELECTROPHORESIS*, 2011, **32**, 2410-2427.
16. B. Cetin and D. Li, *ELECTROPHORESIS*, 2008, **29**, 994-1005.
17. S. Yaman, M. Anil-Inevi, E. Ozcivici and H. C. Tekin, *Frontiers in Bioengineering and Biotechnology*, 2018, **6**.
18. M. Hejazian and N.-T. Nguyen, *Biomicrofluidics*, 2016, **10**, 044103.
19. B. D. Plouffe, M. Mahalanabis, L. H. Lewis, C. M. Klapperich and S. K. Murthy, *Analytical chemistry*, 2012, **84**, 1336-1344.
20. L. Zeng, L. Qiu, X. T. Yang, Y. H. Zhou, J. Du, H. Y. Wang, J. H. Sun, C. Yang and J. X. Jiang, *Cell Biol Int*, 2015, **39**, 1348-1353.
21. R.-Z. Lin and H.-Y. Chang, *Biotechnology Journal*, 2008, **3**, 1172-1184.
22. S. Ghosh, S. Kumar, I. Puri and S. Elankumaran, *Cell proliferation*, 2016, **49**, 134-144.
23. G. R. Souza, J. R. Molina, R. M. Raphael, M. G. Ozawa, D. J. Stark, C. S. Levin, L. F. Bronk, J. S. Ananta, J. Mandelin and M.-M. Georgescu, *Nature nanotechnology*, 2010, **5**, 291-296.
24. C.-Y. Lin, P.-L. Wei, W.-J. Chang, Y.-K. Huang, S.-W. Feng, C.-T. Lin, S.-Y. Lee and H.-M. Huang, *PLoS One*, 2013, **8**, e58988.
25. A. Chionna, B. Tenuzzo, E. Panzarini, M. B. Dwikat, L. Abbro and L. Dini, *Bioelectromagnetics: Journal of the Bioelectromagnetics Society, The Society for*

Physical Regulation in Biology and Medicine, The European Bioelectromagnetics Association, 2005, **26**, 275-286.
26. A. Ashkin, J. M. Dziedzic, J. E. Bjorkholm and S. Chu, *Opt. Lett.*, 1986, **11**, 288-290.
27. A. Ashkin, *IEEE Journal of Selected Topics in Quantum Electronics*, 2000, **6**, 841-856.
28. K. Svoboda and S. M. Block, *Opt. Lett.*, 1994, **19**, 930-932.
29. P. C. Ke and M. Gu, *Appl Opt*, 1999, **38**, 160-167.
30. G. Pesce, P. H. Jones, O. M. Maragò and G. Volpe, *The European Physical Journal Plus*, 2020, **135**, 1-38.
31. Y. Liu and P. H. Daum, *Journal of Aerosol Science*, 2000, **31**, 945-957.
32. Y. Wu, D. Sun and W. Huang, *Journal of biomechanics*, 2011, **44**, 741-746.
33. F. Arai, A. Ichikawa, M. Ogawa, T. Fukuda, K. Horio and K. Itoigawa, *Electrophoresis*, 2001, **22**, 283-288.
34. S. C. Chapin, V. Germain and E. R. Dufresne, *Optics express*, 2006, **14**, 13095-13100.
35. E. Eriksson, J. Enger, B. Nordlander, N. Erjavec, K. Ramser, M. Goksör, S. Hohmann, T. Nyström and D. Hanstorp, *Lab on a Chip*, 2007, **7**, 71-76.
36. X. Wang, S. Chen, M. Kong, Z. Wang, K. D. Costa, R. A. Li and D. Sun, *Lab on a Chip*, 2011, **11**, 3656-3662.
37. Y. Li, Z. Guo and S. Qu, *Optics and Lasers in Engineering*, 2014, **55**, 150-154.
38. J. Leach, H. Mushfique, R. di Leonardo, M. Padgett and J. Cooper, *Lab Chip*, 2006, **6**, 735-739.
39. A. Terray, J. Oakey and D. W. Marr, *Science*, 2002, **296**, 1841-1844.
40. S. Keen, A. Yao, J. Leach, R. Di Leonardo, C. Saunter, G. Love, J. Cooper and M. Padgett, *Lab Chip*, 2009, **9**, 2059-2062.
41. T. Gorishnyy, M. Maldovan, C. Ullal and E. Thomas, *Physics world*, 2005, **18**, 24.
42. I. Leibacher, P. Reichert and J. Dual, *Lab Chip*, 2015, **15**, 2896-2905.
43. M. Wu, A. Ozcelik, J. Rufo, Z. Wang, R. Fang and T. Jun Huang, *Microsyst Nanoeng*, 2019, **5**, 32.
44. G. Destgeer and H. J. Sung, *Lab Chip*, 2015, **15**, 2722-2738.
45. M. Tayebi, R. O'Rorke, H. C. Wong, H. Y. Low, J. Han, D. J. Collins and Y. Ai, *Small*, 2020, **16**, 2000462.
46. K. C. Neuman and A. Nagy, *Nature methods*, 2008, **5**, 491-505.
47. P. Li and T. J. Huang, *Analytical chemistry*, 2018, **91**, 757-767.
48. A. Kundt, *Annalen der Physik*, 1866, **203**, 497-523.
49. M. Evander and J. Nilsson, *Lab Chip*, 2012, **12**, 4667-4676.
50. O. Jakobsson, S. S. Oh, M. Antfolk, M. Eisenstein, T. Laurell and H. T. Soh, *Analytical Chemistry*, 2015, **87**, 8497-8502.
51. Z. Mao, P. Li, M. Wu, H. Bachman, N. Mesyngier, X. Guo, S. Liu, F. Costanzo and T. J. Huang, *ACS Nano*, 2017, **11**, 603-612.
52. B. Hammarström, T. Laurell and J. Nilsson, *Lab Chip*, 2012, **12**, 4296-4304.
53. P. Ohlsson, M. Evander, K. Petersson, L. Mellhammar, A. Lehmusvuori, U. Karhunen, M. Soikkeli, T. Seppä, E. Tuunainen, A. Spangar, P. von Lode, K.

Rantakokko-Jalava, G. Otto, S. Scheding, T. Soukka, S. Wittfooth and T. Laurell, *Analytical Chemistry*, 2016, **88**, 9403-9411.
54. J. M. Cooper, P. B. Wiklander, J. Z. Nordin, R. Al-Shawi, M. J. Wood, M. Vithlani, A. H. Schapira, J. P. Simons, S. El-Andaloussi and L. Alvarez-Erviti, *Mov Disord*, 2014, **29**, 1476-1485.
55. A. Ku, H. C. Lim, M. Evander, H. Lilja, T. Laurell, S. Scheding and Y. Ceder, *Analytical Chemistry*, 2018, **90**, 8011-8019.
56. Y. Gu, C. Chen, Z. Mao, H. Bachman, R. Becker, J. Rufo, Z. Wang, P. Zhang, J. Mai and S. Yang, *Science Advances*, 2021, **7**, eabc0467.
57. S. Li, L. Ren, P.-H. Huang, X. Yao, R. A. Cuento, J. P. McCoy, C. E. Cameron, S. J. Levine and T. J. Huang, *Analytical Chemistry*, 2016, **88**, 5655-5661.
58. S. Li, X. Ding, Z. Mao, Y. Chen, N. Nama, F. Guo, P. Li, L. Wang, C. E. Cameron and T. J. Huang, *Lab Chip*, 2015, **15**, 331-338.
59. S. Deshmukh, Z. Brzozka, T. Laurell and P. Augustsson, *Lab Chip*, 2014, **14**, 3394-3400.
60. P. Augustsson, L. B. Åberg, A.-M. K. Swärd-Nilsson and T. Laurell, *Microchimica Acta*, 2009, **164**, 269-277.
61. J. Park, G. Destgeer, H. Kim, Y. Cho and H. J. Sung, *Lab on a Chip*, 2018, **18**, 2936-2945.
62. Z. Liu, A. Fornell, L. Barbe, K. Hjort and M. Tenje, *Biomicrofluidics*, 2019, **13**, 064123.
63. C. Wyatt Shields Iv, C. D. Reyes and G. P. López, *Lab on a Chip*, 2015, **15**, 1230-1249.
64. W. M. Weaver, P. Tseng, A. Kunze, M. Masaeli, A. J. Chung, J. S. Dudani, H. Kittur, R. P. Kulkarni and D. Di Carlo, *Current Opinion in Biotechnology*, 2014, **25**, 114-123.
65. D. Ren, Y. Xia and Z. You, *Journal of biomedical optics*, 2013, **18**, 096005-096005.
66. Y. S. Zhang, K. Yue, J. Aleman, K. Mollazadeh-Moghaddam, S. M. Bakht, J. Yang, W. Jia, V. Dell'Erba, P. Assawes, S. R. Shin, M. R. Dokmeci, R. Oklu and A. Khademhosseini, *Annals of Biomedical Engineering*, 2017, **45**, 148-163.
67. A. Nilghaz, D. R. Ballerini and W. Shen, *Biomicrofluidics*, 2013, **7**, 051501.
68. X. Wei, X. Yang, Z.-p. Han, F.-f. Qu, L. Shao and Y.-f. Shi, *Acta Pharmacologica Sinica*, 2013, **34**, 747-754.
69. N. Norouzi, H. C. Bhakta and W. H. Grover, *PLOS ONE*, 2017, **12**, e0180520.
70. L. Schmid, D. A. Weitz and T. Franke, *Lab Chip*, 2014, **14**, 3710-3718.
71. X. Ding, S.-C. S. Lin, M. I. Lapsley, S. Li, X. Guo, C. Y. Chan, I. K. Chiang, L. Wang, J. P. McCoy and T. J. Huang, *Lab Chip*, 2012, **12**, 4228-4231.
72. L. Ren, Y. Chen, P. Li, Z. Mao, P.-H. Huang, J. Rufo, F. Guo, L. Wang, J. P. McCoy, S. J. Levine and T. J. Huang, *Lab Chip*, 2015, **15**, 3870-3879.
73. D. J. Collins, A. Neild and Y. Ai, *Lab Chip*, 2016, **16**, 471-479.
74. M. E. Piyasena, P. P. Austin Suthanthiraraj, R. W. Applegate, A. M. Goumas, T. A. Woods, G. P. López and S. W. Graves, *Analytical Chemistry*, 2012, **84**, 1831-1839.
75. L. Ren, S. Yang, P. Zhang, Z. Qu, Z. Mao, P.-H. Huang, Y. Chen, M. Wu, L. Wang, P. Li and T. J. Huang, *Small*, 2018, **14**, 1801996.

76. J. Oakey, R. W. Applegate, E. Arellano, D. D. Carlo, S. W. Graves and M. Toner, *Analytical Chemistry*, 2010, **82**, 3862-3867.
77. M.-Y. Kim, T. Oskarsson, S. Acharyya, D. X. Nguyen, X. H.-F. Zhang, L. Norton and J. Massagué, *Cell*, 2009, **139**, 1315-1326.
78. P. Augustsson, C. Magnusson, M. Nordin, H. Lilja and T. Laurell, *Analytical Chemistry*, 2012, **84**, 7954-7962.
79. M. Antfolk, C. Antfolk, H. Lilja, T. Laurell and P. Augustsson, *Lab Chip*, 2015, **15**, 2102-2109.
80. M. Antfolk, C. Magnusson, P. Augustsson, H. Lilja and T. Laurell, *Analytical Chemistry*, 2015, **87**, 9322-9328.
81. C. Magnusson, P. Augustsson, A. Lenshof, Y. Ceder, T. Laurell and H. Lilja, *Analytical Chemistry*, 2017, **89**, 11954-11961.
82. M. C. Zalis, J. F. Reyes, P. Augustsson, S. Holmqvist, L. Roybon, T. Laurell and T. Deierborg, *Integrative Biology*, 2016, **8**, 332-340.
83. M. Wu, P.-H. Huang, R. Zhang, Z. Mao, C. Chen, G. Kemeny, P. Li, A. V. Lee, R. Gyanchandani, A. J. Armstrong, M. Dao, S. Suresh and T. J. Huang, *Small*, 2018, **14**, 1801131.
84. T. M. Maul, D. W. Chew, A. Nieponice and D. A. Vorp, *Biomechanics and modeling in mechanobiology*, 2011, **10**, 939-953.
85. X. Li, M. Dao, G. Lykotrafitis and G. E. Karniadakis, *Journal of biomechanics*, 2017, **50**, 34-41.
86. A. Adamo, A. Sharei, L. Adamo, B. Lee, S. Mao and K. F. Jensen, *Analytical Chemistry*, 2012, **84**, 6438-6443.
87. W. H. Grover, A. K. Bryan, M. Diez-Silva, S. Suresh, J. M. Higgins and S. R. Manalis, *Proc Natl Acad Sci U S A*, 2011, **108**, 10992.
88. S. E. Cross, Y.-S. Jin, J. Rao and J. K. Gimzewski, *Nature Nanotechnology*, 2007, **2**, 780-783.
89. S. Suresh, *Acta Biomater*, 2007, **3**, 413-438.
90. D. Di Carlo, *Journal of laboratory automation*, 2012, **17**, 32-42.
91. J. H. Kang, T. P. Miettinen, L. Chen, S. Olcum, G. Katsikis, P. S. Doyle and S. R. Manalis, *Nat Methods*, 2019, **16**, 263-269.
92. D. Hartono, Y. Liu, P. L. Tan, X. Y. S. Then, L.-Y. L. Yung and K.-M. Lim, *Lab Chip*, 2011, **11**, 4072-4080.
93. H. Wang, Z. Liu, D. M. Shin, Z. Chen, Y. Cho, D.-Y. Jang, Y.-J. Kim and A. Han, 2013.
94. H. Wang, Z. Liu, D. M. Shin, Z. G. Chen, Y. Cho, Y.-J. Kim and A. Han, *Lab on a Chip*, 2019, **19**, 387-393.
95. P. Augustsson, J. T. Karlsen, H.-W. Su, H. Bruus and J. Voldman, *Nat Commun*, 2016, **7**, 11556.
96. L. Ren, S. Yang, P. Zhang, Z. Qu, Z. Mao, P. H. Huang, Y. Chen, M. Wu, L. Wang and P. Li, *Small*, 2018, **14**, 1801996.
97. L. Zhao, P. Niu, E. Casals, M. Zeng, C. Wu, Y. Yang, S. Sun, Z. Zheng, Z. Wang, Y. Ning, X. Duan and W. Pang, *Lab on a Chip*, 2021, **21**, 660-667.

98. M. Wu, C. Chen, Z. Wang, H. Bachman, Y. Ouyang, P.-H. Huang, Y. Sadovsky and T. J. Huang, *Lab on a Chip*, 2019, **19**, 1174-1182.
99. Y. Wu, A. G. Stewart and P. V. Lee, *Lab on a Chip*, 2021, **21**, 2812-2824.
100. Y. Wu, A. G. Stewart and P. V. S. Lee, *Biomicrofluidics*, 2019, **13**, 024107.
101. S. Hong, Q. Pan and L. P. Lee, *Integrative biology*, 2012, **4**, 374-380.
102. A. G. Fraser, R. S. Kamath, P. Zipperlen, M. Martinez-Campos, M. Sohrmann and J. Ahringer, *Nature*, 2000, **408**, 325-330.
103. I. d. C. Cáceres, N. Valmas, M. A. Hilliard and H. Lu, *PloS one*, 2012, **7**, e35037.
104. S. K. Mohanty, A. Uppal and P. K. Gupta, *Biotechnology letters*, 2004, **26**, 971-974.
105. K. Chung, M. M. Crane and H. Lu, *Nature methods*, 2008, **5**, 637-643.
106. C. Pardo-Martin, T.-Y. Chang, B. K. Koo, C. L. Gilleland, S. C. Wasserman and M. F. Yanik, *Nature methods*, 2010, **7**, 634-636.
107. S. X. Guo, F. Bourgeois, T. Chokshi, N. J. Durr, M. A. Hilliard, N. Chronis and A. Ben-Yakar, *Nature methods*, 2008, **5**, 531-533.
108. M. Rasmussen, L. Oddershede and H. Siegumfeldt, *Applied and environmental microbiology*, 2008, **74**, 2441-2446.
109. D. Ahmed, A. Ozcelik, N. Bojanala, N. Nama, A. Upadhyay, Y. Chen, W. Hanna-Rose and T. J. Huang, *Nat Commun*, 2016, **7**, 11085.
110. Q. Tang, F. Liang, L. Huang, P. Zhao and W. Wang, *Biomedical Microdevices*, 2020, **22**, 1-11.
111. L. Feng, B. Song, D. Zhang, Y. Jiang and F. Arai, *Micromachines*, 2018, **9**, 596.
112. J. Zhang, S. Yang, C. Chen, J. H. Hartman, P.-H. Huang, L. Wang, Z. Tian, P. Zhang, D. Faulkenberry, J. N. Meyer and T. J. Huang, *Lab Chip*, 2019, **19**, 984-992.
113. T. Schwarz, G. Petit-Pierre and J. Dual, *The Journal of the Acoustical Society of America*, 2013, **133**, 1260-1268.
114. H. Bruus, *Lab Chip*, 2011, **11**, 3742-3751.
115. J. T. Karlsen and H. Bruus, *Physical Review E*, 2015, **92**, 043010.
116. H. Bruus, *Lab Chip*, 2012, **12**, 20-28.
117. H. Bruus, *Lab Chip*, 2012, **12**, 1014-1021.
118. S. Liu, G. Xu, Z. Ni, X. Guo, L. Luo, J. Tu and D. Zhang, *Applied Physics Letters*, 2017, **111**, 043508.
119. L. Rayleigh, *Proceedings of the London mathematical Society*, 1885, **1**, 4-11.
120. Z. Mao, Y. Xie, F. Guo, L. Ren, P.-H. Huang, Y. Chen, J. Rufo, F. Costanzo and T. J. Huang, *Lab Chip*, 2016, **16**, 515-524.
121. C. Acikgoz, M. A. Hempenius, J. Huskens and G. J. Vancso, *European Polymer Journal*, 2011, **47**, 2033-2052.
122. C. Sun, F. Wu, Y. Fu, D. J. Wallis, R. Mikhaylov, F. Yuan, D. Liang, Z. Xie, H. Wang, R. Tao, M. H. Shen, J. Yang, W. Xun, Z. Wu, Z. Yang, H. Cang and X. Yang, *Ultrasonics*, 2020, **108**, 106202.
123. S. Yao, J. Wang, H. Liu, X. Hu, H. Zhang, X. Cheng and Z. Ling, *Journal of Alloys and Compounds*, 2008, **455**, 501-505.
124. T. Zheng, C. Wang, Q. Hu and S. Wei, *Applied Physics Letters*, 2018, **112**, 233702.
125. X. Du, Y. Q. Fu, J. Luo, A. Flewitt and W. Milne, *Journal of Applied Physics*, 2009, **105**, 024508.

126. Popa, Laura C., and Dana Weinstein. "2DEG electrodes for piezoelectric transduction of AlGaN/GaN MEMS resonators." In 2013 Joint European Frequency and Time Forum & International Frequency Control Symposium (EFTF/IFC), pp. 922-925. IEEE, 2013.
127. Kirschner, Jared. "Surface acoustic wave sensors (SAWS)." Micromechanical systems (2010).
128. Hashimoto, Ken-ya, and Ken-Ya Hashimoto. Surface acoustic wave devices in telecommunications. Vol. 116. Berlin: Springer-Verlag, 2000.
129. J. Liow, *Journal of Cleaner Production*, 2009, **17**, 662-667.
130. L. Wang, R. Kodzius, X. Yi, S. Li, Y. S. Hui and W. Wen, *Sensors and Actuators B: Chemical*, 2012, **168**, 214-222.
131. K. Ren, J. Zhou and H. Wu, *Accounts of chemical research*, 2013, **46**, 2396-2406.
132. J. C. McDonald, D. C. Duffy, J. R. Anderson, D. T. Chiu, H. Wu, O. J. Schueller and G. M. Whitesides, *ELECTROPHORESIS: An International Journal*, 2000, **21**, 27-40.
133. A. Lenshof, M. Evander, T. Laurell and J. Nilsson, *Lab Chip*, 2012, **12**, 684-695.
134. N. Nama, R. Barnkob, Z. Mao, C. J. Kähler, F. Costanzo and T. J. Huang, *Lab Chip*, 2015, **15**, 2700-2709.
135. X. Ding, Z. Peng, S.-C. S. Lin, M. Geri, S. Li, P. Li, Y. Chen, M. Dao, S. Suresh and T. J. Huang, *Proc Natl Acad Sci U S A*, 2014, **111**, 12992-12997.
136. J. Kim and R. J. DeBerardinis, *Cell metabolism*, 2019, **30**, 434-446.
137. X. Ding, Z. Peng, S. C. Lin, M. Geri, S. Li, P. Li, Y. Chen, M. Dao, S. Suresh and T. J. Huang, *Proc Natl Acad Sci U S A*, 2014, **111**, 12992-12997.
138. E. Anderson, D. Petersen and R. Tobey, *Biophysical Journal*, 1970, **10**, 630-645.
139. J. Guck, S. Schinkinger, B. Lincoln, F. Wottawah, S. Ebert, M. Romeyke, D. Lenz, H. M. Erickson, R. Ananthakrishnan, D. Mitchell, J. Käs, S. Ulvick and C. Bilby, *Biophys J*, 2005, **88**, 3689-3698.
140. J. R. Staunton, B. L. Doss, S. Lindsay and R. Ros, *Sci Rep*, 2016, **6**, 19686.
141. T. Yang, F. Bragheri, G. Nava, I. Chiodi, C. Mondello, R. Osellame, K. Berg-Sørensen, I. Cristiani and P. Minzioni, *Sci Rep*, 2016, **6**, 23946.
142. Q. Fu, Y. Zhang, T. Huang, Y. Liang and Y. Liu, *Biomicrofluidics*, 2021, **15**, 064101.
143. F. Garofalo, A. Lenshof, A. Urbansky, F. Olm, A. C. Bonestroo, L. Ekblad, S. Scheding and T. Laurell, *Microfluidics and Nanofluidics*, 2020, **24**, 64.
144. F. Wu, M. H. Shen, J. Yang, H. Wang, R. Mikhaylov, A. Clayton, X. Qin, C. Sun, Z. Xie and M. Cai, *IEEE Electron Device Letters*, 2021, **42**, 577-580.
145. R. Barnkob, P. Augustsson, T. Laurell and H. Bruus, *Physical Review E*, 2012, **86**, 056307.
146. M. Kinnunen, A. Kauppila, A. Karmenyan and R. Myllylä, *Biomed Opt Express*, 2011, **2**, 1803-1814.
147. J. Paulus, *Blood*, 1975, **46**, 321-336.
148. M. Tayebi, D. Yang, D. J. Collins and Y. Ai, *Nano Letters*, 2021, **21**, 6835-6842.
149. X. M. Tang, M. N. Toksöz, P. Tarif and R. H. Wilkens, *The Journal of the Acoustical Society of America*, 1988, **83**, 453-462.
150. K. D. Frampton, S. E. Martin and K. Minor, *Applied Acoustics*, 2003, **64**, 681-692.
151. J. Dong, D. Liang, X. Yang and C. Sun, *Ultrasonics*, 2021, **117**, 106547.